UNIVERSITAT POLITÈCNICA DE CATALUNYA BARCELONATECH

Development of a Large-Eddy simulation framework for engineering applications using the finite element method

Georgios Chrysokentis

UNIVERSITAT POLITÈCNICA
DE CATALUNYA
BARCELONATECH

Universitat Politècnica de Catalunya
Facultat de Matemàtiques i Estadística

Development of a Large-Eddy Simulation framework for engineering applications using the Finite Element method

Ph.D. Thesis

Georgios Chrysokentis
Computer Applications in Science and Engineering
Barcelona Supercomputing Center (BSC)

Supervisor: Dr. Herbert Owen

February, 2019

Acknowledgements

During my doctoral studies, I went through a lot of ups and a lot of downs. What I found very important is to have people to share the positives with, and the same people will help you get through the difficulties. I would like to thank all those people that made this thesis possible.

First and foremost I would like to express my gratitude to my supervisor, Dr. Herbert Owen. I have been extremely lucky to have a supervisor that cared so much about my work and invested a lot of time to help me finish it. Herbert was always there to guide and mentor me. Even at times when I was difficult to work with, he was patient and understanding. He always found time to help me with everything I needed. He also instilled to me a pragmatic approach to research, which I believe is a valuable quality to have.

I would also like to deeply thank Dr. Oriol Lehmkuhl. Ever since he joined our department, he has been a driving force. His passion for research and for pushing the boundaries is something I greatly admire and can only aspire to replicate in my career. In the same vein, I want to thank Dr. Matias Avila. He always made sure that I fully understood why to use a method or pursue a specific approach and that is a lesson that will stay with me in future endeavors. I would also like to thank Dr. Daniel Mira and Dr. Juan Carlos Cajas for their assistance and their cooperation throughout various stages of my thesis. Furthermore, I want to thank Samuel for helping me with the creation of computational grids for the more complex cases.

My PhD experience was made easier by my "partners in crime", my fellow doctoral students in the CASE department. I would like to thank Alfonso and Simon, who always managed to brighten my day with a bit of banter, Matias and Maria for those long, more philosophical discussions, Edgar, Mariña, Paula, Dani, Jordi and Alex for all the fun times we have had in and out of BSC.

I would like to acknowledge the Spanish Ministry of Economy and Competitiveness for making this work possible through a FPI scholarship, as well as the Barcelona Supercomputing Center for giving me access to significant computational resources, without which this work would not have been possible.

Last but not least, I would like to thank my family, for their unwavering

and unconditional support at every step of the way. My mom and my dad, who have always been by my side and it is only through they support that I am where I am today. My brother and his wife, who have shown great interest in my work and my little nephew whose distractions provided me with valuable breaks during the writing of this thesis.

Abstract

This thesis develops a large eddy simulation framework for engineering applications using the finite element method. It focuses on the numerical formulation, the wall modelling approach as well as the generation of turbulent inflow conditions, with emphasis on incompressible flows.

A low-dissipation formulation is introduced that uses a non-incremental fractional step method to stabilize the pressure and allow the use of finite element pairs that do not satisfy the inf-sup condition, such as equal order interpolation for velocity and pressure. This stabilization introduces an error of $\mathcal{O}(\delta t, h^2)$ (for linear elements) in the conservation of kinetic energy, while the final scheme preserves momentum and angular momentum. Explicit subgrid scale models are used for turbulent closure. Temporal discretization is performed through an explicit, energy-conserving Runge Kutta scheme, coupled with an eigenvalue-based time step estimator. The formulation is compared with the Variational Multiscale method in three common benchmark cases: the decaying isotropic turbulence, the Taylor-Green vortex and the turbulent channel flow at $Re_\tau = 395,\ 950$ and 2003, with favorable results without any need for ad hoc tuning. The formulation is further evaluated in the flow over a sphere and the flow around an Ahmed body.

A new approach is introduced for wall modelling in a finite element context. Instead of the classical finite element method, where part of the domain is omitted and the wall model accounts for it, the mesh extends all the way to the wall, as is commonly done in finite differences and finite volumes. The new approach is tested in a turbulent channel flow at $Re_\tau = 2003$, a neutrally stratified atmospheric boundary layer and the flow over a wall-mounted hump, where it is shown to offer a great improvement over the classical finite element method. In addition, preliminary work is presented on a two-layer non-equilibrium wall model that uses time-averaging to filter the excess Reynolds stresses. It is tested in a turbulent channel flow at $Re_\tau = 2003$ with accurate results. Furthermore a method of synthesizing turbulent inflow conditions through the diffusion process is compared with a precursor method on the flow over a three-dimensional hill, providing results of similar quality at significantly less computational cost.

Finally, the complete framework is evaluated on the flow around the DrivAer model, a realistic car model developed to facilitate aerodynamic

investigations of passenger vehicles, as well as the flow over the Bolund hill, a hill whose geometry represents a scaled-down model of the typical wind farm site. Good agreement with the reference data is achieved.

Contents

List of Figures

List of Tables

Chapter 1

Introduction

1.1 Background

Turbulent phenomena can be observed all around us. The vast majority of fluid flows that exist in nature are under the heavy influence of turbulence. This is especially evident in engineering applications where quantities of interest are directly related to the turbulent behavior of the flow. Looking for example at offshore wind farms, the losses in generated power due to the turbulent wakes of the turbines can reach up to 20%. It is, therefore, of utmost importance to accurately predict the turbulent flows in order to optimize the design of wind turbines and farms, resulting in bigger gains in the harvested power.

For centuries the main means of investigating turbulent flows was through experimental techniques. From the whirling arm of Benjamin Robins in the early 18th century to the first wind tunnel devised by Frank Wenham in 1871, scientists and engineers have always sought to create elaborate experimental devices in order to thoroughly study fluid mechanics. More recently, however, and with the ever-increasing computational power available, the numerical simulation of fluid flows has become more prevalent. Computational Fluid Dynamics (CFD) can provide a cheaper and often faster alternative to experiments for the study of turbulence and the optimization of design processes.

The motion of viscous fluids is described by the Navier-Stokes equations. For incompressible fluids of constant density they can be defined as:

$$\partial_t \mathbf{u} + \mathbf{u} \cdot \nabla \mathbf{u} - \nabla \cdot (2\nu \boldsymbol{\varepsilon}(\mathbf{u})) + \nabla p = \mathbf{f} \tag{1.1}$$

$$\nabla \cdot \mathbf{u} = 0 \tag{1.2}$$

where ν is the kinematic viscosity, $\boldsymbol{\varepsilon}(\mathbf{u})$ is the velocity strain rate tensor defined as $\boldsymbol{\varepsilon}(\mathbf{u}) := \frac{1}{2}\left(\nabla \mathbf{u} + \nabla^T \mathbf{u}\right)$, and $\mathbf{f}$ is the vector of external body forces.

Since the Navier-Stokes equations can only be analytically solved for very simple cases, they instead need to be solved numerically. In order to achieve maximum accuracy in the solution of the Navier-Stokes equations, a discretization fine enough to capture all the scales of the flow is needed. Such a discretization can be very computationally demanding in highly turbulent flows, considering that there is a wide spectrum of dynamically active scales, which increases with the Reynolds number.

For a homogeneous and isotropic turbulent flow, the ratio between the integral length scale and the Kolmogorov scale is:

$$\frac{L}{\eta} = O\left(Re^{3/4}\right) \tag{1.3}$$

where the integral length scale L denotes the size of the most energetic eddies of the flow and the Kolmogorov scale η signifies the size of the smallest turbulent structures. For a cubic volume of edge L, this means that one would need $O\left(Re^3\right)$ degrees of freedom for an accurate prediction of the flow. Both spatial and temporal resolution requirements are included in this estimate. It becomes immediately obvious that a computation that seeks to resolve all the scales of motion in a fluid (Direct Numerical Simulation - DNS) would be practically infeasible for flows of engineering interest (with Reynolds numbers typically ranging between 10^6 and 10^9). Therefore, DNS is limited to fairly simple flows at low Reynolds numbers for the foreseeable future.

Considering all of the above, there arises a need to coarsen the parameters and only directly solve fewer scales, for the computation to become feasible. However, just resolving the scales above a certain size threshold and neglecting the smaller ones will not yield accurate results, since there exists a dynamic relationship between all the scales, i.e. the behavior of the smaller scales has a direct effect on that of the larger ones. To combat this problem, approaches that seek to reduce the computational requirements through the use of empirical modelling to approximate turbulent effects have been devised. The most common are Reynolds-Averaged Navier-Stokes (RANS) methods and Large Eddy Simulations (LES).

In RANS methods the flow equations are time-averaged and, thus, only the mean flow is resolved. Empirical models are used to account for the effects of turbulence. These methods have found extensive use in industry, since they are simple to use and result in significant savings in computational cost. A major downside of this approach is that most RANS models are typically tuned with specific flows in mind and there is not a universal model that will be able to handle all turbulent flows. Furthermore, it struggles to accurately predict highly unsteady flow phenomena, such as those encountered for example in aeroacoustics, as well as the intermittent nature of turbulence. In order to partially alleviate that problem, unsteady RANS

methods have been constructed that can also predict some low-frequency modes apart from the mean flow.

Large Eddy Simulations on the other hand perform a scale separation between the large, energy-containing scales and the small, more universal ones, by means of a low-pass filtering operation. The scales that are above the filtering threshold can be adequately resolved on a relatively coarse grid, while their interaction with the smaller scales is modelled. Since the small scales are the most computationally expensive to resolve, this procedure results in a significant reduction in the computational cost compared to DNS, while still retaining great accuracy in the predictions.

1.2 Large Eddy Simulation

Scale separation is achieved by applying a low-pass filter to the velocity field, such that the instantaneous velocity is decomposed to a filtered and a residual component:

$$\mathbf{u}(x) \equiv \overline{\mathbf{u}}(x) + \mathbf{u}'(x) \tag{1.4}$$

The filtering essentially applies a local spatial averaging over the filter width Δ. Following Leonard [1], we can define $\overline{\mathbf{u}}$ through the convolution:

$$\overline{\mathbf{u}}(x) = \int_{-\infty}^{\infty} G(x - x')u(x')dx' \tag{1.5}$$

where G is a convolution kernel that depends on the type of the filter. Such an explicit filter means that the filter width Δ is not necessarily proportional to the grid size h, allowing for a filter that is coarser than the grid. This type of explicit filtering has the advantage of reducing numerical discretization errors. It does, however, mean that more scales need to be modelled for the same grid, thus increasing the modelling demands. Therefore, in practice, the grid size is often used as the filter, resulting in what is commonly known as implicit filtering. The latter approach is used in this work.

A schematic representation of the implicit filtering can be seen in Fig. 1.1, where the scales below the cutoff wave number $k_\Delta = \pi/\Delta$ are resolved, while the rest of the scales are modelled. Here Δ is directly related to the grid size.

Applying the filtering procedure to equations 1.1 and 1.2 we obtain:

$$\partial_t \overline{\mathbf{u}} + \overline{\mathbf{u}} \cdot \nabla \overline{\mathbf{u}} - \nabla \cdot (2\nu\boldsymbol{\varepsilon}(\overline{\mathbf{u}})) + \nabla \overline{p} = \overline{\mathbf{f}} - \nabla \cdot \tau \tag{1.6}$$

$$\nabla \cdot \overline{\mathbf{u}} = 0 \tag{1.7}$$

where the tensor

$$\tau = \overline{u_i u_j} - \overline{u}_i \overline{u}_j \tag{1.8}$$

comes from the nonlinearity of the convection term. It expresses the effect of the unresolved scales on the resolved ones. Since the original velocity

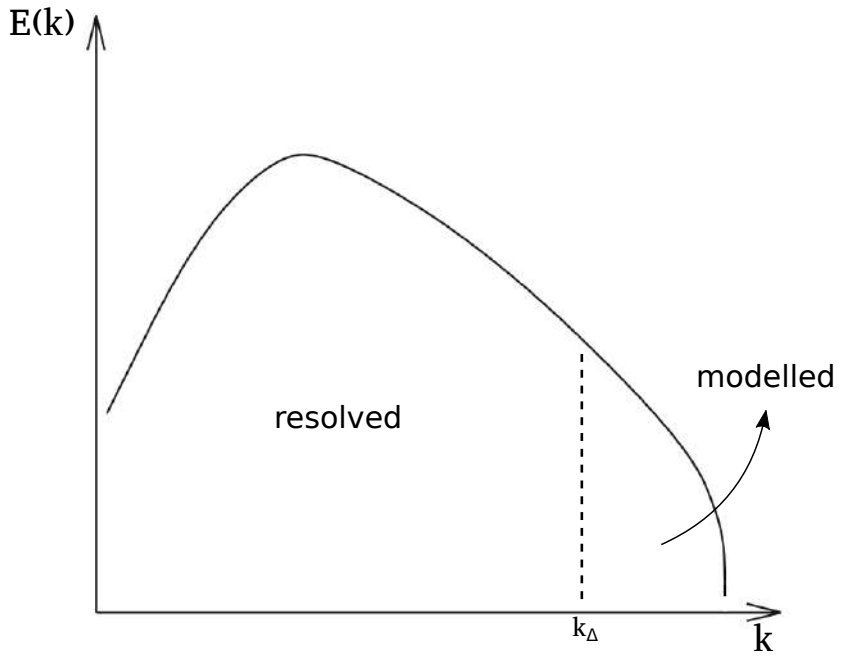

Figure 1.1: Schematic representation of the implicit filtering operation. k_Δ denotes the cutoff wave number, directly associated with the filter width Δ.

field **u** appears in Eq. 1.8, the tensor cannot be directly computed at the discrete level and therefore needs to be modelled.

The classical way to address the modelling of tensor τ (which we will refer to as the subgrid scale tensor) is through an explicit subgrid scale model. Most of the current subgrid scale models rely on the concept of an eddy viscosity ν_t, that relates the traceless part of the subgrid scale tensor T to the strain tensor of the resolved velocity through the following expression:

$$\tau_{ij}^{\alpha} = \tau_{ij} - \frac{1}{3}\delta_{ij}\tau_{kk} = -2\nu_t\overline{\varepsilon}_{ij} \tag{1.9}$$

The first such model to have been developed and still widely used is the Smagorinsky model [2]. It calculates the eddy viscosity as:

$$\nu_t = (C_s\Delta)^2|\overline{\varepsilon}| \tag{1.10}$$

where Δ denotes the filter width, $|\overline{\varepsilon}| = \sqrt{2\overline{\varepsilon}_{ij}\overline{\varepsilon}_{ij}}$ and C_s is the model constant. A dynamic procedure was proposed by Germano et al. [3] and further

enhanced by Lilly [4] and Meneveau et al. [5], where the model coefficient is evaluated locally using an additional test filter (typically taken to be twice Δ), in order to better represent the local state of the flow. For more information on the various subgrid scale models, the reader is referred to [6, 7]. In this work the Vreman model [8], explained in detail in Section 2.3, is used for turbulence closure. The low-dissipation formulation, presented in the same section, makes use of explicit subgrid scale models and can therefore be categorized as an explicit LES method.

An alternative approach to modelling the subgrid scales is to rely on numerical dissipation to account for their effect on the resolved scales. This type of approach was originally proposed by Boris et al. in [9]. They advocated that there should be no explicit filtering or subgrid scale model. Instead both the filtering and the subgrid scale modelling are performed implicitly by the numerics. This is achieved by using an appropriate numerical method to solve the Navier-Stokes equations. The coarseness of the grid leads to significant numerical stresses, that model the contribution of the subgrid scales. Several methods have been developed following that concept, with most of them falling under the non-oscillatory finite volume (NFV) class of methods. A more detailed description of such methods can be found in [10]. Here, we consider a residual-based Variational Multiscale method that relies on a similar concept [11, 12, 13, 14, 15]. In this method, the contribution of the subgrid scales is modelled through the numerical stabilization used to stabilize the Galerkin finite element approximation. This method is presented in Section 2.2. It is important to note that the scope of this work (and Chapter 2 in particular) is not to provide a general comparison of the classical and implicit Large Eddy Simulations, but rather the Variational Multiscale method, commonly used in the finite element community, with a new low-dissipation formulation.

Although LES is less computationally demanding than DNS, it is still prohibitively expensive for wall-bounded flows at high Reynolds numbers. The length scale of the energy-containing eddies is greatly reduced in the near-wall region, which significantly increases the grid requirements in order to resolve them. This leads to an exorbitant computational cost, comparable to that of DNS. In an effort to alleviate this problem, wall modelling techniques are instead used, where the near-wall turbulence is not resolved, but is instead modelled. Additionally, since LES computes part of the turbulent spectrum, inflow boundary conditions that possess characteristics of the incoming turbulence need to be prescribed. Imposing just the mean flow or adding random perturbations is not successful, since a large upstream distance is required for the correct turbulent structures to develop, significantly increasing the computational cost. Therefore, techniques for the generation of turbulent inflow conditions are utilized. Both of these issues are addressed in this work, with literature reviews presented in the respective chapters.

1.3 State of the art review

The VMS framework was originally proposed by Hughes in [11], as a means of designing finite element methods, that ensure stability in scenarios where the standard Galerkin approximation is shown to falter. In a fluid dynamics context, such scenarios occur in convection-dominated flows as well as when finite element pairs that do not satisfy the inf-sup condition are used. It was further established as a general framework for computational mechanics in [12]. The framework relies on the concept of decomposing the unknown into a finite element scale that is resolved, and a fine scale that cannot be captured by the computational mesh and is instead approximated. The latter is commonly referred to as subscale.

The method was first considered as a means of performing LES in [13], and has since become highly popular within the finite element community. An a priori scale separation through variational projection was utilized in place of the traditional filtering procedure used in classical LES formulations. In the proposed formulation the traditional Smagorinsky model acts only on the small scales, allowing for consistency to be preserved in the variational equation governing the large scales, since it does not contain any modelling. The method was successfully applied to benchmark cases such as the decaying isotropic turbulence and the turbulent channel flow [14, 15, 16]. Two different possibilities are explored for the eddy viscosity used in these works: one that depends on the strain rate tensor of the large-scale velocity, named "large-small", and one that depends on that of the small-scale velocity, named "small-small". Both approaches offered improved results compared with the dynamic Smagorinsky model in a classical LES setting. The effect of employing the dynamic Smagorinsky model on the small scales was explored in [17, 18], where higher accuracy was achieved compared to the static model. A different approach where the scale separation is extended to obtain three scale groups was considered in [19, 20], where the unknown is decomposed into the following: large resolved scales, small resolved scales and unresolved scales. The turbulence model is then applied to the small resolved scales. The three-scale VMS approach was extended to a mixed finite element-finite volume framework in [21, 22] and tested in flows over bluff bodies with good results. This type of approach will not be explored in the context of this thesis. The reader is referred to the aforementioned articles as well as [23] for a more detailed explanation.

A first mention of VMS as a fully implicit LES approach is encountered in [24]. The author poses the question "how does the numerical method behave as a physical model" as a point of further research, laying the ground for the explicit subgrid scale model to be completely omitted in the formulation. This idea was explored in detail by Calo in [25], albeit in a finite volume context, as well as Hughes et al. [26] and Bazilevs et al. [27]. An alternative approach to turbulence modelling, where the use of an eddy viscosity is

avoided, was suggested. An analytical solution to the fine scale problem is sought so that their effect on the coarse scales can be accounted for. A residual-based approximation is used for the solution of the fine scales. Different residual-based VMS methods can be derived, depending on the exact treatment of the subscales. Instead of considering the subscales quasi-static, the temporal derivative of the velocity subscales can be included in the method, which leads to the so-called dynamic subscales [28]. Nonlinear subscales are obtained by keeping the scale decomposition in the nonlinear terms of the equations. Nonlinear scale splitting has shown to conserve momentum globally [28]. Considering the subscale space to be L^2-orthogonal to the finite element space, proposed in [24, 29] has shown to allow for the possibility of backscatter when combined with dynamic subscales [30, 31], as well as produce numerical dissipation that is proportional to the molecular one [32].

Extensive reviews on variational multiscale methods can be found in [23, 33, 34, 35].

1.4 Scope of the thesis

The goal of this thesis is to develop a complete framework for performing large eddy simulations of engineering applications, using the finite element method, with emphasis on incompressible flows. This is achieved by focusing on three different aspects:

Numerical formulation

The quality of computational simulations of fluid flows is highly dependent on the numerical formulation of choice, especially in the case of LES, where a significant portion of the turbulence is directly resolved, with only a weak dependence on empirical modelling. Ideally, the numerical formulation needs to: a) be able to offer accurate results without the need for ad hoc tuning and b) be applicable (in terms of accuracy) for a wide variety of flows and Reynolds numbers. A residual-based Variational Multiscale (VMS) method, commonly used for large eddy simulations in the finite element community, is assessed and a new formulation, that fulfills the above requirements, is developed.

Wall modelling

As mentioned previously, performing wall-resolved LES in flows of industrial interest can often incur a prohibitive computational cost. Therefore, building a framework that aims to be used in industrial applications must contain wall-modelling techniques. An approach commonly used in finite elements is evaluated and is shown to falter, which leads to the proposal of a new

approach that significantly reduces the error in the predictions for velocity and skin friction. Additionally, a non-equilibrium wall model is examined.

Inflow boundary conditions

Considering that the large scales of turbulence are directly resolved in LES, the boundary conditions imposed at the inflow of the computational domain cannot be laminar, but must instead contain information of the incoming turbulence. Therefore, the generation of appropriate inflow conditions is necessary. Several such techniques are examined and the best performing one is selected with high focus on low computational cost and the simplicity of implementation.

1.5 Computational framework

All the simulations presented in this thesis were performed using the computational code Alya, developed in the Computer Applications in Science and Engineering (CASE) department of the Barcelona Supercomputing Center (BSC). Alya is a highly parallel finite element multiphysics code, written in Fortran 90/95, optimized for large-scale computers, with a reported scalability of up to 100.000 cores [36, 37]. The code is part of the Unified European Application Benchmark Suite, provided in the Partnership for Advanced Computing in Europe (PRACE) framework.

The code is structured into a kernel, which is responsible for the general subroutines, solvers and parallelization, and different modules, where each module represents different physics. In this work the Nastin module, which solves the incompressible Navier-Stokes equations, has been predominantly used. The code already contained important tools used in this thesis, such as coupling structures. However, Alya is an ever-changing code, being simultaneously developed by a large number of people, which means that a lot of effort is needed on a regular basis to adapt to the new status.

In-house scripts have been used for the generation of the computational grids in simple geometries. For the more complex geometries, however, commercial software has been used, namely ANSYS ICEM CFD and ANSA, developed by BETA CAE Systems.

The simulations were carried out on MareNostrum, one of the most powerful supercomputers worldwide, hosted in BSC. It consists of 48 racks with 3,456 compute nodes, where each node contains 48 processors, resulting in a total of over 165.000 processors. Its peak performance is reported at 11.1 petaflops.

1.6 Outline of the thesis

The structure of the thesis is as follows:

Following this introduction, the incompressible Navier-Stokes problem is presented in Chapter 2. The two different formulations considered here for the solution of the problem, namely the Variational Multiscale method and a new low-dissipation formulation, are introduced. The formulations are compared in a set of benchmark cases, namely the decaying isotropic turbulence, the Taylor-Green vortex and the turbulent channel flow. A reasoning for selecting the low-dissipation formulation is provided, and the formulation is further evaluated in more complex cases, such as the flow over a sphere and the Ahmed body. This chapter elaborates on the material in:

Lehmkuhl O., Houzeaux G., Owen H., Chrysokentis G., Rodriguez I. A low-dissipation finite element scheme for scale resolving simulations of turbulent flows. Under revision. *Journal of Computational Physics.*

Chapter 3 examines methods for the generation of turbulent inflow conditions. The precursor method is presented, before an extensive review on techniques for synthesizing turbulence is performed. The method of creating a synthetic inflow through the diffusion process is explained. The two methods are compared in the prediction of the flow over a three-dimensional hill.

Wall modelling techniques are explored in Chapter 4. An estimate for the computational requirements of resolving the inner layer is provided, justifying the need for modelling the near-wall region. In Section 4.2, the approach commonly used for wall-modelled LES in finite elements is examined and is shown to falter both theoretically and in practice. Instead the approach typically used in finite differences is adapted and is shown to provide significant improvements. Additionally, techniques such as moving the LES/wall model interface further away from the wall and time-averaging the wall model input are examined. All the aforementioned methods are evaluated in a wide range of flows, such as the turbulent channel flow, the neutrally stratified atmospheric boundary layer and the flow over a wall-mounted hump. Finally, in Section 4.3, preliminary work on a two-layer non-equilibrium wall model is presented. The model uses time-averaging in order to filter the excess of Reynolds stresses, a common problem in this family of models. Results from a turbulent channel flow are presented. This chapter elaborates on the material in:

Owen H., Chrysokentis G., Avila M., Mira D., Houzeaux G., Cajas J. C., Lehmkuhl O. Wall-modeled large-eddy simulation in a finite element framework. In review. *Computers and Fluids.*

The complete framework developed in the previous chapters is employed

in real world applications in Chapter 5. More specifically two complex geometries are examined: a) the DrivAer model, a realistic car model developed in the Technical University of Munich to facilitate aerodynamic investigations of passenger vehicles and b) the Bolund hill, a hill located on a peninsula close to the city of Roskilde, Denmark, whose shape represents a scaled-down model of the typical wind farm site. This chapter elaborates on the material in:

Lehmkuhl O., Chrysokentis G., Gomez S., Owen H. Large eddy simulation for automotive aerodynamics with Alya. In *Tenth International Conference on Computational Fluid Dynamics (ICCFD10)*, Barcelona (Spain), 9-13 July 2018.

Finally, conclusions are drawn in Chapter 6 and recommendations for future work are presented.

Chapter 2

Numerical formulations

2.1 The incompressible Navier-Stokes equations

The Navier-Stokes equations for a fluid moving in the domain Ω bounded by $\Gamma = \partial\Omega$ during the time interval (t_0, t_f) consist in finding the velocity $\mathbf{u}$ and a kinematic pressure p such that:

$$\partial_t \mathbf{u} + \mathbf{u} \cdot \nabla \mathbf{u} - \nabla \cdot (2\nu\boldsymbol{\varepsilon}(\mathbf{u})) + \nabla p = \mathbf{f} \quad \text{in } \Omega \times (t_0, t_f) \tag{2.1}$$

$$\nabla \cdot \mathbf{u} = 0 \quad \text{in } \Omega \times (t_0, t_f) \tag{2.2}$$

where ν is the kinematic viscosity, $\boldsymbol{\varepsilon}(\mathbf{u})$ is the velocity strain rate tensor defined as $\boldsymbol{\varepsilon}(\mathbf{u}) := \frac{1}{2}\left(\nabla\mathbf{u} + \nabla^T\mathbf{u}\right)$, and $\mathbf{f}$ is the vector of external body forces. The Dirichlet condition consists in prescribing the velocity, while the Neumann condition consists in prescribing the traction $\sigma \cdot \mathbf{n}$, where σ is the stress tensor such that $\sigma = -p\mathbf{I} + 2\nu\boldsymbol{\varepsilon}(\mathbf{u})$. Let Γ_D and Γ_N be the Dirichlet and Neumann parts of the boundary Γ respectively, such that $\Gamma_D \cup \Gamma_N = \Gamma$ and $\Gamma_D \cap \Gamma_N = \emptyset$. The boundary conditions consist in prescribing:

$$\begin{aligned} \mathbf{u} &= \mathbf{u}_D \quad \text{on } \Gamma_D \times (t_0, t_f) \\ \sigma \cdot \mathbf{n} &= 0 \quad \text{on } \Gamma_N \times (t_0, t_f). \end{aligned} \tag{2.3}$$

Additionally, initial conditions:

$$\mathbf{u} = \mathbf{u}_0 \quad \text{in } \Omega \times \{t_0\}, \tag{2.4}$$

have to be appended to the problem.

In order to obtain the weak or variational formulation of the Navier-Stokes equations (2.1) and (2.2), the spaces of vector functions $\mathbf{V}_D = \mathbf{H}^1_D(\Omega)$, $\mathbf{V}_0 = \mathbf{H}^1_0(\Omega)$ and $\mathcal{Q} = L^2(\Omega)/\mathbb{R}$ are introduced. As usual, $L^2(\Omega)$ is the space of square-integrable functions, $H^1(\Omega)$ is a subspace of $L^2(\Omega)$ formed by functions whose derivatives also belong to $L^2(\Omega)$, $H^1_D(\Omega)$ is a subspace of $H^1(\Omega)$ that satisfies the Dirichlet boundary conditions on Γ, $H^1_0(\Omega)$ is a subspace of $H^1(\Omega)$ whose functions are zero on Γ and $\mathbf{H}^1_D$ and

$\mathbf{H}_0^1$ are their vector counterparts in a 2 or 3 dimensional space. $(\cdot,\cdot)$ indicates the standard L^2 inner product.

For the evolutionary case $\mathbf{V}_t \equiv L^2(t_0, t_f; \mathbf{V}_D)$ and $\mathcal{Q}_t \equiv \mathcal{D}'(t_0, t_f; \mathcal{Q})$ are introduced, where $L^p(t_0, t_f; X)$ is the space of time dependent functions in a normed space X such that $\int_0^{t_f} ||f||_X^p dt < \infty$, $1 \leqslant p < \infty$ and $\mathcal{Q}_t$ consists of mappings whose $\mathcal{Q}$-norm is a distribution in time. The weak form of problem (2.1, 2.2) with the boundary conditions we have just defined is then: Find $\mathbf{u} \in \mathbf{V}_t$, $p \in \mathcal{Q}_t$ such that:

$$(\partial_t \mathbf{u}, \mathbf{v}) + (\mathbf{u} \cdot \nabla \mathbf{u}, \mathbf{v}) + 2(\nu \boldsymbol{\varepsilon}(\mathbf{u}), \boldsymbol{\varepsilon}(\mathbf{v})) - (p, \nabla \cdot \mathbf{v}) + (q, \nabla \cdot \mathbf{u}) = (\mathbf{f}, \mathbf{v}), \tag{2.5}$$

for all $(\mathbf{v}, q) \in \mathbf{V}_0 \times \mathcal{Q}$.

The space discretization is built with the finite element method. $\mathbf{V}_{Dh} \subset \mathbf{V}_D$, $\mathbf{V}_{0h} \subset \mathbf{V}_0$ and $\mathcal{Q}_h \subset \mathcal{Q}$ are the discrete linear subspaces that approximate the respective continuous spaces. The same interpolation will be used for both the velocity and the pressure. $\mathbf{V}_{Dh}$ incorporates the Dirichlet conditions for the velocity components and $\mathcal{Q}_h$ has one pressure fixed to zero if the normal component of the velocity is prescribed on the whole boundary. The space discretized problem reads: Find $\mathbf{u}_h^{n+1} \in \mathbf{V}_{Dh}$ and $p^{n+1} \in \mathcal{Q}_h$, such that:

$$\begin{aligned}(\partial_t \mathbf{u}_h, \mathbf{v}_h) + (\mathbf{u}_h \cdot \nabla \mathbf{u}_h, \mathbf{v}_h) + 2(\nu \boldsymbol{\varepsilon}(\mathbf{u}_h), \boldsymbol{\varepsilon}(\mathbf{v}_h)) \\ - (p_h, \nabla \cdot \mathbf{v}_h) + (q_h, \nabla \cdot \mathbf{u}_h) = (\mathbf{f}, \mathbf{v}_h),\end{aligned} \tag{2.6}$$

for all $(\mathbf{v}_h, q_h) \in \mathbf{V}_{0h} \times \mathcal{Q}_h$, which constitutes the Galerkin Finite Element (FE) approximation.

2.2 Variational Multiscale method

The Galerkin Finite Element approximation (Eq. 2.6) is known to face numerical instabilities in convection-dominated flows, which is often the case in high Reynolds numbers problems. Additionally, in order for the problem to be well-posed, the pair $\mathbf{V}_h \times \mathcal{Q}_h$ needs to satisfy the inf-sup condition [38]. In an effort to solve convection-dominated problems and allow for finite element pairs that do not satisfy the inf-sup condition, Hughes proposed the Variational Multiscale method (VMS) in [11, 12], presented in this section. The idea is to use variational projections and restrict modelling to just the fine-scale equations.

Let us consider the direct-sum decomposition of spaces $\mathbf{V}$ and $\mathcal{Q}$ into coarse and fine scales:

$$\begin{aligned}\mathbf{V} &= \mathbf{V}_h + \widetilde{\mathbf{V}}, \\ \mathcal{Q} &= \mathcal{Q}_h + \widetilde{\mathcal{Q}}\end{aligned} \tag{2.7}$$

where the coarse scale (or FE) component is identified via the subscript h and the fine scale (or subgrid) component is identified via the superscript $(\sim)$.

Problem (2.5) can be rewritten as:

$$(\partial_t \mathbf{u}, \mathbf{v}) + B_\alpha (\mathbf{u}, p; \mathbf{v}, q) = (\mathbf{f}, \mathbf{v}) \tag{2.8}$$

where

$$B_\alpha (\mathbf{u}, p; \mathbf{v}, q) = (\boldsymbol{\alpha} \cdot \nabla \mathbf{u}, \mathbf{v}) + \nu (\nabla \mathbf{u}, \nabla \mathbf{v}) - (p, \nabla \cdot \mathbf{v}) + (q, \nabla \cdot \mathbf{u})$$

and $\boldsymbol{\alpha}$ is an advection velocity equal to $\boldsymbol{\alpha} = \mathbf{u}_h$ for linear or $\boldsymbol{\alpha} = \mathbf{u}_h + \widetilde{\mathbf{u}}$ for non-linear scale splitting (cf. [28]). Substituting (2.7) into (2.8) we obtain:

$$(\partial_t \mathbf{u}_h, \mathbf{v}_h) + B_\alpha (\mathbf{u}_h, p_h; \mathbf{v}_h, q_h) + (\partial_t \widetilde{\mathbf{u}}, \mathbf{v}_h) + B_\alpha (\widetilde{\mathbf{u}}, \widetilde{p}; \mathbf{v}_h, q_h) = (\mathbf{f}, \mathbf{v}_h), \tag{2.9}$$

for the FE component and

$$(\partial_t \mathbf{u}_h, \widetilde{\mathbf{v}}) + B_\alpha (\mathbf{u}_h, p_h; \widetilde{\mathbf{v}}, \widetilde{q}) + (\partial_t \widetilde{\mathbf{u}}, \widetilde{\mathbf{v}}) + B_\alpha (\widetilde{\mathbf{u}}, \widetilde{p}; \widetilde{\mathbf{v}}, \widetilde{q}) = (\mathbf{f}, \widetilde{\mathbf{v}}), \tag{2.10}$$

for the subgrid component, for all $(\mathbf{v}_h, q_h) \in \mathbf{V}_h \times \mathcal{Q}_h$ and $(\widetilde{\mathbf{v}}, \widetilde{q}) \in \widetilde{\mathbf{V}} \times \widetilde{\mathcal{Q}}$. If we perform an integration by parts on (2.9) we obtain:

$$\begin{aligned} (\partial_t \mathbf{u}_h, \mathbf{v}_h) + B_\alpha (\mathbf{u}_h, p_h; \mathbf{v}_h, q_h) + (\partial_t \widetilde{\mathbf{u}}, \mathbf{v}_h) + \\ (\widetilde{\mathbf{u}}, \mathcal{L}^* (\mathbf{v}_h, q_h)) - (\widetilde{p}, \nabla \cdot \mathbf{v}_h) = (\mathbf{f}, \mathbf{v}_h), \end{aligned} \tag{2.11}$$

where $\mathcal{L}^*$ is the adjoint of the operator $\mathcal{L}$, defined as:

$$\begin{aligned} \mathcal{L} (\mathbf{v}_h, q_h) &= -\nu \nabla^2 \mathbf{v}_h + \boldsymbol{\alpha} \cdot \nabla \mathbf{v}_h + \nabla q_h \\ \mathcal{L}^* (\mathbf{v}_h, q_h) &= -\nu \nabla^2 \mathbf{v}_h - \boldsymbol{\alpha} \cdot \nabla \mathbf{v}_h - \nabla q_h \end{aligned}$$

The convective form of the non-linear term has been used in the previous equations, which is probably the most frequent choice in computational practice and here it is referred to as the non-conservative form. Using (2.2) other forms of the non-linear term can be derived which are equivalent at the continuous level but have different properties at the discrete level. The skew-symmetric form:

$$C_{\text{skew}}(\boldsymbol{\alpha}, \mathbf{u}, \mathbf{v}) = (\boldsymbol{\alpha} \cdot \nabla \mathbf{u}, \mathbf{v}) + \frac{1}{2} (\nabla \cdot \boldsymbol{\alpha}, \mathbf{u} \cdot \mathbf{v}) \tag{2.12}$$

has the advantage that it conserves kinetic energy at the discrete level and is commonly used in numerical analysis and direct numerical simulations (DNS) and large-eddy simulations (LES), where energy conservation provides enhanced results.

Considering that the subgrid scale equations cannot be directly solved, we approximate the values of the subscales through the following equations:

$$\partial_t \widetilde{\mathbf{u}} + \frac{1}{\tau_1}\widetilde{\mathbf{u}} = \mathcal{P}\left(\mathbf{R}_m\right) \tag{2.13}$$

$$\frac{1}{\tau_2}\widetilde{p} = \mathcal{P}\left(R_c\right) \tag{2.14}$$

where

$$\mathbf{R}_m = \mathbf{f} - \partial_t \mathbf{u}_h - \mathcal{L}\left(\mathbf{u}_h, p_h\right) \tag{2.15}$$

$$R_c = -\nabla \cdot \mathbf{u}_h \tag{2.16}$$

are the residuals of the momentum and continuity equations respectively, and $\mathcal{P}$ is their projection onto the space of the subscales. Defining $\mathcal{P} = I$ leads to the Algebraic Subgrid Scale (ASGS) method, whereas $\mathcal{P} = \Pi_h^{\perp}$ results in the Orthogonal Subscale (OSS) method [24, 29], where the space of the subscales is chosen to be orthogonal to the finite element space. Using a heuristic Fourier analysis for the subscale problem [24], the stabilization parameters τ_1 and τ_2 can be approximated as follows:

$$\tau_1 = \left[c_1 \frac{\nu}{h^2} + c_2 \frac{|\boldsymbol{\alpha}|}{h}\right]^{-1} \tag{2.17}$$

$$\tau_2 = \frac{h^2}{c_1 \tau_1} = \nu + \frac{c_2}{c_1}|\boldsymbol{\alpha}|h \tag{2.18}$$

where c_1 and c_2 are algorithmic constants and h denotes the mesh size. It must be noted that expressions where τ_1 depends on the time-step δt are also common in literature [28, 39, 40].

The subscales can be categorized into quasi-static or dynamic, depending on whether the temporal derivative of the subscales in (2.13) is neglected or not. Considering the subscales to be time-dependent has shown to offer improved stability over the pressure without restrictions on the time-step size as well as improved accuracy. It also allows for commutativity of the space and time discretization [28, 41]. The subscales can also be classified as linear or non-linear, depending on the definition of the advection velocity $\boldsymbol{\alpha}$ (where, as stated earlier, $\boldsymbol{\alpha} = \mathbf{u}_h$ leads to linear and $\boldsymbol{\alpha} = \mathbf{u}_h + \widetilde{\mathbf{u}}$ to non-linear subscales). Nonlinear scale splitting is shown to lead to global conservation of momentum [28].

In order to understand the impact of the algorithmic constants c_1 and c_2, we first need to derive the expression for the numerical dissipation introduced by the formulation. The energy balance statement for the finite element component, when dynamic subscales are used, can be obtained by substituting $\mathbf{v}_h = \mathbf{u}_h$ and $q_h = p_h$ in Eq. 2.11:

$$\begin{aligned} &\frac{1}{2} d_t ||\mathbf{u}_h||^2 + \nu ||\nabla \mathbf{u}_h||^2 + (\boldsymbol{\alpha} \cdot \nabla \mathbf{u}_h, \mathbf{u}_h) \\ &\qquad + \Big[(\partial_t \widetilde{\mathbf{u}}, \mathbf{u}_h) + (\widetilde{\mathbf{u}}, \mathcal{L}^*\left(\mathbf{u}_h, p_h\right)) - (\widetilde{p}, \nabla \cdot \mathbf{u}_h) \Big] = (\mathbf{f}, \mathbf{u}_h) \end{aligned} \tag{2.19}$$

where $||\cdot||$ denotes the L^2 norm. The expression in brackets in Eq. 2.19 corresponds to the energy transfer from the finite element scales to the subscales, which is equivalent to the numerical dissipation of the method ε_{num}. Rewriting Eq. 2.13 and 2.14 as:

$$\begin{aligned}\widetilde{\mathbf{u}} &= \tau_1 \left(\mathcal{P}\left(\mathbf{R}_m\right) - \partial_t \widetilde{\mathbf{u}}\right) \\ \widetilde{p} &= \tau_2 \mathcal{P}\left(R_c\right)\end{aligned}$$

and substituting them into the bracketed expression, using also Eq. 2.15 and 2.16, leads to:

$$\begin{aligned}\varepsilon_{\text{num}} = \left(\partial_t \widetilde{\mathbf{u}}, \mathbf{u}_h\right) - \left(\tau_1 \partial_t \widetilde{\mathbf{u}}, \mathcal{L}^*\left(\mathbf{u}_h, p_h\right)\right) - \left(\tau_1 \partial_t \mathbf{u}_h, \mathcal{L}^*\left(\mathbf{u}_h, p_h\right)\right) \\ - \left(\tau_1 \mathcal{L}\left(\mathbf{u}_h, p_h\right), \mathcal{L}^*\left(\mathbf{u}_h, p_h\right)\right) + \tau_2 ||\mathcal{P}\nabla \cdot \mathbf{u}_h||^2\end{aligned} \tag{2.20}$$

where the last two terms are positive and, therefore, dissipative, excluding the viscous contribution. It can, thus, be seen that increasing either τ_1 or τ_2 generally results in a more dissipative behavior. Using the expressions from Eq. 2.17 and 2.18, we can observe that larger values of c_1 lead to lower τ_1 and τ_2 (or, equivalently, lower dissipation), while increasing c_2 results in reduced τ_1 but increased τ_2. It is also important to note that the first three terms can be negative, allowing for the possibility of predicting backscatter effects [30, 31].

Typically, the values considered for the algorithmic constants are $c_1 = 4$ and $c_2 = 2$ (see for example [29, 30]). Recently, Colomés et al. [42] examined the influence of the algorithmic constants on the numerical dissipation of the formulation. It is pointed out that τ_2 is not necessary for the stabilization of the pressure, and can therefore be taken equal to zero. In other words, we can consider $p \approx p_h$, with the pressure subscale being $\widetilde{p} \approx 0$. This choice, which leads to a less dissipative method, is seen to offer improved accuracy in the results. Similar behavior is observed when the value of c_1 is increased to $c_1 = 12$ [43, 44]. This is consistent with the behavior observed in our numerical experiments, and, therefore, the values $c_1 = 12$ and $\tau_2 = 0$ have been used in this chapter. However, the situation is not as clear in regards to the value of the constant c_2. In fact, different values of the constant perform better in different types of flows. To that end, we consider both $c_2 = 2$ and $c_2 = 8$ in the numerical problems examined in this chapter. It should also be noted that the numerical dissipation of the formulation directly depends on the element size h, through Eq. 2.17 and Eq. 2.18. The specification of h is not trivial for anisotropic elements. Nevertheless, in the numerical examples of this chapter, the minimum size characterizing an element is used, with the aim of reducing the numerical dissipation.

Backward differencing schemes are used for the time discretization of equations (2.11) and (2.13). More specifically a second order backward differentiation formula (BDF2) is used to discretize equation (2.11):

$$\partial_t \mathbf{u}_h^{n+1} = \frac{3\mathbf{u}_h^{n+1} - 4\mathbf{u}_h^n + \mathbf{u}_h^{n-1}}{2\delta t}, \tag{2.21}$$

while a first order backward differentiation formula (also known as Backward Euler method) is used in equation (2.13) in the case of dynamic subscales:

$$\partial_t \mathbf{u}_h^{n+1} = \frac{\mathbf{u}_h^{n+1} - \mathbf{u}_h^n}{\delta t}, \tag{2.22}$$

where δt denotes the time step. As seen in Eq. 2.21 and 2.22, this temporal scheme is implicit, since the solution depends on the unknown at the current time step. Implicit schemes are known to have unconditional stability at large values of the time step, however they require an iterative method for the solution of the linear system, leading to a higher computational cost per time step.

It is important to note at this point, that the formulation presented above can be classified as an implicit large-eddy simulation method since it relies on numerical dissipation to model the effect of the subscales, without introducing any turbulent viscosity to the continuous problem. It can be shown that, when the OSS method is used in conjunction with dynamic and non-linear subscales, it produces a numerical dissipation that is proportional to the molecular one [32] and it offers the possibility of predicting backscatter [30, 31]. Therefore, the OSS method with dynamic and non-linear subscales has been used in the examples presented in this chapter. Additionally, the skew-symmetric form of the convective term (2.12) has been used in order to conserve kinetic energy at the discrete level.

2.3 Low-Dissipation formulation

In the context of this thesis, where the LES framework aims to be applicable over a wide range of engineering flows (e.g. aeronautics, combustion, fluid-structure interaction), the formulation needs to be simple to implement and use without depending on a plethora of parameters. It can be argued that the Variational Multiscale method presented in the previous section does not necessarily meet the aforementioned criteria. The amount of different options in regards to the treatment of the subscales, as well as the dependence of the numerical dissipation on algorithmic constants, significantly increase the complexity of the method and its implementation. Additionally, stabilization mechanisms associated with a numerical dissipation might add a non-physical damping mechanism to the discretized equations [45, 46]. Although this damping might be accepted in laminar or time-average flows, it might interfere with the energy cascade in turbulent flows. To that end, a new formulation is proposed. The formulation offers low numerical dissipation by construction, with a physical subgrid scale model accounting for the effect of the unresolved scales. It relies on a simple fractional step scheme to stabilize the pressure, making it straightforward to implement.

Recently, Charnyi et al. [47] presented a new formulation in the finite element context that preserves energy at the inviscid limit, momentum, angular

momentum, enstrophy in two-dimensions, helicity and vorticity without the strong enforcement of the divergence constraint. They tested their formulation using mixed finite elements in laminar two- and three-dimensional flows and proved that none of the commonly used formulations conserves energy, momentum and angular momentum. Following Charnyi et al. [47] work, an extension of the conservative formulation to equal order finite elements for use in turbulent flows is presented. A non-incremental fractional step method is used to stabilize the pressure, whereas for the explicit time integration of the set of discrete equations, the energy conserving explicit Runge-Kutta method recently proposed by Cappuano et al. [48] is combined with an eigenvalue-based time-step estimator [49].

Let us consider the matrix form of the momentum and continuity equations:

$$\mathrm{M}\partial_t \mathrm{U} + \mathrm{K(U)U} + \mathrm{GP} = \mathrm{R_m}, \tag{2.23}$$

$$\mathrm{DU} = \mathrm{R_c}, \tag{2.24}$$

where U, P are the arrays of the nodal unknowns for $\mathbf{u}$ and p respectively. If we denote the node indexes with superscripts a, b, the space indexes with subscripts i, j and the standard shape functions of node a with N^a, the components of the matrices involved in the previous equations are:

$$\mathrm{M}_{ij}^{ab} = \left(N^b, N^a\right)\delta_{ij}, \tag{2.25}$$

$$\mathrm{K}\left(\mathrm{U}^{\mathrm{n+1}}\right) = \mathrm{K_{CONV}(U)} + \mathrm{K_{VISC}(U)}, \tag{2.26}$$

$$\mathrm{K_{VISC}}\left(\mathrm{U}^{\mathrm{n+1}}\right)_{ij}^{ab} = \left(\nu\boldsymbol{\varepsilon}\left(N^b\right), \boldsymbol{\varepsilon}\left(N^a\right)\right)\delta_{ij}, \tag{2.27}$$

$$\begin{aligned}\mathrm{K_{CONV}}\left(\mathrm{U}^{\mathrm{n+1}}\right)_{ij}^{ab} = &\left(\mathbf{u}_h\cdot\nabla N^b, N^a\right)\delta_{ij} + \left(\partial_i N^b u_h^j, N^a\right) + \\ &\left(\left(\nabla\cdot\mathbf{u}_h\right)N^b, N^a\right)\delta_{ij} - \frac{1}{2}\left(\partial_i u_h^j N^b, N^a\right),\end{aligned} \tag{2.28}$$

$$\mathrm{G}_i^{ab} = -\left(N^b, \partial_i N^a\right), \tag{2.29}$$

$$\mathrm{D}_j^{ab} = \left(\partial_j N^b, N^a\right), \tag{2.30}$$

where δ_{ij} is the Kronecker δ. u_h^j is used to denote component j of vector $\mathbf{u}_h$.

The energy, momentum and angular momentum conserving (EMAC) form of the convective term, recently proposed in [47], has been introduced in Eq. 2.28:

$$C_{\mathrm{emac}}(\mathbf{u}) = 2\mathbf{u}\cdot\boldsymbol{\varepsilon}(\mathbf{u}) + (\nabla\cdot\mathbf{u})\mathbf{u} - \frac{1}{2}\nabla|\mathbf{u}|^2, \tag{2.31}$$

which, as its name indicates, additionally conserves linear and angular momentum at the discrete level even if the conservation of mass is enforced only weakly like in the case of stabilizing the continuity equation.

In the aforementioned publication, the last term of Eq. 2.31 was absorbed in the pressure by redefining the pressure as $p^* := p - \frac{1}{2}|\mathbf{u}|^2$ which, in physical terms, has no meaning. We have rather chosen to include it explicitly in the formulation, to avoid having to implement non-physical Neumann conditions at outflow boundaries. With this choice, Eq. 2.3 coincides with the natural condition of the weak formulation (Eq. 2.5).

The matrices are obtained by grouping together the left indexes in the previous expressions (a and possibly i) and the right indexes in the previous expressions (b and possibly j). The vectors $\mathrm{R_c}$ and $\mathrm{R_m}$ include terms coming from the application of the Dirichlet boundary conditions and the latter also includes the contribution from the volumetric forces.

Since an explicit time discretization is used, the mass matrix is lumped to avoid the solution of a linear system for the velocity as is usually done for explicit schemes in the finite element context. From now onwards M will refer to the lumped mass matrix.

The momentum equation can be rewritten as:

$$\mathrm{M}\partial_t \mathrm{U} = \mathrm{F} - \mathrm{GP} \tag{2.32}$$

defining

$$\mathrm{F} = -\mathrm{KU} + \mathrm{R_m}. \tag{2.33}$$

Starting from equations 2.24 and 2.32, time discretization using an explicit Runge-Kutta scheme and imposition of a divergence-free constraint with a fractional step scheme [50] implies solving the following equations:

$$\mathrm{U}^{i,*} = \mathrm{U}^n + \delta t \mathrm{M}^{-1} \sum_{j=1}^{i} \alpha_{ij} \mathrm{F}^j, \tag{2.34}$$

$$\mathrm{DM}^{-1}\mathrm{G}\left(\Phi^i\right) = \frac{1}{c_i \delta t}\left(\mathrm{DU}^{\mathrm{i},*} - \mathrm{R_c}\right), \tag{2.35}$$

$$\mathrm{U}^i = \mathrm{U}^{i,*} - c_i \delta t \mathrm{M}^{-1}\mathrm{G}\left(\Phi^i\right), \tag{2.36}$$

for substeps $i = 2, s$ (for the first substep, $\mathrm{U}^1 = \mathrm{U}^n$) and finally obtaining the unknowns at the new step from:

$$\mathrm{U}^{n+1,*} = \mathrm{U}^n + \delta t \mathrm{M}^{-1} \sum_{i=1}^{s} b_i \mathrm{F}^i, \tag{2.37}$$

$$\mathrm{DM}^{-1}\mathrm{G}\left(\Phi^{n+1}\right) = \frac{1}{\delta t}\left(\mathrm{DU}^{\mathrm{n+1},*} - \mathrm{R_c}\right), \tag{2.38}$$

$$\mathrm{U}^{n+1} = \mathrm{U}^{n+1,*} - \delta t \mathrm{M}^{-1}\mathrm{G}\left(\Phi^{n+1}\right), \tag{2.39}$$

where α_{ij}, b_i and $c_i = \sum_j \alpha_{ij}$ are the coefficients of the Runge-Kutta scheme, δt is the time-step size and the pseudo-pressure, Φ, is a first order approximation to the pressure:

$$\Phi = \mathrm{P} + \mathcal{O}(\delta t). \tag{2.40}$$

In spite of this approximation, the accuracy in the velocity is not affected and it depends on the accuracy of the Runge-Kutta used. If one is interested in obtaining pressure with the same temporal accuracy as the velocity, an additional Poisson equation needs to be solved [51]. This is not explored here.

Explicit Runge-Kutta schemes do not conserve energy [51], [48]. Classical explicit Runge-Kutta of order $p \leqslant 4$, with s stages, introduces an error in the energy conservation of order

$$\frac{\Delta E}{\Delta t} = \mathcal{O}\left(\delta t^q\right),$$

such that $p = s = q$. Here p and q denote the order of accuracy on the solution and the conservation of kinetic energy respectively, while s refers to the number of stages of the Runge-Kutta scheme. Alternative schemes which increase q at the expense of p for a certain s are presented in [48]. The present work uses the 3p5q(4) scheme proposed in [48]. The Butcher tableau for this 4-stage scheme is:

0	0			
$\frac{c_3-1}{4c_3-3}$	$\frac{c_3-1}{4c_3-3}$	0		
c_3	$c_3 - \frac{(2c_3-1)(4c_3-3)}{2(c_3-1)}$	$\frac{(2c_3-1)(4c_3-3)}{2(c_3-1)}$	0	
1	$-\frac{(2c_3-1)^2}{2(c_3-1)(4c_3-3)}$	$\frac{6c_3^2-8c_3+3}{2(c_3-1)(2c_3-1)}$	$\frac{c_3-1}{(2c_3-1)(4c_3-3)}$	0
	$\frac{1}{12(c_3-1)}$	$\frac{(4c_3-3)^2}{12(c_3-1)(2c_3-1)}$	$-\frac{1}{12(c_3-1)(2c_3-1)}$	$\frac{4c_3-3}{12(c_3-1)}$

where $c_3 = 1/4$ has been selected, following the recommendation in [48].

The efficient self-adaptive strategy for the explicit time-integration of Navier-Stokes equations proposed by Trias & Lehmkuhl [49] is adapted here to finite elements and the Runge-Kutta method. Unlike the conventional explicit integration schemes, it is not based on a standard CFL condition. Instead, the eigenvalues of the dynamical system are analytically bounded and the linear stability domain of the time-integration scheme is adapted in order to maximize the time-step.

Following the original work of Trias & Lehmkuhl [49], the eigenvalues of the dynamical system can be approximated using the discrete properties

of the matrices $\mathrm{K_{CONV}}$ and $\mathrm{K_{VISC}}$ (i.e., $\mathrm{K_{CONV}} = -\mathrm{K_{CONV}^T}$ and $\mathrm{K_{VISC}} = \mathrm{K_{VISC}^T}$). Therefore, by means of the Geshgorin circle theorem one can find the following expression for the bounding eigenvalues:

$$|\lambda_k^{\mathrm{K_{CONV}}}| \leqslant \sum_{i \neq j} |\mathrm{K_{CONV}} \left(\mathrm{U}^n\right)_{ij}| \tag{2.41}$$

$$|\lambda_k^{\mathrm{K_{VISC}}}| \leqslant 2\mathrm{K_{VISC}} \left(\mathrm{U}^n\right)_{ii} \tag{2.42}$$

In order to approximate the $\mathrm{K_{VISC}}$ and $\mathrm{K_{CONV}}$ matrices, one can use expressions 2.27 and 2.28 respectively at the gravity center of each element at the beginning of the time step n+1, with the velocity values of the previous time step n. Then, using a numerical solution for the region of absolute stability of an explicit Runge-Kutta with $p = 3$,

$$|R(z)| = |1 + z + \frac{z^2}{2} + \frac{z^3}{6}| = e^{i\varphi} \tag{2.43}$$

and evaluating the phase angle as:

$$\varphi = \frac{\pi}{2} - \mathrm{atan} \left(\frac{\max\left(\lambda_k^{\mathrm{K_{VISC}}}\right)}{\max\left(\lambda_k^{\mathrm{K_{CONV}}}\right)} \right) \tag{2.44}$$

the optimal $\delta t_{opt}\left(\varphi\right)$ is obtained. A safety factor of $C_{\delta t} = 0.9$ is adopted for all the simulations in this chapter; therefore, the simulation time step for $n + 1$ is defined as $\delta t = C_{\delta t} \delta t_{opt}\left(\varphi\right)$.

The use of the discrete Laplacian $\mathrm{DM^{-1}G}$, is relatively expensive even if a diagonal mass matrix is used. Therefore, when continuous pressure interpolations are used, it is usually approximated as:

$$\mathrm{DM^{-1}G} \approx \mathrm{L}, \quad \text{with components } \mathrm{L}^{ab} = -\left(\nabla N^a, \nabla N^b\right). \tag{2.45}$$

Moreover, this approximation introduces a stabilizing effect for the pressure that allows to use finite element pairs that do not satisfy the inf-sup condition [52], such as equal order interpolation for velocity and pressure used in this work (known as collocated schemes in the finite volume and finite difference communities). As shown by Codina [52], the approximation introduces a stabilizing term of the form $\delta t \mathrm{B}\Phi$ where $\mathrm{B} = \mathrm{DM^{-1}G} - \mathrm{L}$. In Codina & Blasco [53] it is shown that approximation 2.45 introduces an error of the same order as the pressure interpolation $\left(\mathcal{O}\left(h^{k+1}\right)\right)$, where k is the degree of the finite element shape functions and h is the element size, and thus it does not deteriorate the accuracy of the finite element approximation. The equations for the pseudo-pressure 2.35 and 2.38 are replaced by:

$$\mathrm{L}(\Phi^{\mathrm{i}}) = \frac{1}{c_i \delta t} \mathrm{DU^{i,*}}, \tag{2.46}$$

$$\mathrm{L}(\Phi^{\mathrm{n}+1}) = \frac{1}{\delta t}\mathrm{DU}^{\mathrm{n}+1,*}. \tag{2.47}$$

Starting from Eq. 2.36

$$\mathrm{U}^{\mathrm{i},*} = \mathrm{U}^{\mathrm{i}} + c_i \delta t \mathrm{M}^{-1}\mathrm{G}(\Phi^{\mathrm{i}}) \tag{2.48}$$

is obtained, which can be introduced in Eq. 2.35 to end up with:

$$\mathrm{DU}^{\mathrm{i}} + c_i \delta t \mathrm{B}\Phi^{\mathrm{i}} = \mathrm{R}_{\mathrm{c}}. \tag{2.49}$$

For time step $n+1$, from Eq. 2.39 and 2.47,

$$\mathrm{DU}^{\mathrm{n}+1} + \delta t \mathrm{B}\Phi^{\mathrm{n}+1} = \mathrm{R}_{\mathrm{c}} \tag{2.50}$$

is obtained. The second term in the left hand side of Eq. 2.49 and 2.50 is the perturbation to the incompressibility constraint introduced by replacing the discrete Laplacian with a continuous one.

In order to obtain an equation for the evolution of the kinetic energy one can take $\mathbf{v}_h = \mathbf{u}_h$ and $q_h = p_h$ in Eq. 2.6 or, equivalently, premultiply Eq. 2.23 by U^T and Eq. 2.24 by P^T and add both equations. In the case of the Runge-Kutta scheme, Φ^T is used instead of P^T. The perturbation to the incompressibility constraint introduced by replacing the discrete Laplacian with a continuous one results in a dissipation $c_i \delta t \left(\Phi^i\right)^T \mathrm{B}\Phi^{\mathrm{i}}$ at each substep and a dissipation $\delta t \left(\Phi^{n+1}\right)^T \mathrm{B}\Phi^{\mathrm{n}+1}$ at the new time step. The error in the conservation of kinetic energy introduced by the approximation is then of $\mathcal{O}\left(\delta t, h^{k+1}\right)$. In the case of linear finite elements ($k = 1$), this coincides with the error obtained for finite volumes using a collocated scheme in [54], [55].

Finally, the explicit low-dissipation formulation implementation is summarized in the following algorithm:

The Vreman model [8] is used for modelling the subgrid stress term resulting from the spatial filtering of the Navier-Stokes equations. It calculates the turbulent eddy viscosity through the following expression:

$$\nu_t = c\sqrt{\frac{B_\beta}{\alpha_{ij}\alpha_{ij}}} \tag{2.51}$$

where

$$\alpha_{ij} = \partial_i \overline{u}_j = \frac{\partial \overline{u}_j}{\partial x_i} \tag{2.52}$$

is the resolved velocity gradient tensor and

$$B_\beta = \beta_{11}\beta_{22} - \beta_{12}^2 + \beta_{11}\beta_{33} - \beta_{13}^2 + \beta_{22}\beta_{33} - \beta_{23}^2 \tag{2.53}$$

is the second invariant of tensor

$$\beta_{ij} = \Delta_k^2 \alpha_{ki}\alpha_{kj}. \tag{2.54}$$

Algorithm 1 Low-dissipation formulation algorithm

```
t = t_0;
while t ⩽ t_f do
  Evaluate the new δt = C_δt δt_opt (φ) using equations 2.41-2.44
  t = t + δt;
  i = 2;
  U^1 = U^n;
  while i ⩽ s do
    Evaluate U^{i,*} using equation 2.34
    Evaluate Φ^i solving equation 2.35
    Evaluate U^i by means of equation 2.36
    i = i + 1;
  end while
  Evaluate U^{n+1,*} using equation 2.37
  Evaluate Φ^{n+1} solving equation 2.38
  Evaluate U^{n+1} by means of equation 2.39
end while
```

Finally Δ denotes the filter width and c is the constant model, chosen to be $c = 0.1$ in the examples presented here, following the recommendation by the author for complex cases. Here, the filter width is equal to the cubic root of the element volume $\Delta = \sqrt[3]{V_{\text{elem}}}$.

2.4 Comparison between the formulations

Having presented the two formulations, it is important to perform some comparative tests and justify our choice for the more complex problems presented in the later chapters. To that end, tests in three very common benchmark cases are performed: 1) the Decaying Isotropic Turbulence (DIT) case, 2) the Taylor-Green Vortex (TGV) case and 3) the Turbulent Channel Flow (TCF). The low-dissipation formulation is denoted by "LD method" in the results presented in this section.

2.4.1 Decaying Isotropic Turbulence

This fundamental benchmark case analyzes the evolution of the homogeneous decaying isotropic turbulence at $Re = 4.209 \times 10^5$. Through this case, the capability of the formulation to predict the energy cascade is evaluated. The computational domain consists of a cube with a side length of 2π and periodic boundary conditions on each direction. The domain is discretized through 32^3 and 64^3 grids. An initial velocity field is obtained through the inverse Fourier transformation of the experimental data from [56]. The flow is allowed to evolve until a non-dimensional time $t = 2.0$, at which point the

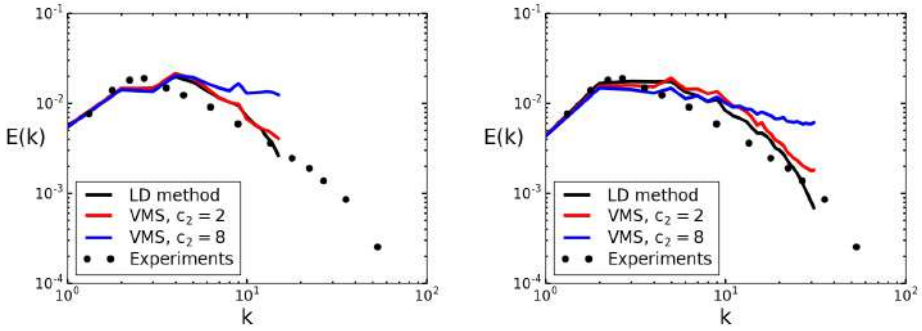

(a) 32^3 (b) 64^3

Figure 2.1: Decaying isotropic turbulence. Energy spectra versus wavenumber k for the 32^3 (a) and 64^3 (b) grids at t=2.0.

results are again compared with the experimental data. The energy spectra for both grids are presented in Fig. 2.1. Both the low-dissipation formulation as well as the VMS with $c_2 = 2$ provide a fairly accurate prediction of the energy cascade, with the former showing a slightly overdissipative behavior at the very high wavenumbers. However, when the algorithmic constant is increased to $c_2 = 8$, a much less dissipative behavior from the VMS is observed, which completely fails to capture the energy cascade in the higher wavenumbers. This is consistent with the findings presented in [42].

2.4.2 Taylor-Green Vortex

The Taylor-Green Vortex (TGV) is a canonical problem formulated to address the study of the turbulence dynamics, the enhancement of vorticity by vortex-stretching and the consequent energy transfer to smaller eddies [57]. The problem proposed consists of an incompressible flow in a three-dimensional periodic cubic domain of side 2π in which the initial velocity field is given by:

$$\begin{aligned} u &= U_0 \sin\frac{x}{L}\cos\frac{y}{L}\cos\frac{z}{L} \\ v &= -U_0 \cos\frac{x}{L}\sin\frac{y}{L}\cos\frac{z}{L} \\ w &= 0 \end{aligned} \tag{2.55}$$

and the pressure is obtained from the solution of the Poisson equation for the given velocity field:

$$p = p_0 + \frac{\rho_0 U_0^2}{16}\left(\cos\left(\frac{2x}{L}\right) + \cos\left(\frac{2y}{L}\right)\right)\left(\cos\left(\frac{2z}{L}\right) + 2\right) \tag{2.56}$$

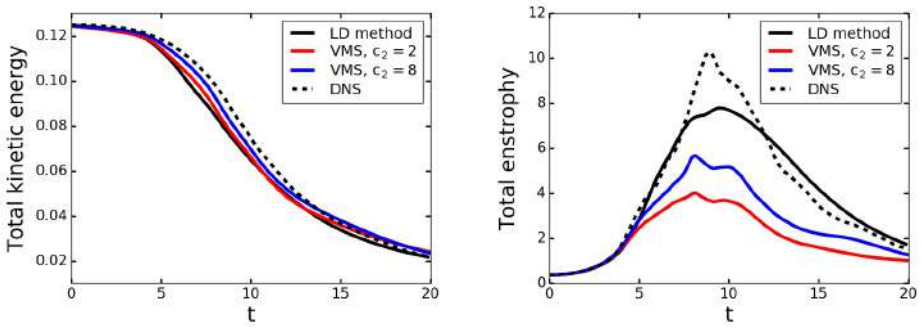

(a) (b)

Figure 2.2: Results for the TGV benchmark, using a 64^3 grid. a) Temporal evolution of the kinetic energy as a function of the dimensionless time. b) Temporal evolution of the enstrophy integrated over the domain as a function of the dimensionless time.

where $L = 1$, $U_0 = 1$, $\rho_0 = 1$ and $p_0 = 0$. In the present problem, the Reynolds number, defined in terms of the initial velocity U_0 and the side of the domain L, is set to $Re = U_o L/\nu = 1600$. The problem is solved using grids of 64^3, 128^3 and 256^3 degrees of freedom and the flow is simulated for $t = 20t_c$, where t_c is the characteristic convective time $t_c = U_0/L$. The numerical results presented here are compared to the direct numerical simulation of Van Rees et al. [58] obtained with a pseudo-spectral code on a computational mesh of 512^3.

The temporal evolution of the volume-averaged kinetic energy:

$$E_k = \frac{1}{\rho_0 V}\int_V \frac{1}{2}\rho \mathbf{u}\cdot\mathbf{u} dV \tag{2.57}$$

and the integrated enstrophy:

$$\zeta = \frac{1}{\rho_0 V}\int_V \frac{1}{2}\rho \boldsymbol{\omega}\cdot\boldsymbol{\omega} dV \tag{2.58}$$

as a function of the dimensionless time t are presented for each grid in Fig. 2.2-2.4. It is immediately obvious that while the low-dissipation formulation predicts a slightly higher dissipation for the kinetic energy, it performs significantly better in predicting the evolution of the enstrophy, which can be directly related to the vorticity-based dissipation [59], especially in the coarser grids. All the methods converge towards the reference DNS when using the 256^3 grid, since the accuracy depends more on the mesh size than the method at such fine grids. It must be noted that both formulations produce results of significantly higher quality compared to the low-order codes presented in [60], which is especially true in the case of the low-dissipation formulation.

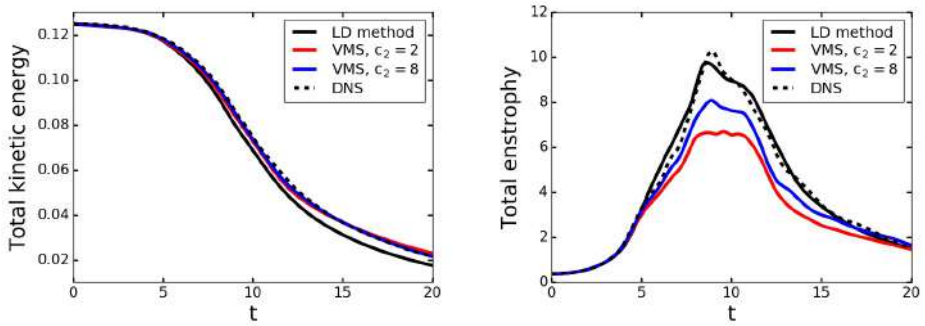

(a) (b)

Figure 2.3: Results for the TGV benchmark, using a 128^3 grid. a) Temporal evolution of the kinetic energy as a function of the dimensionless time. b) Temporal evolution of the enstrophy integrated over the domain as a function of the dimensionless time.

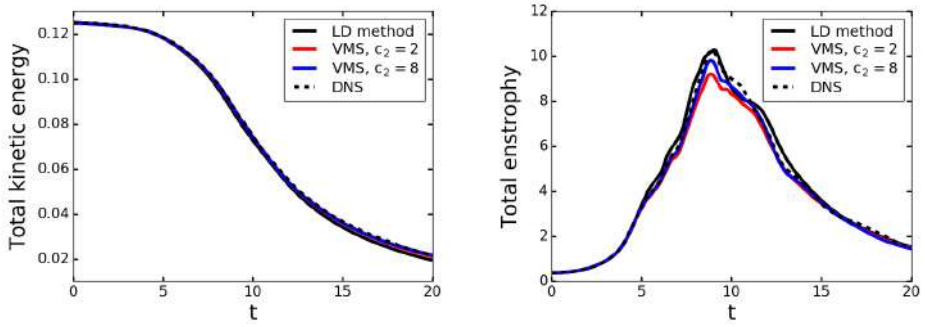

(a) (b)

Figure 2.4: Results for the TGV benchmark, using a 256^3 grid. a) Temporal evolution of the kinetic energy as a function of the dimensionless time. b) Temporal evolution of the enstrophy integrated over the domain as a function of the dimensionless time.

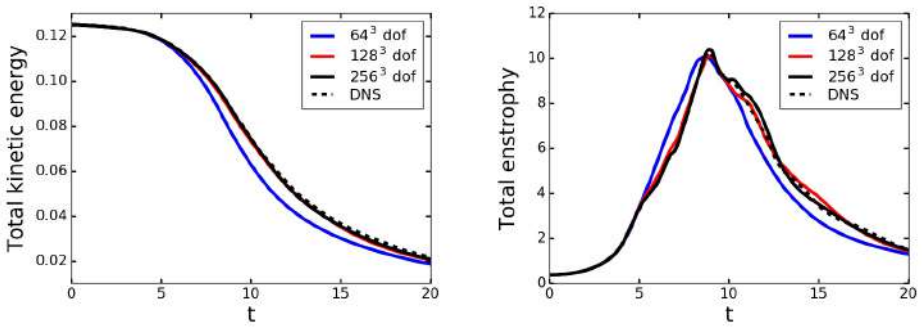

(a) (b)

Figure 2.5: Results for the TGV benchmark, using the low-dissipation formulation and quadratic (Q2) elements. a) Temporal evolution of the kinetic energy as a function of the dimensionless time. b) Temporal evolution of the enstrophy integrated over the domain as a function of the dimensionless time.

Nevertheless, it is very important to note that, unlike the DIT case (Section 2.4.1), the VMS method provides notably better results with $c_2 = 8$, compared to $c_2 = 2$, which is a very undesirable behavior, since it points towards an ad hoc tuning of the constants, depending on the case examined. In [42], it is argued that $c_2 = 2$ is more appropriate for homogeneous turbulence, i.e. the DIT and TGV cases, however, it is quite evident from Fig. 2.2-2.4, that this is not the case for the TGV problem.

Fig. 2.5 presents results from the low-dissipation formulation, using quadratic elements. It can be observed that when using high order elements, the results are notably improved compared to linear elements for the same number of degrees of freedom (dof). In fact, the predictions are in very good agreement with the reference data for all three meshes. Especially the results from the finer meshes (128^3 and 256^3 dof) are almost identical to the DNS.

Vortical structures identified by Q-isosurfaces [61] are presented in Fig. 2.6, as predicted by the low-dissipation formulation. It can be seen that the flow is still organized at $t/t_c = 4$, however the vortex-stretching process activates the energy cascade and the flow breaks down into smaller and smaller scales ($t/t_c \geqslant 8$).

2.4.3 Turbulent Channel Flow at $Re_\tau = 395$

In this section we perform LES of the turbulent flow in a plane channel at $Re_\tau = 395$, where Re_τ denotes the friction Reynolds number, defined in terms of the friction velocity u_τ and channel half-height δ.

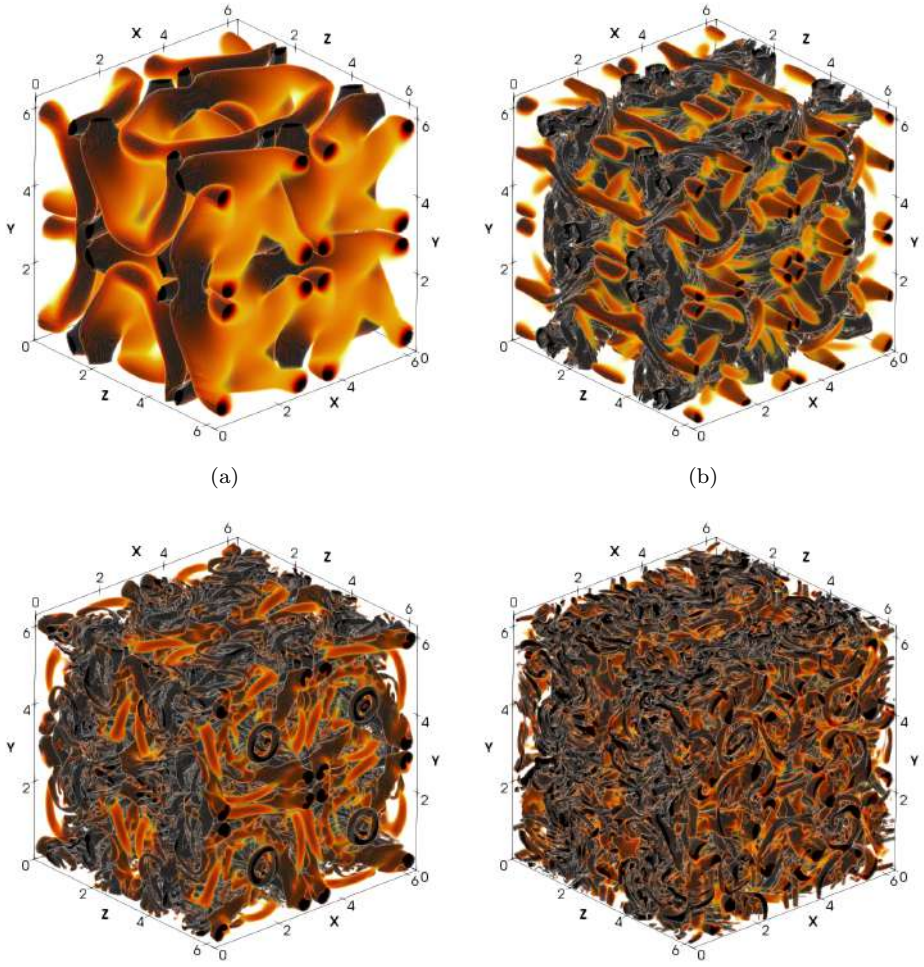

Figure 2.6: Taylor-Green vortices. Instantaneous vortical structures represented by volumetric Q-isocontours, $Q = 0 - 0.5$ (a darker colour represents a higher level of Q) (a) $t/t_c = 4$, (b) $t/t_c = 8$, (c) $t/t_c = 12$, (d) $t/t_c = 16$.

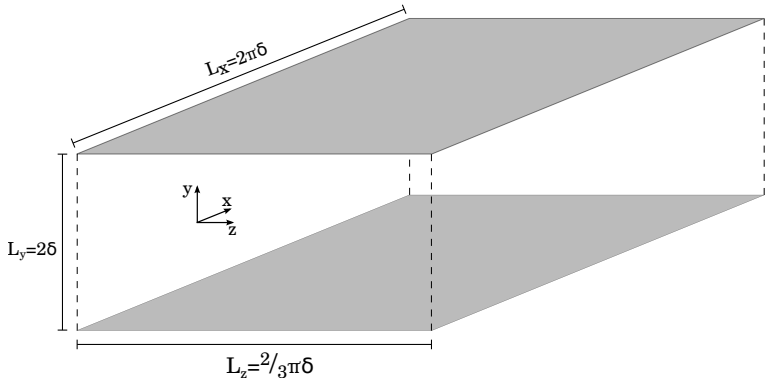

Figure 2.7: Computational domain for the turbulent channel case at $Re_\tau = 395$.

The size of the computational domain considered herein is $2\pi\delta \times 2\delta \times 2/3\pi\delta$ in the streamwise, wall-normal and spanwise directions respectively. The geometry of the channel is presented in Fig. 2.7. The streamwise and spanwise directions are assumed to be homogeneous, and thus periodic boundary conditions are applied, while a no penetration condition is imposed on the wall boundaries.

A mesh of 32^3 elements has been used with uniform distribution in the tangential directions, while a hyperbolic tangent function has been used in the wall-normal direction:

$$y(i) = \frac{\tanh\left(\gamma\left(\frac{2(i-1)}{N_y} - 1\right)\right)}{\tanh(\gamma)} \tag{2.59}$$

where $i = 1, ..., N_y$ with N_y being the number of nodes in the wall-normal direction and γ the concentration factor, here $\gamma = 2.75$. This results in the first grid point off the wall being located at $y^+ = 1.3$, while at the center of the channel $\Delta x^+ = 77.6$, $\Delta y^+ = 67.8$ and $\Delta z^+ = 25.9$ resulting in fairly isotropic elements.

The results are compared with the DNS data of [62]. The reference DNS used a $256 \times 193 \times 192$ mesh on a domain with size $2\pi\delta \times \delta \times \pi\delta$. The flow is driven by a constant pressure gradient in the streamwise direction.

The simulation is run for an appropriately long time to guarantee that a statistically stationary regime is reached. Once that quasi-steady state has been achieved, statistics are collected, and the results are averaged in time for approximately 24 flow-through units (we define a flow-through unit as $t = L_x/U$ where U denotes the velocity at the center of the channel and L_x is the size of the domain in the streamwise direction). They are subsequently averaged in space (in the streamwise and spanwise direction) and non-dimensionalized using the computed friction velocity.

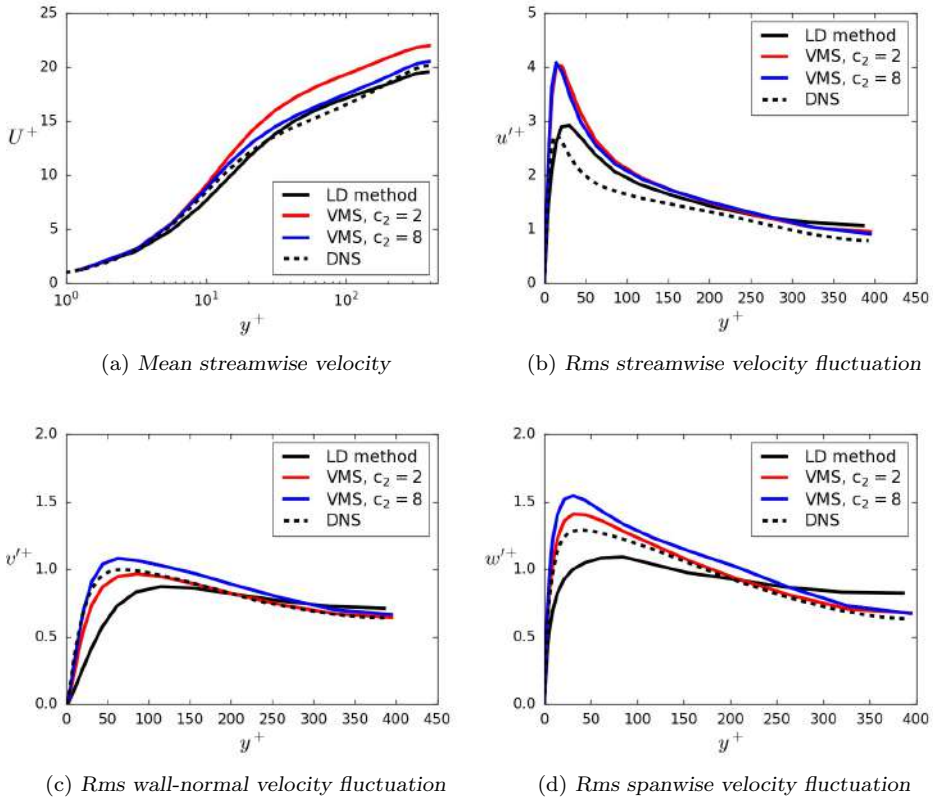

(a) *Mean streamwise velocity*

(b) *Rms streamwise velocity fluctuation*

(c) *Rms wall-normal velocity fluctuation*

(d) *Rms spanwise velocity fluctuation*

Figure 2.8: Mean streamwise velocity and rms velocity fluctuations for $Re_\tau = 395$.

The results for the velocity and its fluctuations are presented in Fig. 2.8. It can be seen that both the low-dissipation formulation, as well as the VMS method with $c_2 = 8$, provide a quite accurate prediction for the mean streamwise velocity, with the former being slightly more accurate. By contrast, when the algorithmic constant is decreased in the VMS method ($c_2 = 2$), a much more dissipative behavior is obtained, which fails to accurately predict the mean flow. Nevertheless, it offers some improvement in the fluctuations in the wall-normal and spanwise directions. The low-dissipation formulation offers a significantly better prediction for the streamwise fluctuations than either VMS setup, while falling short in the other two directions. It is important to remind that the value of the Vreman constant has been chosen with focus on high Reynolds number flows (following the author's recommendation), and therefore at such low Reynolds numbers it tends to be more dissipative in the buffer zone. With this in mind, the turbulent channel case at a relatively high Reynolds number, namely $Re_\tau = 950$, is also examined.

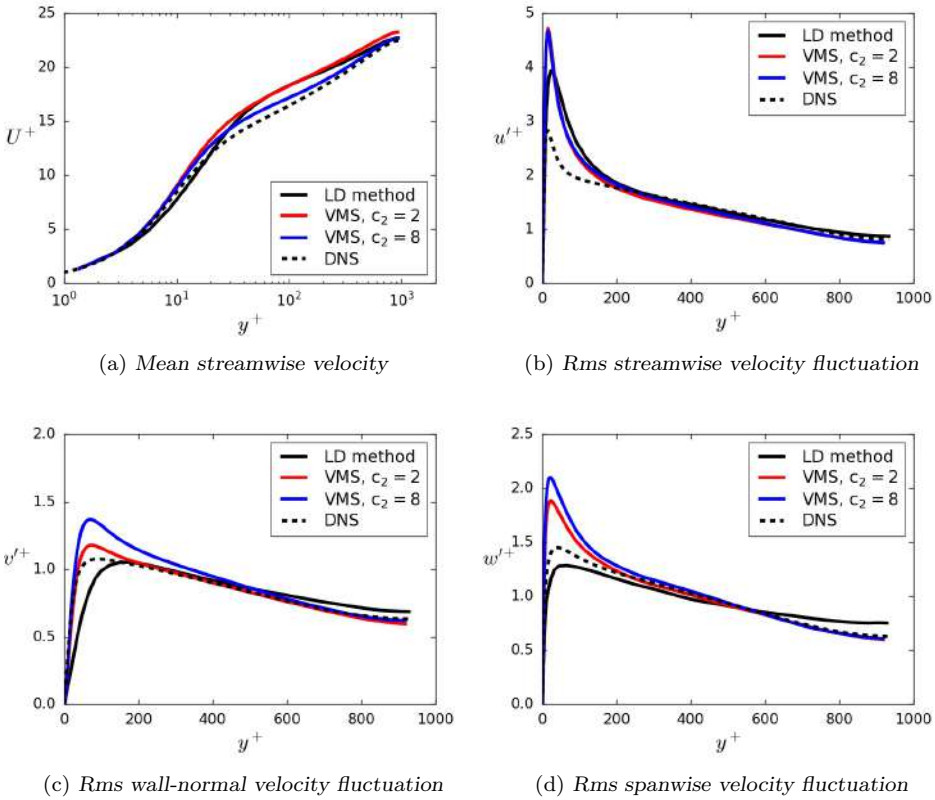

(a) *Mean streamwise velocity*

(b) *Rms streamwise velocity fluctuation*

(c) *Rms wall-normal velocity fluctuation*

(d) *Rms spanwise velocity fluctuation*

Figure 2.9: Grid G1: Mean streamwise velocity and rms velocity fluctuations for $Re_\tau = 950$.

2.4.4 Turbulent Channel Flow at $Re_\tau = 950$

For the $Re_\tau = 950$ case, the size of the computational domain has been increased to $6\delta \times 2\delta \times 3\delta$ to match the setup presented in [63]. The reference DNS is the one described in [64], which utilized a $3072 \times 385 \times 2304$ mesh on a $8\pi\delta \times 2\delta \times 3\pi\delta$ domain. Two different grids are considered: one consisting of $64 \times 97 \times 64$ elements (grid G1) and one of $128 \times 129 \times 128$ elements (grid G2), matching the resolutions used in [63]. The meshes use a uniform distribution in the tangential directions, while the hyperbolic tangent function of Eq. 2.59 has been used to concentrate the nodes towards the wall boundaries in the wall-normal direction. Here, the concentration factor is set to $\gamma = 2.5$. The first grid point off the wall is located at $y^+ = 1.4$ and $y^+ = 1$ for grids G1 and G2 respectively. At the center of the channel, much like the previous case, the elements are fairly isotropic with $\Delta x^+ = 89$, $\Delta y^+ = 49.6$ and $\Delta z^+ = 44.5$ for grid G1 and $\Delta x^+ = 44.5$, $\Delta y^+ = 37.3$ and $\Delta z^+ = 22.3$ for grid G2. As in the $Re_\tau = 395$ case, statistics were collected over

approximately 24 flow through units.

Fig. 2.9 shows the predictions for the velocity and its fluctuations for grid G1. All the formulations provide a fairly reasonable prediction for the mean streamwise velocity (Fig. 2.9a), with the VMS method with $c_2 = 8$ showing the best agreement with the DNS results. When the constant is set to $c_2 = 2$, the method overpredicts the velocity, which is consistent with the findings in Section 2.4.3. The low-dissipation formulation overpredicts the velocity in the region $30 < y^+ < 400$ with very good agreement with the DNS data in the rest of the channel.

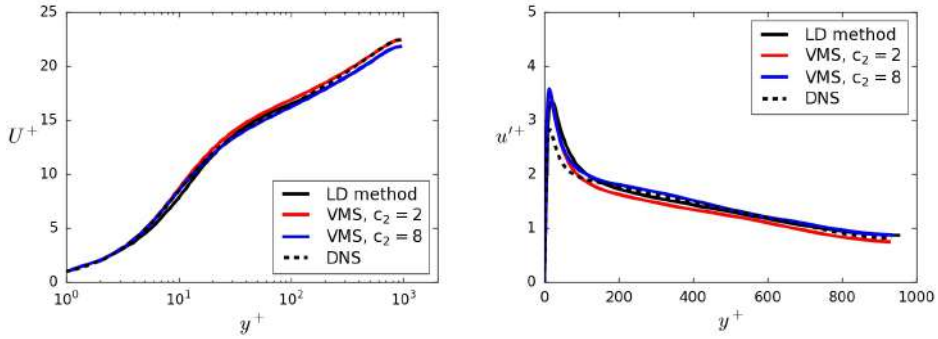

(a) *Mean streamwise velocity*

(b) *Rms streamwise velocity fluctuation*

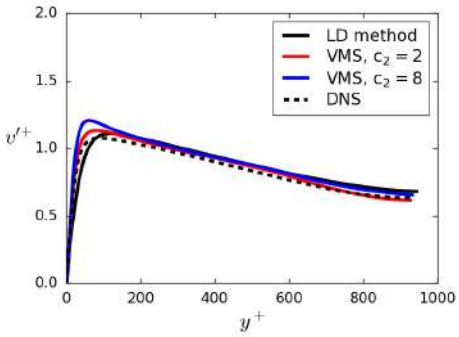

(c) *Rms wall-normal velocity fluctuation*

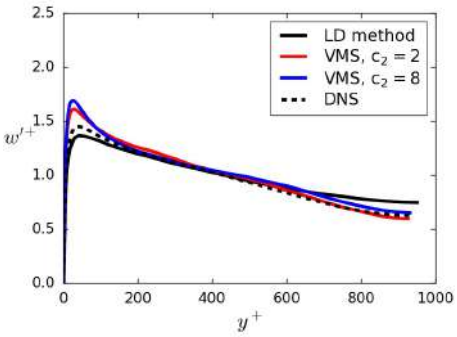

(d) *Rms spanwise velocity fluctuation*

Figure 2.10: Grid G2: Mean streamwise velocity and rms velocity fluctuations for $Re_\tau = 950$.

In terms of the prediction for the fluctuations (Fig. 2.9b-2.9d), it can be observed that the VMS method consistently overpredicts the fluctuations in the near-wall region, especially when $c_2 = 8$. While the prediction for the fluctuations improves when $c_2 = 2$, they are still overpredicted. The results are significantly better when the low-dissipation formulation is used. The overprediction of the near-wall streamwise fluctuations is notably smaller, while the wall-normal and spanwise fluctuations are slightly underpredicted

near the wall. This behavior is in good agreement with the results presented in [63] for the same mesh resolution.

The predictions for grid G2 are presented in Fig. 2.10. Much like the Taylor-Green Vortex case, it can be seen that all the methods converge towards the DNS data when the mesh is refined, in regards to the prediction of the mean streamwise velocity. Some deviation from the DNS can be observed in the fluctuations, however there is notable improvement compared to the results from grid G1. More specifically, the low-dissipation formulation offers better predictions for the fluctuations than either VMS setup, with the only exception being the spanwise fluctuations in the center of the channel.

2.4.5 Conclusions

Two numerical formulations for performing Large Eddy Simulations have been presented. The Variational Multiscale method (VMS), originally proposed by Hughes [11, 12], relies on performing a scale splitting operation and modelling the effect of the subscales as a means of stabilization. The numerical dissipation introduced by the stabilization is used to account for the effects of the subgrid scales in lieu of an explicit subgrid scale model. Therefore, the method can be categorized as an implicit LES method. A new low-dissipation formulation is also introduced. It uses a non-incremental fractional step method to stabilize the pressure and allow the use of equal order interpolation for velocity and pressure. The method uses an explicit subgrid scale model (in this work, the Vreman model [8] is used) for turbulence closure and can therefore be categorized as a classical LES method.

The two methods are compared in a set of benchmark cases, namely the Decaying Isotropic Turbulence (DIT), the Taylor-Green Vortex (TGV) and the Turbulent Channel Flow (TCF). Both formulations perform well in the cases examined, however an important issue is highlighted for the VMS method. Depending on the case and the Reynolds number examined, the best results are obtained for different values of the stabilization constants. This means that an ad hoc tuning of the constants is required to obtain the most accurate results. It is shown that using $c_2 = 2$ performs best in the DIT case, while $c_2 = 8$ performs best in the TGV and TCF cases. This behavior is also observed in a TCF at a higher Reynolds number ($Re_\tau = 2003$) presented in Chapter 4, where using $c_2 = 2$ proves to be more accurate. The findings presented here are consistent with the results from [42, 65]. It can be argued that this is a very undesirable behavior for a formulation that aims to be systematically used to predict complex flows, such as the ones encountered in industry. While this behavior is less prevalent when the meshes are refined, such resolutions are not representative of the grids typically used in engineering applications.

On the contrary, the new low-dissipation formulation has shown to offer very accurate predictions for all the cases examined without requiring any ad hoc tuning, even when coarser meshes are considered. Additionally, the new formulation results in a significant decrease in computational cost, needing approximately 60% less computational time per time-step, compared to VMS. This was partially counteracted by the ability to use higher time-steps in VMS in the examples considered in this section, however this is typically not possible in highly unsteady flows, where the size of the time-step is limited by the physics of the flow. The low-dissipation formulation is further tested in more complex cases in the next section with great results and is therefore recommended for use in the simulation of engineering applications.

2.5 Complex geometry problems using the low-dissipation formulation

2.5.1 Flow past a sphere

The fluid dynamics of the flow past a sphere at $Re = U_{\text{ref}}D/\nu = 10^4$ are considered. Here, the Reynolds number is defined in terms of the free-stream velocity U_{ref} and the sphere diameter D. At this Reynolds number, the flow separates laminarly from the sphere and transition to turbulence occurs in the separated shear layer, i.e. the flow is in the sub-critical regime [66]. In this regime, the main characteristics of the flow, i.e. drag coefficient, non-dimensional vortex shedding frequency, location of the separation of the boundary layer from the sphere, remain almost constant up until the flow enters the critical regime around $Re \approx 2.3 \times 10^5$ [67].

For the problem under study, a cylindrical computational domain of dimensions $x \equiv [-5.5D, 25.5D]$; $r \equiv [0, 10D]$; $\phi \equiv [0, 2\pi]$, with the sphere located at $(0, 0, 0)$, is considered. This domain has similar dimensions to that used in the DNS of Rodriguez et al. [68, 69]. Three different meshes have been considered and the flow has been integrated over 350 time-units to achieve well converged statistics. The meshes used are summarized in Table 2.1. The computational meshes are formed by three inner cylindrical regions of radius $1.5D$, whose outer boundary extends to $x/D = 3.5, 8.5, 20$ from the sphere center. The sizes of the elements at these zones are given in Table 2.1 and are denoted as Δ_{z1}, Δ_{z2} and Δ_{z3} respectively. The size of the outer/external zone Δ_{z4} is also given in the table.

Solutions obtained with the three different grids are compared to those of the DNS of Rodriguez et al. [69], which were obtained using a finite-volume approach on a computational grid of 18.2 million degrees-of-freedom.

In Table 2.2 the drag coefficient C_D, the base pressure coeffficient $-C_{pb}$, the separation angle θ_{sep} and the non-dimensional vortex shedding frequency $St = fU_{\text{ref}}/D$ are given for the three meshes considered. For meshes m2 and

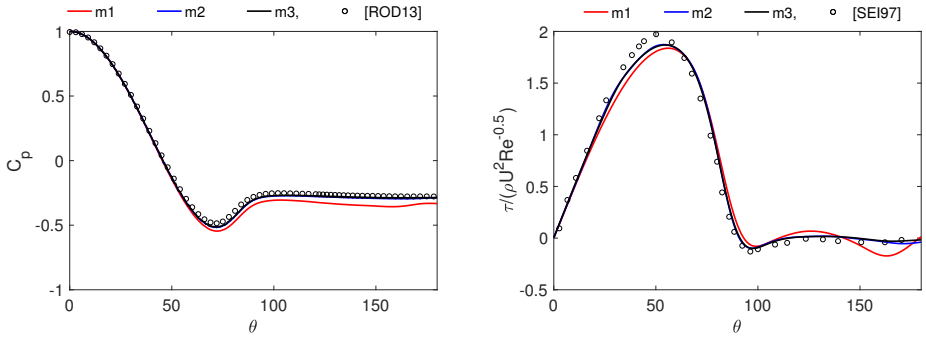

(a) (b)

Figure 2.11: Flow past a sphere. (a) Pressure coefficient and (b) skin friction distribution along the circumference of the sphere. Comparison with results from the literature [ROD13] Rodriguez et al. [69] and [SEI97] Seidl et al. [70].

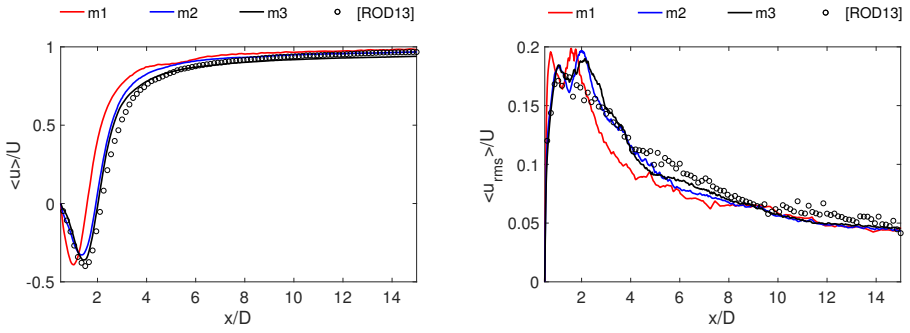

(a) (b)

Figure 2.12: Flow past a sphere. (a) Mean streamwise velocity in the wake centerline and (b) its fluctuation. Comparison with results from the literature [ROD13] Rodriguez et al. [69].

Mesh	N_{elem}	N_{dof}	Δ_{sph}	Δ_{z1}	Δ_{z2}	Δ_{z3}	Δ_{z4}
m1	3.19×10^6	7.1×10^5	0.05	0.08	0.13	0.195	1.09
m2	9.60×10^6	1.7×10^6	0.005	0.05	0.08	0.12	0.75
m3	3.27×10^7	5.6×10^6	0.0025	0.025	0.05	0.12	0.75

Table 2.1: Flow past a sphere. Meshes used in the simulation. N_{elem}: total number of elements, N_{dof}: number of degrees of freedom, Δ_{sph}: size of the elements on the surface of the sphere, Δ_{z1} to Δ_{z4}: size of the elements in the regions 1 to 4 in the wake of the sphere.

Mesh	C_D	$-C_{pb}$	θ_{sep}	St
m1	0.446	0.332	91.44	0.179
m2	0.408	0.287	89.8	0.213
m3	0.400	0.286	89.8	0.183
DNS	0.402	0.277	84.7	0.195

Table 2.2: Flow past a sphere. Flow parameters for Reynolds number $Re = 10^4$. Comparison with literature results. Drag coefficient C_D, base pressure coefficient $-C_{pb}$, separation angle θ_{sep}, non-dimensional vortex shedding frequency St. * DNS results by Rodriguez et al. [69].

m3 results are in good agreement the DNS data. Small differences are obtain in the vortex shedding frequency, which at these sub-critical Reynolds numbers is more difficult to measure as vortices are shed at different azimuthal locations at every vortex shedding cycle, as discussed in [68].

The pressure coefficient distribution ($C_p = (p - p_{\text{inf}}/0.5\rho U_{\text{ref}}^2$) together with the non-dimensional skin friction along the sphere circumference are plotted in Fig. 2.11. For the skin friction, results are compared to the DNS of Seidl at al. [70] at a lower Reynolds number of $Re = 5000$. To make comparisons possible, the results have been scaled with the Reynolds number. For the coarsest mesh, deviations from the reference data are large, especially in the aft part of the sphere. This is probably due to the quite coarse mesh used in the zone immediately after the sphere, which is altering the fluid dynamics in the recirculation zone producing a rather large and artificial mixing. However, for the second and third level of refinement results are quite close to the DNS data. The altered mixing in the recirculation zone obtained with mesh m1 can also be observed if the stream-wise velocity and its fluctuations are compared along the wake centerline (Fig. 2.12). For this mesh, the recirculation zone is shorter and closes near the sphere back stagnation point. However, with the two other levels of refinement, results

tend to the DNS data and the finest mesh accurately predicts the location and magnitude of the minimum velocity defect. Actually, these two meshes are capable of reproducing the level of streamwise fluctuations in the wake centerline quite well.

2.5.2 Flow around an Ahmed body

The Ahmed body is a generic reference car-type bluff body with a rounded front part and a slant back. Although it is a simplified geometry, it exhibits some of the main flow features encountered in real cars such as the large three-dimensional recirculation zone at the back of the geometry and complex vortex interaction of the flow coming from the slant side edges and the top and bottom surfaces. This generic car-like body was originally used in experimental measurements by Ahmed et al. [71] and later Lienhart et al. [72] performed laser Doppler anemometry (LDA) measurements of the velocity field and Reynolds stresses on the 25° and 35° slant back configurations. Because of its configuration, this simplified car model has also been used as a benchmark case in numerical investigations (see for instance [73, 74, 75, 76, 77, 78]).

Ahmed et al. [71] found that the slant angle largely influenced the flow configuration and the drag in the car. For the critical slant angle of 30°, they observed a complex vortex interaction with merging of vortices and the recirculation bubble, and that a further small change in the slant angle cause a dramatic change in flow configuration and in the body drag. The experimental study of Lienhart et al. [72] around this critical slant angle found that the counter-rotating vortices were responsible for keeping the flow attached to the slant for angles lower than the critical one. However, they observed that beyond the critical slant angle the flow detaches in the slant and forms a large recirculation region in the rear zone.

The chosen configuration corresponds to the geometry defined as in the experiments of Ahmed et al. [71]. The dimensions of the body are presented in Fig. 2.13. In this study, the slant angle $\phi = 25°$ is considered. The computational domain is a 3/4 rectangular open wind tunnel with dimensions $9.1944 \times 1.87 \times 1.4$m, as in the experiments of Lienhart et al. [72]. The inlet is located at 2.1024m upwind the front of the body. The downstream region has a length of 6.048m, measured from the rear end of the car. The Reynolds number in the experiments of Ahmed et al. [71], based on the inlet velocity U_{ref} and the car height H, was $Re_H = U_{\text{ref}} H/\nu = 1.2 \times 10^6$, whereas in the LDA measurements of Lienhart et al. [72] it was $Re_H = 7.68 \times 10^5$. In the present computations, wall-resolved LES have been conducted and thus, in order to have a good resolution within the boundary layer, the Reynolds number of the experiments has been reduced to $Re_H = 2 \times 10^5$ as in the LES study of Krajnović & Davidson [74]. As it was argued by Krajnović

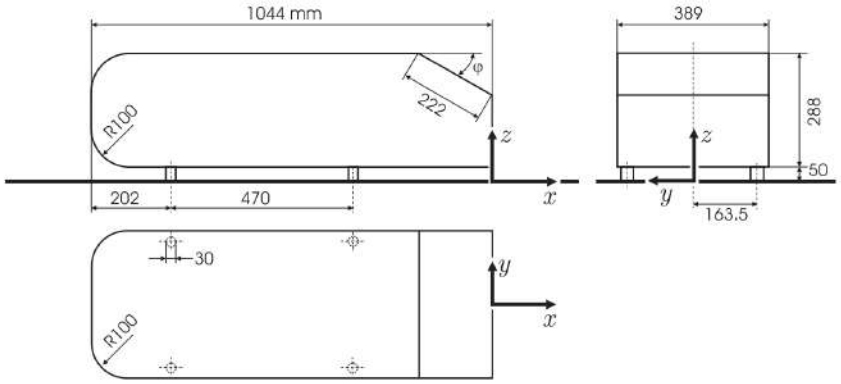

Figure 2.13: Ahmed body dimensions.

Mesh	N_{elem}	N_{dof}
m1	9.48×10^6	3.62×10^6
m2	14.9×10^6	5.64×10^6
m3	25.6×10^6	9.52×10^6

Table 2.3: Ahmed body. Meshes used in the simulations. N_{elem}: total number of elements, N_{dof}: number of degrees of freedom.

& Davidson, given the geometry of the body, the transition to turbulence is triggered by the sharp corners and thus, this Reynolds number reduction shall not affect the results after separation.

In order to perform the computations, large-eddy simulations with a uniform velocity $(u, v, w) = (U_{\text{ref}}, 0, 0)$ at the inflow have been used. As the domain is a 3/4 open wind tunnel, at the lateral and top walls slip boundary conditions are prescribed. As for the outflow of the domain, a pressure-based boundary condition is applied. No-slip conditions at the body and bottom surface are prescribed. Three different levels of refinements are considered here (see Table 2.3). To design the computational grids, a prism layer around the car geometry has been constructed to capture the boundary layer and allow a good resolution in this zone. The size of the elements in this layer follows the values reported by Krajnović & Davidson [74]. Moreover, more nodes are clustered in the zone of the slant in order to properly resolve the separation of the boundary layer in the rear end of the car. The finest computational mesh used (m3) can be seen in Fig. 2.14.

Fig. 2.15 shows the complex vortex interaction in the slant and rear end of the car. Vortices are identified by means of Q-isosurfaces [61] and coloured by the velocity magnitude. As can be seen, the simulations are capable of

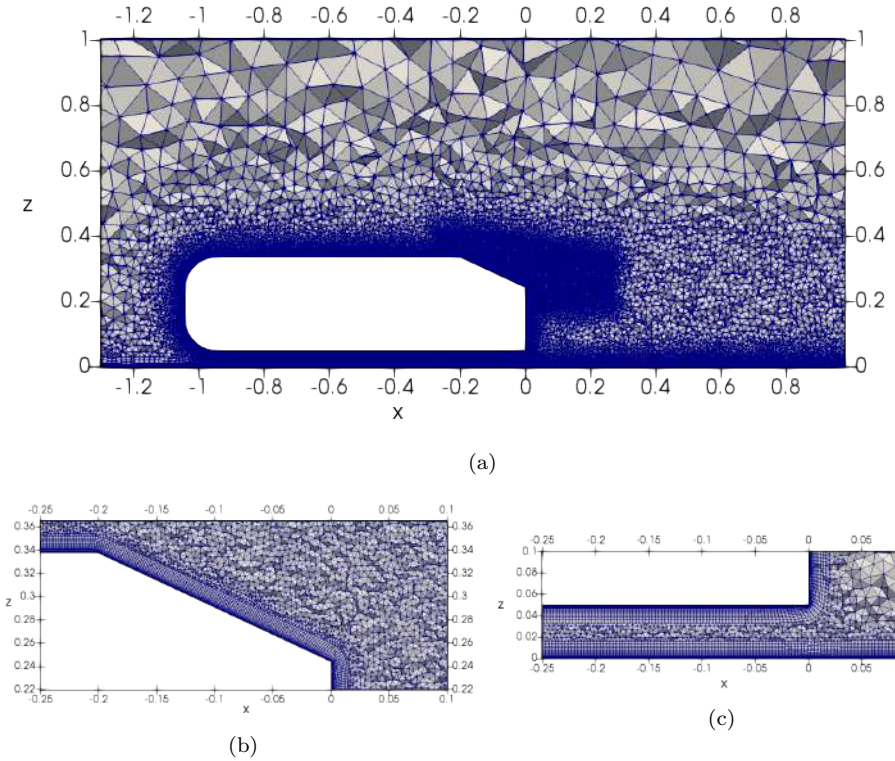

Figure 2.14: Ahmed body computational mesh (m3). (a) Mesh around the car, (b) detail of the mesh on the slant, (c) detail of the mesh close to the ground.

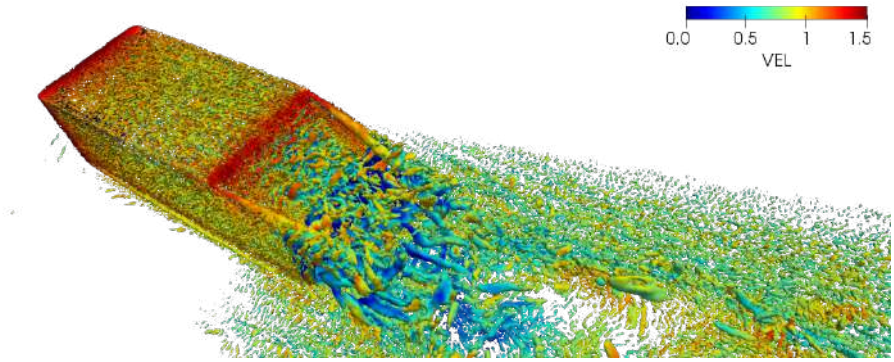

Figure 2.15: Ahmed car body. Vortical flow structures identified by Q-isosurfaces $Q = 150$ coloured by the velocity magnitude.

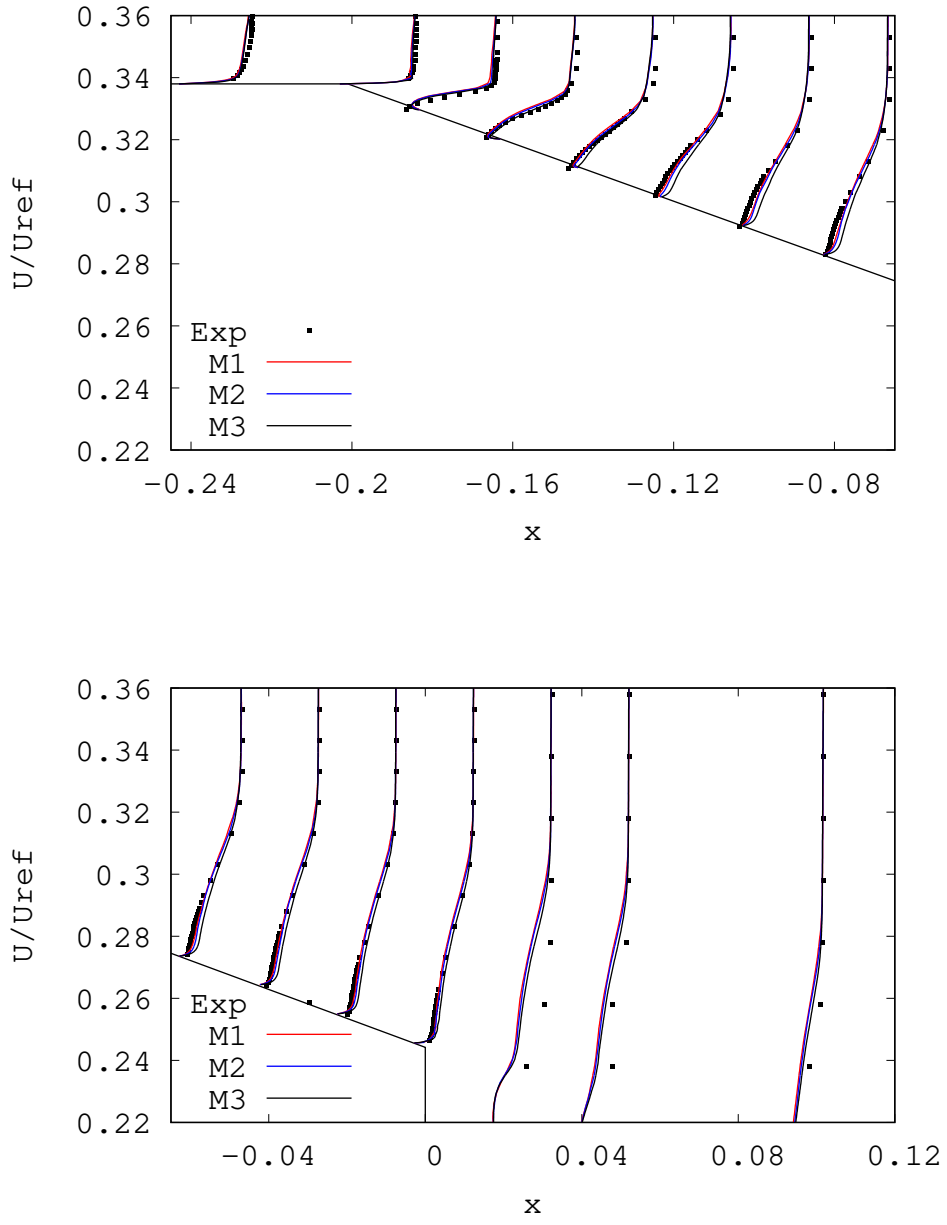

Figure 2.16: Ahmed car body. Mean streamwise velocity in the symmetry plane $z = 0$ over the slant. Comparison with the experimental results of Lienhart et al. [72].

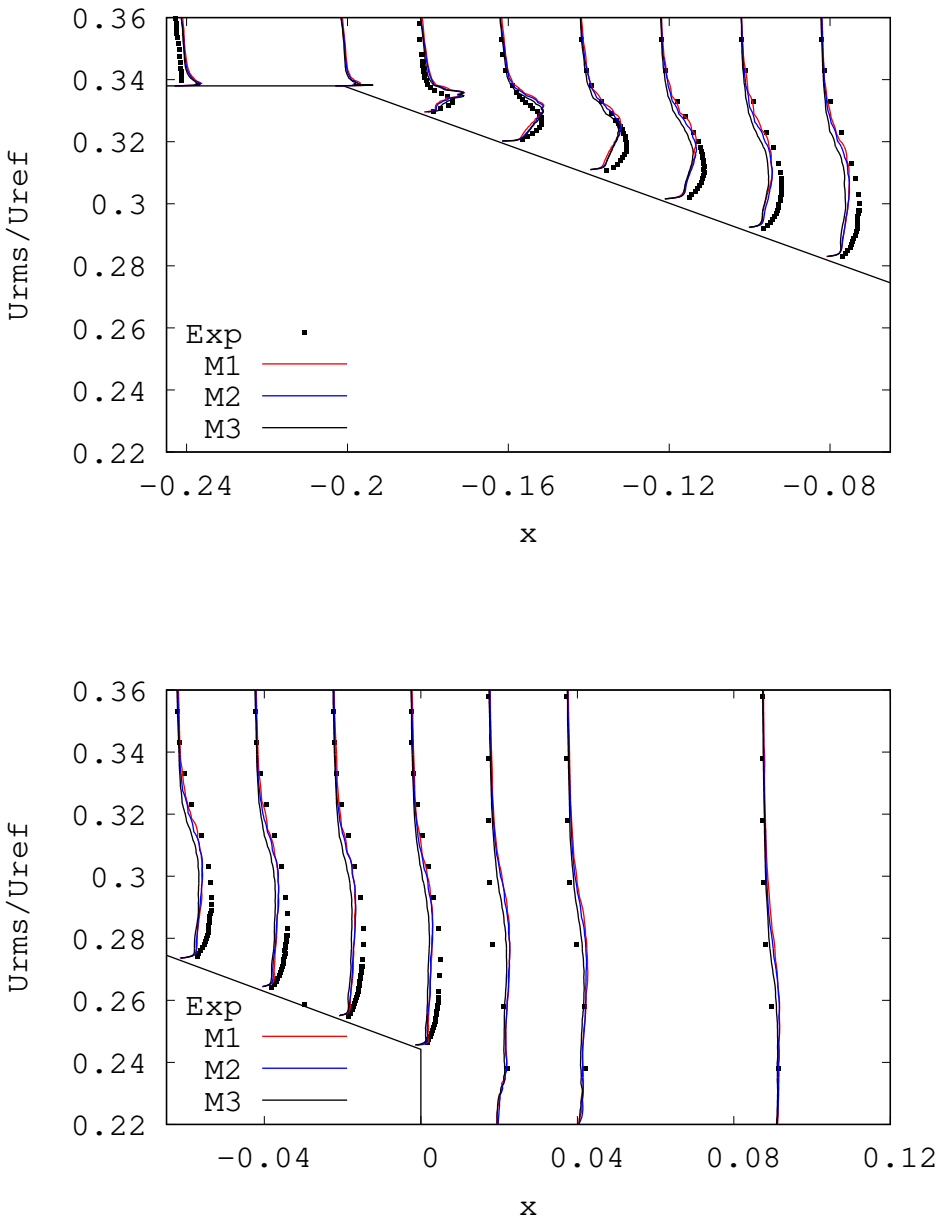

Figure 2.17: Ahmed car body. Streamwise velocity fluctuations in the symmetry plane $z = 0$ over the slant. Comparison with the experimental results of Lienhart et al. [72].

Mesh	C_D	$C_{D,p}$	C_L	$C_{D,\text{rms}}$	$C_{L,\text{rms}}$
m1	0.292	0.261	0.267	5.1×10^{-3}	2.09×10^{-2}
m2	0.296	0.262	0.272	5.7×10^{-3}	2.57×10^{-2}
m3	0.297	0.260	0.275	6.2×10^{-3}	2.82×10^{-2}
Ahmed (exp)*	0.285	0.234	-	-	-
K&D (LES)†	-	0.294	0.334	5.0×10^{-3}	1.80×10^{-2}
ALJ (LES)‡	0.302	0.292	0.282	8.0×10^{-3}	3.30×10^{-2}

Table 2.4: Ahmed body. Aerodynamic forces on the surface and comparison with the literature. Drag coefficient C_D, form drag coefficient $C_{D,p}$, lift coefficient C_L, rms of the drag and lift coefficients $C_{D,\text{rms}}$ and $C_{L,\text{rms}}$ respectively. * experimental results by Ahmed et al. [71], † LES results by Krajnovic & Davidson [74], ‡ LES results by Aljure [78].

capturing the two counter-rotating vortices that separate from the slant top corners and interact with the flow coming down from the center of the slant. In Table 2.4, the aerodynamic forces on the surface of the car are given for the three computational meshes and compared to the experiments of Ahmed et al. [71]. and to the LES computations by Krajnovic & Davidson [74] and Aljure et al. [78]. In general, present LES results reproduce both the form and total drag from the experiments quite well, even with the coarsest grid, which is the result of the good resolution achieved in the near-wall region.

Fig. 2.16-2.17 show computed profiles of the mean streamwise velocity and its fluctuations in the symmetry plane over the slant at different streamwise stations. Results are compared to the experimental data of Lienhart et al. [72]. Good level of agreement is observed at all levels of refinement.

Chapter 3

Inflow boundary conditions

3.1 Introduction

In contrast with RANS, where only the mean flow is directly calculated (i.e. not modelled) and thus only a mean inflow profile is required as boundary condition, in LES and DNS the specification of the inflow boundary conditions is more complex. In early applications of LES, this problem did not appear, as the flows could usually be considered periodic in the flow direction. For spatially developing flows, however, such as those encountered in real world applications, the inflow conditions need to possess specific characteristics connected with the properties of LES. When the inflow is expected to be laminar and transition occurs later in the computational domain, the problem becomes nearly insignificant as the production of turbulence is mostly performed inside the domain. For flows with a fully turbulent inflow, on the other hand, specifying inappropriate boundary conditions can significantly alter the numerical predictions.

Ideally, the inflow velocity needs to accurately represent the contribution of the eddies. This, in effect, means that the imposed velocity vector needs to match the moments, spectra and phase of the above eddies. While the first two could, in theory, be approximated by the use of stochastic methods, the same is not possible for phase information, as it is flow-dependent (related to the structure of the eddies). The absence or inaccuracy of this information results in the need of a transition zone, until realistic, for the particular type of flow, turbulence is achieved. In an effort to reduce the cost of LES and DNS, the inlet should be as close to the region of interest as possible. Thus, the approximate conditions introduced need to be as accurate as possible, so this transition zone is minimized.

Different approaches have been proposed for the specification of appropriate inflow boundary conditions. They can be categorized as follows:

- **Recycling/Mapping**
  In the recycling technique, originally proposed by Spalart [79], profiles

of variables are extracted from a predefined downstream location and reintroduced as inflow boundary conditions, after being rescaled to match the characteristics of the desired inflow profiles.

– **Precursor/concurrent simulation**
An alternative method is to use time-accurate inflow profiles from an auxiliary simulation, usually called precursor/concurrent simulation. This can be achieved either by simultaneously running the two simulations and feeding the profiles from the auxiliary (concurrent) simulation to the main simulation [80, 81], or by initially running a (precursor) simulation and storing the generated inflow data, for later use in the main simulation.

– **Synthetic turbulence**
These techniques synthesize inflow conditions by superposing some sort of stochastic, unsteady disturbances on a mean flow profile. This method was originally proposed by Kraichnan [82]. These perturbations are usually based on analytic representations or Fourier series and they need to possess some specific flow characteristics, such as low order statistics (mean velocity, turbulent kinetic energy, Reynolds stresses etc).

Extensive reviews on the various techniques for generating turbulent inflow conditions can be found in [83, 84, 85, 86, 87]. In this work the generation of inflow conditions through a precursor simulation as well as synthetic turbulence techniques will be examined.

3.1.1 Precursor simulation

As explained previously, a precursor simulation refers to an auxiliary simulation that is performed before the main simulation, using the same geometry and operating conditions. Typically the precursor mesh is created through an extrusion of the inlet surface mesh of the main simulation. Inlet slices are extracted and stored in order to be used later. Another possibility is to run a concurrent simulation, where the auxiliary simulation runs in parallel with the main simulation and the extracted slices are directly fed into the main simulation through some form of communication (commonly called coupling). This type of auxiliary simulations will not be explored here.

If a fully developed mean flow is needed at the inflow, the precursor simulation can be run with periodic conditions in the streamwise direction. The flows considered here fall under this category. Nevertheless, spatially developing flows can also be run on a precursor simulation.

Considering the high storage demands and computational cost of performing a full precursor simulation, i.e. producing a set of inflow data that

suffices for the full duration of the main simulation, a more common approach is to only run the precursor simulation for a limited amount of time (after the statistically steady state has been reached), which results to a limited set of inflow data being stored. This set of data is fed into the main simulation, and when all the slices have been used, the same set is reused. Two approaches are used here to perform this procedure: a) no periodicity is imposed on the set of data, i.e. there is a discontinuity between the last and first slice of inflow data, and b) the set of inflow data is modified to become periodic through a simple blending function. Here, the blending function suggested in [88]:

$$u_{\text{per}}(i) = \frac{1}{2}\left[u_1(i)\left(1 - cos\left(\frac{i}{N_{\text{per}}}\pi\right)\right) + u_2(i)\left(1 + cos\left(\frac{i}{N_{\text{per}}}\pi\right)\right)\right] \tag{3.1}$$

is used, where i is the current time-step and N_{per} is the total amount of time-steps used for the blending. Fig. 3.1 illustrates the procedure with the original, discontinuous signal presented in Fig. 3.1a and the modified, periodic signal in Fig. 3.1b. Reusing the same set of data can introduce an artificial low-frequency behavior [85], however Li et al. [89] suggested that the nonlinearity of the flow downstream of the inlet destroys such periodicity. Both approaches are examined on the flow over a three-dimensional hill (Section 3.3).

3.1.2 Synthetic turbulence

The simplest approach to synthesizing turbulence would be by superimposing random white noise on a mean flow profile. Such an inflow condition, however, lacks any spatial and temporal correlation, two very important characteristics of turbulence. This approach was followed by Lund et al. [90], where a target Reynolds stress profile was assigned to white noise. As a result of the lack of coherence between the eddies, they found that a very large transition zone (of the order of 50 boundary layer thicknesses) was needed for correct structures to be generated.

Kraichnan [82] proposed a method of generating isotropic fluctuations, based on a sum of Fourier modes. An energy spectrum is prescribed, so that the amplitude of the fluctuations is defined as a function of the wave number. In order to satisfy the requirement that the velocity profile possesses certain statistical properties (mean/fluctuating values and energy spectra), Lee et al. [91] suggested an inverse Fourier transform of the velocity field. In their method, a three-dimensional box containing the generated fluctuations is convected across the inlet plane, which transforms their streamwise correlation to a temporal one. Le et al. [92] attempted a modification of this method, where the fluctuations were rescaled in order to match a prescribed Reynolds stress tensor at the inlet and used it in the backward-facing

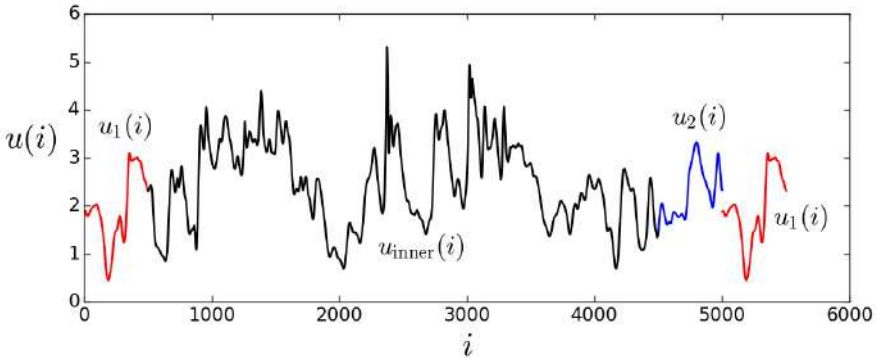

(a)

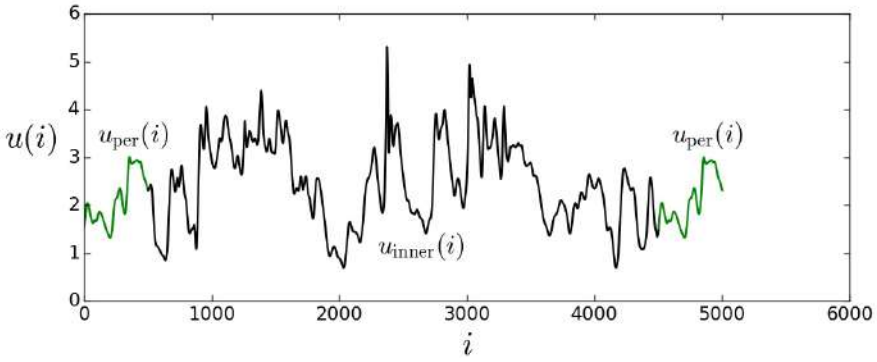

(b)

Figure 3.1: Inflow signal using a precursor simulation: (a) discontinuous signal, (b) periodic signal.

step case. Even though they faced several problems, such as that the non-homogeneity of the inlet plane significantly increases the cost of the inverse Fourier transform, they noted that a transition zone of only 12 boundary layer thicknesses was needed, i.e. a great reduction compared to the random method [90].

Based on Kraichnan's proposal [82] and the method of Le et al. [92], Smirnov et al. [93] suggested a method that accounts for the anisotropy of the flow. In their method, a Fourier decomposition with Fourier coefficients computed from different spectra at different locations across the flow, based on local turbulent time and length scales, was used. Batten et al. [94] proposed the use of a superposition of sinusoidal modes with random frequencies and wave numbers, but given moments and spectra. This approach effectively allows for the more elongated eddies in the direction of larger Reynolds stresses to be represented, thus producing more realistic, anisotropic turbulence. Klein et al. [95] approached the problem in the physical space, with the use of a digital filtering procedure that remedies the

lack of large-scale dominance in the data generated by the random method. They assumed a Gaussian shape for the filter, depending on the length scale as a parameter. Kempf et al. [96] extended that work, by creating a method that generated fluctuations in the physical space using a diffusion process. Their method was shown to work in arbitrary geometries and unstructured grids. Davidson [97], introduced a "mixed" method, combining the Fourier decomposition with digital filtering. With a procedure similar to the one proposed by Kraichnan [82], isotropic fluctuations are synthesized and then filtered in time using an asymmetric time filter, in order to acquire temporal correlation.

More recently, Jarrin et al. [98, 99], inspired by the work of Batten et al. [94], proposed a different approach, based on a Lagrangian treatment of vortices. In their method, known as synthetic-eddy method (SEM), the fluctuations are imposed by eddies convected through a virtual box. These eddies are convected through the box by the locally imposed mean velocity. Upon their exit of the box, they are regenerated at a random location of the inlet plane. These coherent structures generated in the inlet plane are defined by a shape function that provides information on the structure's spatial and temporal characteristics. This method is shown to be able to reproduce first and second order one point statistics, characteristic time and length scales, as well as the shape of coherent turbulent structures. Pamiès et al. [100] extended this idea by defining the shape function in more detail. By splitting the near-wall region in multiple zones, they were able to adjust the structures based on previous observations of vorticity in the turbulent boundary layer. While this approach provides better results, it is an ad hoc approach, as it implies specifically designing the structures for each problem. Another problem identified in those methods is that the produced velocity field is not divergence-free. To that end, Poletto et al. [101] constructed a divergence free synthetic eddy method (DFSEM). They approached the problem by applying the original methodology to the vorticity field and then switching back to the velocity field by taking its curl, thus complying with the divergence free condition.

3.2 Synthetic inflow through diffusion

In this work, the synthetic inflow technique proposed by Kempf et al. [96] is considered, since it is based on creating a turbulent signal from white noise through the diffusion process, making it easy to apply and implement in a CFD code. This diffusion process eliminates the unphysical small-scale structures of the random field, resulting in dominant large-scale structures. Additionally, since it is a method based on physical space, it does not need equidistant grid spacing, but can instead be applied to arbitrary grids. This is a very desirable method when performing large-eddy simulations of com-

plex flows, since the grids utilized are not isotropic. The method is described in detail in the following:

Initially, the inlet surface mesh is extruded in order to create the auxiliary grid that will be utilized for the diffusion process. In our implementation, the z-axis serves as the temporal dimension (following Taylor's hypothesis), therefore the surface mesh is rotated, if necessary, before being extruded in that direction. Taylor's hypothesis relates temporal to spatial fluctuations, reasoning that if the turbulence intensity of the flow is small, the temporal variation of the velocity at a fixed point can be seen as the result of the convection of unchanging spatial patterns. The length of the extrusion typically depends on the target integral time scale T, while the spacing in the z-direction is related to the time interval between the consecutive slices of the generated inflow set. No-penetration boundary conditions are imposed on the boundaries that correspond to the wall and slip boundaries of the main simulation, while periodic conditions are imposed to match those of the main simulation. Periodicity is also imposed in the z-direction.

An initial condition for the auxiliary simulation is generated by means of a three-dimensional white noise field U_i that is normalized in order to fulfill the following conditions:

$$\begin{aligned} \overline{U}_i &= 0 \\ \overline{U_i U_i} &= 1 \end{aligned} \tag{3.2}$$

It is subsequently normalized with the square root of the lumped mass matrix, which represents the volume of the mesh assigned to each node:

$$U_i := M_i^{-\frac{1}{2}} U_i \tag{3.3}$$

to account for the anisotropy of the typical computational grid. The auxiliary simulation involves solving the diffusion equation:

$$\frac{\partial U_i}{\partial t} = D \frac{\partial^2 U_i}{\partial x_j^2} \tag{3.4}$$

for a time interval equal to $t = T$, where D is the diffusion coefficient, linked to the desired integral scales through the following expression:

$$D = \frac{L^2}{2\pi T} \approx \frac{L}{2\pi} \tag{3.5}$$

where L denotes the target integral length scale. The last approximation stems from considering $L \approx T$, which is the case in the numerical experiments presented in this work. This diffusion process is shown to produce a Gaussian-shaped autocorrelation function, since it is essentially equivalent to convoluting the original signal with a Gauss filter [96].

The resulting field U_i is then renormalized to fulfill conditions 3.2. Finally, the velocity field is scaled in order to match the desired mean velocity $\overline{\mathbf{u}}$ and Reynolds stress tensor R_{ij} profiles at the inlet. If the goal

is to only satisfy the trace elements, the velocity can be constructed using $u_i = \overline{u}_i + \sqrt{R_{ii}}U_i$. This is the procedure followed in the cases presented in this work. Nevertheless, the cross-correlations between the velocity components can also be taken into account by using Lund's method [90], where $u_i = \overline{u}_i + \alpha_{ij}U_j$ with:

$$\alpha_{ij} = \begin{bmatrix} R_{11}^{0.5} & 0 & 0 \\ R_{21}/\alpha_{11} & \left(R_{22} - \alpha_{21}^2\right)^{0.5} & 0 \\ R_{31}/\alpha_{11} & \left(R_{32} - \alpha_{21}\alpha_{31}\right)/\alpha_{22} & \left(R_{33} - \alpha_{31}^2 - \alpha_{32}^2\right)^{0.5} \end{bmatrix} \tag{3.6}$$

Slices of this pseudo-turbulent velocity field $\mathbf{u}$ can be extracted and applied as inflow data in the LES, making use of Taylor's hypothesis, that relates temporal to spatial fluctuations.

It can be seen that the method is simple to use and implement in a CFD code. It essentially consists of three major steps:

- Generate the grid and appropriate initial conditions for the auxiliary simulation
- Perform the auxiliary simulation, which solves the diffusion equation
- Scale the resulting velocity field in order to satisfy the desired mean velocity and fluctuation profiles

The method only needs the target integral scales (L, T) and the desired velocity profiles as an input, all of which can typically be approximated using data from simpler simulations found in the literature.

3.3 Flow over a three-dimensional hill

The two precursor techniques (discontinuous and periodic), presented in Section 3.1.1, as well as the synthetic method by Kempf et al. [96], presented in Section 3.2 are evaluated in the simulation of a flow over a three-dimensional circular hill, based on the experimental configuration presented by Ishihara et al. [102]. The hill has a cosine-squared cross-section with a maximum-slope of approximately 32°. The shape of the hill is described by the following expression:

$$z(x, y) = H \cos^2\left(\frac{\pi\sqrt{x^2 + y^2}}{2R}\right)$$

where $H = 4$ cm and $R = 10$ cm denote the height of the hill and the radius of its base respectively. The hill along with the basic dimensions and the coordinate system orientation are presented in Fig. 3.2.

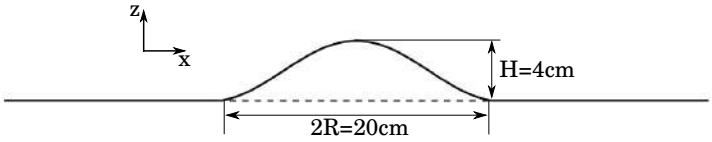

Figure 3.2: Three-dimensional hill geometry and dimensions.

This case is of particular interest, since most of the experimental studies focus on two-dimensional geometries. The three-dimensionality of this geometry allows for comparisons with experimental data along the horizontal plane as well, and not just the vertical profiles. Additionally, using laminar inflow conditions results in a significant underprediction of the velocity fluctuations, highlighting the importance of using appropriate inflow conditions. Therefore, this case allows for a thorough comparison between the various turbulent inflow generation techniques described in the previous sections.

Without the hill the flow corresponds to a neutrally stratified atmospheric boundary layer. The Reynolds number of the flow is $Re_H = 15200$ based on height of the hill $H = 4$ cm and the free-stream velocity $U_{\text{inf}} = 5.36$ ms^{-1} at the top boundary. The flow is simulated in a computational domain of 128 cm $\times$ 64 cm $\times$ 32 cm in the streamwise (x), spanwise (y) and wall-normal (z) directions respectively, with the hill located in the middle of the domain. Periodic boundary conditions are used in the spanwise direction with a slip boundary condition at the upper boundary. While those conditions do not directly correspond to the conditions used in the experiment, there is a large distance between the hill and the boundaries and, thus, the conditions have minimal impact on the flow in the vicinity of the hill.

An unstructured mesh of 2.6 million nodes is used, with a resolution of $\Delta x = \Delta y = 0.25$ cm and $\Delta z = 0.125$ cm at the region of the hill. This resolution results in $z^+ \approx 18$, which means that wall modelling is required. The exchange location method described in Section 4.2 is used, with the matching interface located at the third grid point off the wall. A simple logarithmic law for rough walls (cf. Eq. 4.6) is employed to calculate the wall stress, repeated here for ease of reading:

$$u_z = \frac{u_*}{\kappa} ln \left(\frac{z + z_0}{z_0} \right)$$

where $\kappa = 0.41$ is the von-Kárman constant, u_* is the friction velocity and z_0 is the roughness length. The test-section floor of the experiment was estimated to have $z_0 = 0.001$ cm, however the hill model was machined from

wood, and, therefore, its roughness length is set to $z_0 = 0.002$ cm, following the setup used in [103]. Statistics are collected for 8 seconds after the statistically steady state is achieved. All the results have been normalized using the velocity at hill height in the undisturbed boundary layer, here $U_h = 4.3$ ms^{-1}.

Three different approaches are evaluated in regards to generating turbulent inflow conditions. A precursor simulation was performed with periodicity in the streamwise direction. The flow was driven by a constant pressure gradient, set to an appropriate value that guaranteed a logarithmic velocity profile described by the aforementioned wall law, with $u_* = 0.212$ ms^{-1} and $z_0 = 0.001$ cm. The mesh used for the precursor simulation consisted of approximately 1.8 million nodes, highlighting the significant overhead of the method. Slices of inflow data were extracted for 20000 time-steps (corresponding to a total time of 1 second). However only every fourth slice was used, in order to reduce the memory and storage demands, with a linear interpolation used inbetween. This procedure was found to have minimal impact on the results. Two inflow sets were created from this database, one discontinuous and one periodic following the technique described in Section 3.1.1, with $N_{\text{per}} = 500$, corresponding to $t_{\text{per}} = 0.1$s. In addition, synthetic inflow conditions were generated using the diffusion process by Kempf et al. [96] (cf. Section 3.2). The target length scale was approximated as $L = 0.25H$, based on the hill geometry and mesh element size. A simple logarithmic profile was imposed on the generated turbulent field, along with Reynolds stress profiles from an Atmospheric Boundary Layer simulation. The time-interval between slices is $\Delta \text{t}_{\text{inlet}} = 2.5 \times 10^{-4}$s, which is approximately five times larger than the time-step used in the main simulation.

The vertical profiles of the streamwise and wall-normal velocity components at seven different stations on the central plane of the hill are presented in Fig. 3.3. It can be seen that all methods, including the laminar inlet, provide very good agreement with the experimental data. It is important to note the minimal difference between the two precursor inlets. This behavior is evident in all the results presented here. The features of the flow are properly captured, with the flow accelerating on the upwind slope of the hill and separating shortly after the crest, before reattaching later downstream of the hill. The separation is also evident when looking at the vertical velocity (Fig. 3.3b), since positive values are obtained on the downwind slope. A clear representation of the recirculation region can be seen in Fig. 3.4, which presents a contour of the mean streamwise velocity in the vicinity of the hill for the synthetic inlet case.

Figure 3.5 shows the spanwise distribution of the tangential components of the velocity behind the hill ($x/h = 3.75$) at two different heights: (a) $z/h = 0.125$ and (b) $z/h = 1$. The former corresponds to the height where the streamwise and vertical fluctuations reach their maximum value, while the latter is at the height where the maximum of the spanwise fluctuations

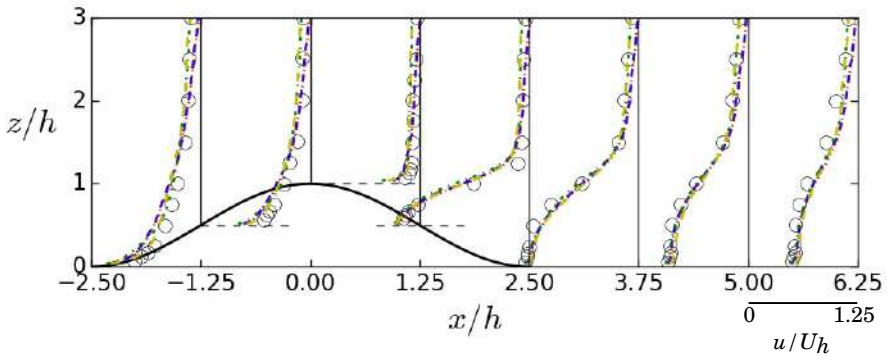

(a)

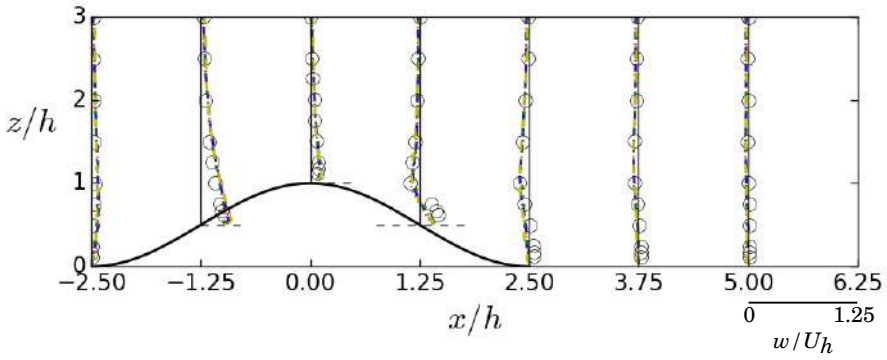

(b)

Figure 3.3: Three-dimensional hill. Vertical profiles of the mean (a) streamwise and (b) vertical velocity on the central plane of the hill. Blue dashed lines (- - - -): periodic precursor, red dotted lines (·····): discontinuous precursor, yellow loosely dashed lines (- - - -): synthetic inlet, green dot-dashed lines (-·-·-): laminar inlet, circles (○): experiment (Ishihara et al [102]).

is observed. It can be seen that the laminar inlet underpredicts the velocity near the wall, however the correct values are recovered further away from the wall. All the turbulent inflow methods provide accurate predictions, with the results from the synthetic method being in better qualitative agreement with the experimental data.

The vertical profiles of the three components of the normal stress on the central plane of the hill can be seen in Fig. 3.6. It becomes immediately obvious that the laminar inlet completely falters, providing a severe underprediction of the fluctuations in all directions as we move further away from the wall, with the only exception being inside the recirculation zone, where the turbulence is generated by the geometry itself and seems largely insensitive to the prescribed inlet. The results from all the turbulent inflow methods are in good qualitative agreement with the experimental data. All

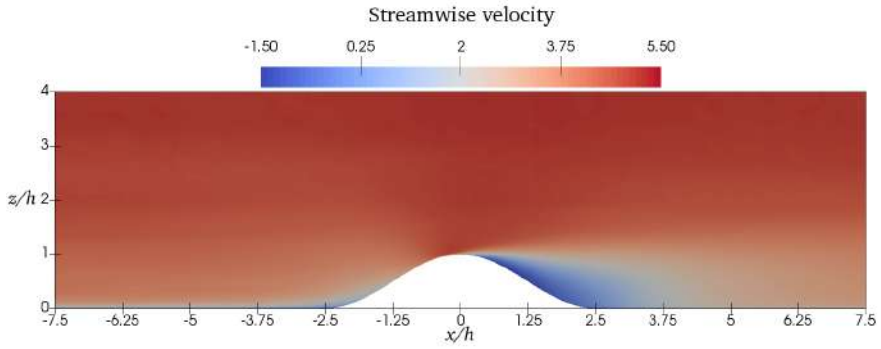

Figure 3.4: Contour of the mean streamwise velocity on the central plane of the hill for the synthetic inlet method.

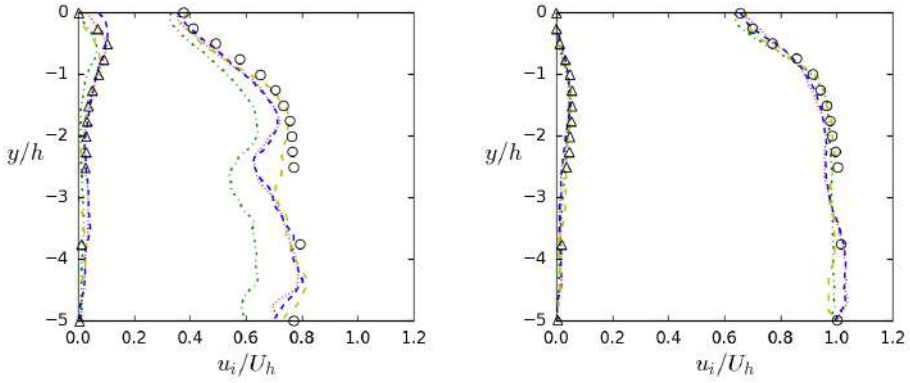

(a) (b)

Figure 3.5: Three-dimensional hill. Spanwise distributions of the streamwise and spanwise velocity behind the hill at (a) $x/h = 3.75$, $z/h = 0.125$ and (b) $x/h = 3.75$, $z/h = 1$. Blue dashed lines (- - - -): periodic precursor, red dotted lines (·····): discontinuous precursor, yellow loosely dashed lines (- - - -): synthetic inlet, green dot-dashed lines (-·-·-): laminar inlet, circles (○): streamwise velocity, triangles (Δ): spanwise velocity, experiment (Ishihara et al [102]).

the methods overpredict the fluctuations immediately downstream of the recirculation region at hill height, especially in the spanwise direction. A small underprediction of the fluctuations can also be observed further away from the wall. All the methods provide nearly identical results, with the synthetic method being slightly less accurate in the near-wall region of the upwind slope of the hill.

Fig. 3.7 presents the spanwise distribution of the normal stress components at the two different heights mentioned previously. The laminar inlet

method offers somewhat reasonable results in the near-wall region, which is consistent with the observations from Fig. 3.6. However, it heavily underpredicts the fluctuations away from the wall, especially in the regions further away from the hill. A slight overprediction of the fluctuations from all the methods can be observed at $z/h = 0.125$, with the synthetic method having the biggest deviation from the experimental data. This issue is rectified as we move further away from the wall, with both the precursor and the synthetic methods offering very accurate results. This is especially obvious in the streamwise direction, where the predictions are in excellent agreement with the experiments. It is important to note that the "fluctuating" behavior observed in the spanwise distribution of the stress components is consistent with the LES studies found in the literature [104, 103].

Figures 3.8 and 3.9 show the streamwise vorticity upstream of the hill at heights $z/h = 0.125$ and $z/h = 1$ respectively. It can be seen that on both locations, the synthetic inlet needs a distance less than $5H$ at either height, to recover the correct level of turbulence, even though the chosen length scale was evidently much bigger than the actual one. Of course, an inlet with the correct length scale could be generated, but that would be counter-intuitive, since such values are unknown in a realistic scenario and are, thus, approximated. As expected, the precursor simulation retains the same (and presumed correct) level of turbulence throughout the domain. On the other hand, the laminar inlet struggles to develop the appropriate turbulence. In the near-wall region, it reaches the correct behavior after approximately $9H$, which explains why this method is able to provide reasonable predictions for the fluctuations near the wall. However, further away from the wall, the method completely falters, resulting in a significant underprediction of the fluctuations (Fig. 3.6). Nevertheless, it needs to be noted that there is an increase in the vorticity, showing that a laminar inlet should eventually recover the appropriate turbulent behavior, given a large enough distance upstream of the region of interest. This is not computationally feasible in most engineering applications, however, further showcasing the need for turbulent inflow generation techniques.

3.4 Conclusions

In this chapter, the importance of utilizing appropriate inflow conditions in turbulent flows has been examined. Two different methods of prescribing a turbulent inflow are explored, one stemming from a precursor simulation and one using a synthetic technique. For the precursor simulation method, the effect of introducing periodicity on the set of inflow data is investigated, however the results are nearly identical with those of the discontinuous inflow set. An extensive literature review of the various synthetic methods is presented, and the method of Kempf et al. [96], where the inflow conditions

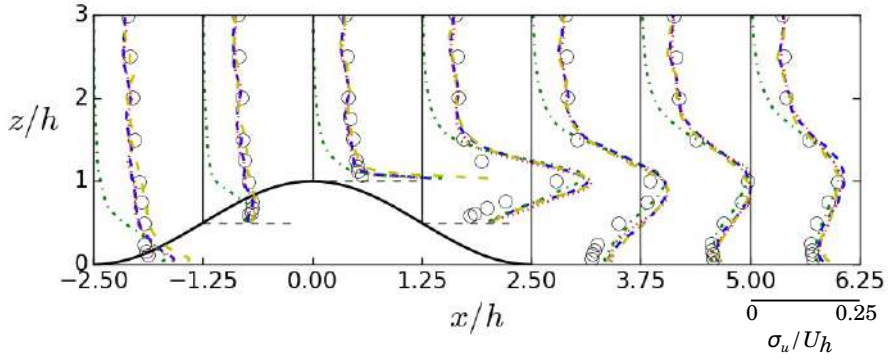

(a)

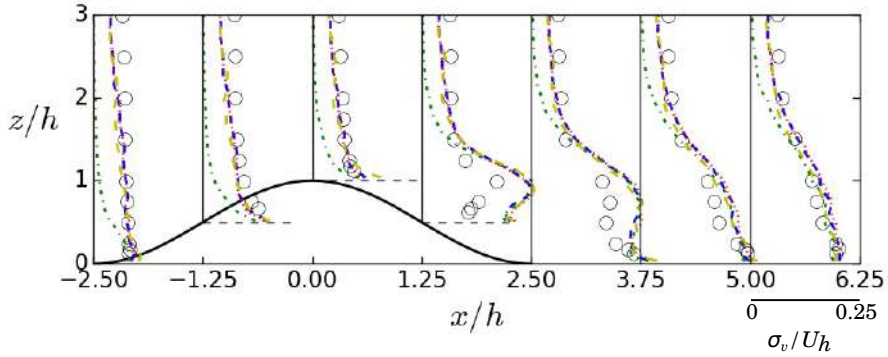

(b)

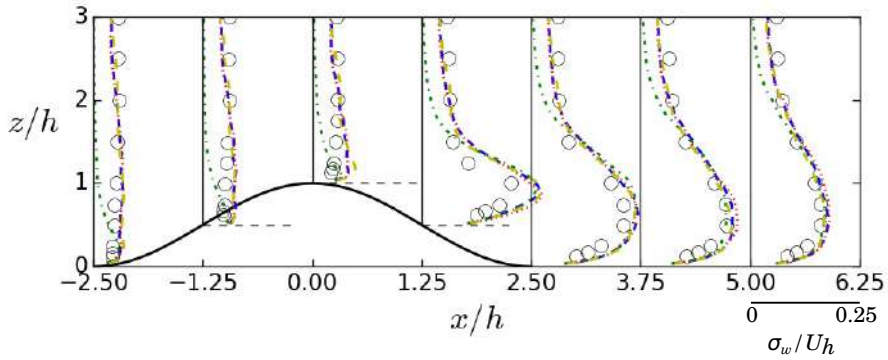

(c)

Figure 3.6: Three-dimensional hill. Vertical profiles of the three normal stress components on the central plane of the hill: (a) σ_u/U_h; (b) σ_v/U_h; (c) σ_w/U_h. Blue dashed lines (- - - -): periodic precursor, red dotted lines (·····): discontinuous precursor, yellow loosely dashed lines (- - - -): synthetic inlet, green dot-dashed lines (-·-·-): laminar inlet, circles (○): experiment (Ishihara et al [102]).

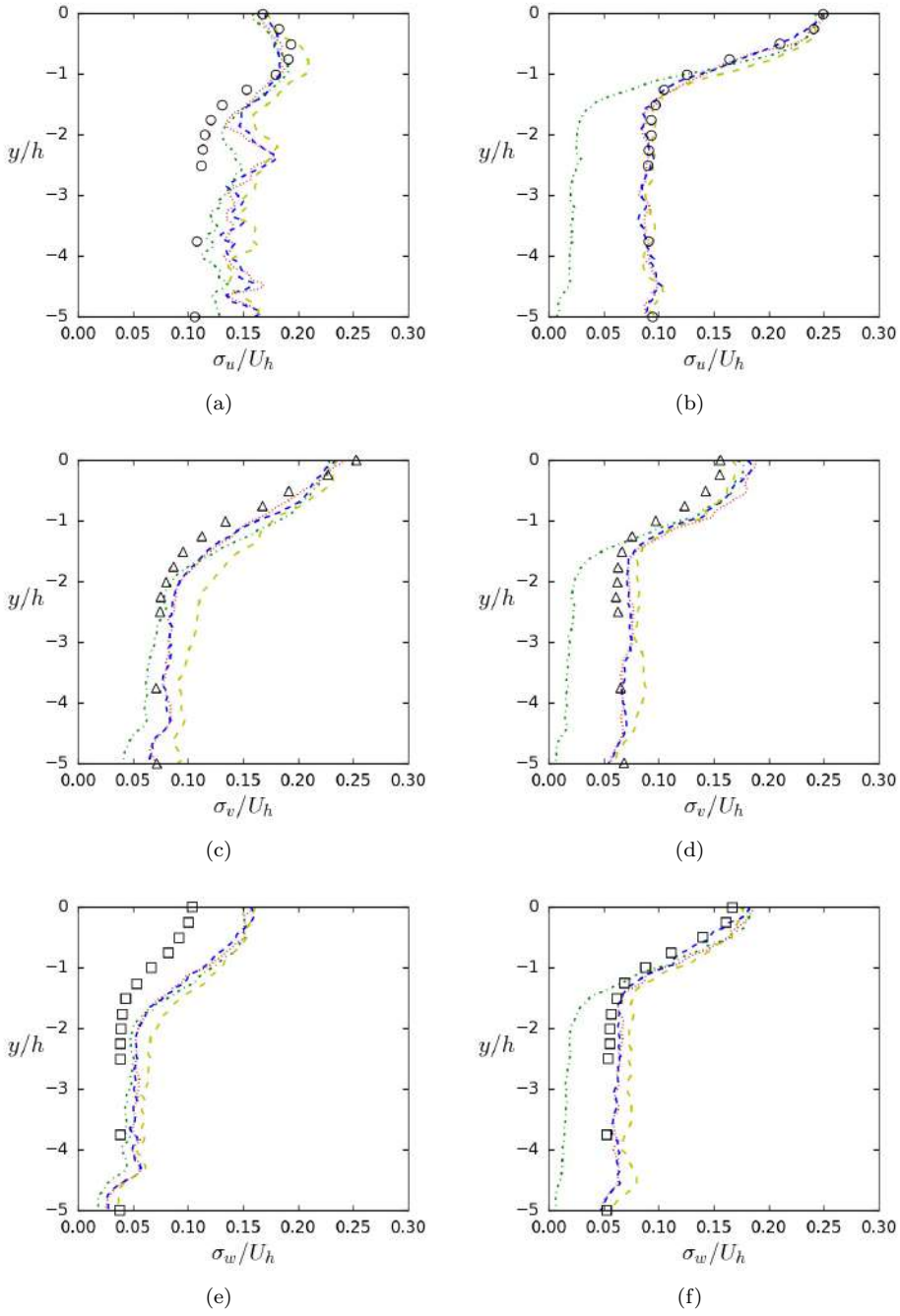

Figure 3.7: Three-dimensional hill. Spanwise distributions of the normal stress components behind the hill at (a-c-e) $x/h = 3.75$, $z/h = 0.125$ and (b-d-f) $x/h = 3.75$, $z/h = 1$. Blue dashed lines (- - - -): periodic precursor, red dotted lines (·····): discontinuous precursor, yellow loosely dashed lines (- - - -): synthetic inlet, green dot-dashed lines (-·-·-): laminar inlet, symbols (○, Δ, □): experiment (Ishihara et al [102]).

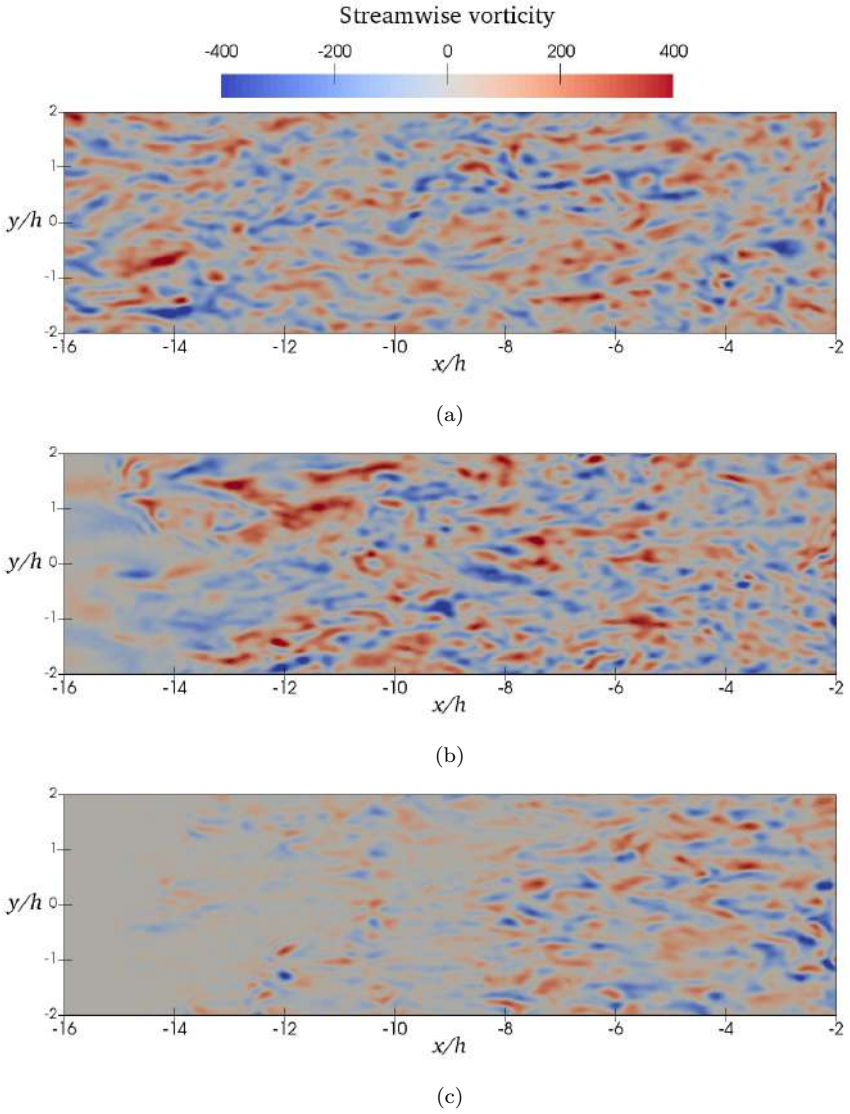

(a)

(b)

(c)

Figure 3.8: Three-dimensional hill. Streamwise vorticity in a region upstream of the hill at height $z/h = 0.125$, for three different inlet conditions: (a) precursor, (b) synthetic, (c) laminar.

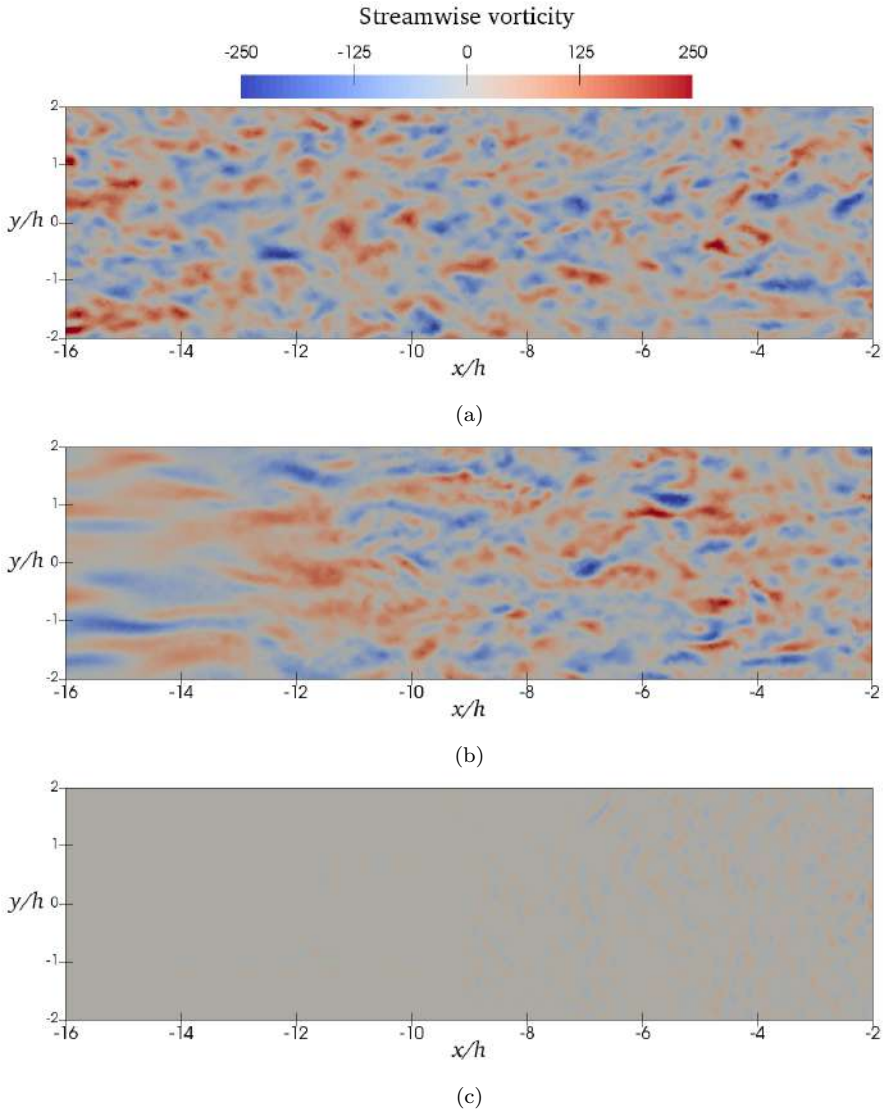

Figure 3.9: Three-dimensional hill. Streamwise vorticity in a region upstream of the hill at height $z/h = 1$, for three different inlet conditions: (a) precursor, (b) synthetic, (c) laminar.

are generated through a diffusion process, is selected. This technique is chosen because of its ease of implementation, as well as the fact that it can be used in arbitrary geometries and unstructured grids.

All the methods are tested in the simulation of a flow over a three-dimensional hill, a case of particular interest, where prescribing a laminar inlet is shown to falter, severely underpredicting the fluctuations in regions away from the wall. Both the precursor and the synthetic method offered results of similar quality, in good agreement with the experimental data. However, it needs to be noted that the precursor simulation imposes a significant additional computational cost. On the other hand, the synthetic method necessitates an a priori specification of a target length scale and also needs knowledge of some quantities of the flow for the scaling procedure. Nevertheless, considering the similar quality of the results from the two methods, the use of a synthetic inlet is suggested, due to the lower computational cost. The two methods are also tested in the flow over the Bolund hill, presented in Section 5.2.

Chapter 4

Wall modelling

4.1 Introduction

Even though LES has found a more widespread use in the simulation of turbulent flows at high Reynolds numbers and complex geometries, it still faces limitations in wall-bounded flows, as the cost to resolve the flow in the near-wall region increases exponentially. Considering that most engineering flows occur in Reynolds numbers of the order of 10^6-10^9, the use of wall-resolved LES is, therefore, limited to flows of moderate Reynolds numbers. In 1979, Chapman [105] presented a complete analysis of grid-resolution requirements for LES of turbulent boundary layers. For this analysis, he separated the flow into an inner layer, where the viscous effects are dominant, and an outer layer, where they are almost negligible on the mean flow. The dynamically important eddies in the outer layer scale with the boundary layer thickness δ. He showed that the number of grid points required in the wall-normal direction is practically independent of the Reynolds number. Under the assumption that the grid size in the tangential directions scales like $Re^{0.2}$ (like the boundary layer thickness), the estimate for the total number of points is proportional to $Re^{0.4}$.

The requirements for the inner layer, however, are much more strict. Quasi-streamwise vortices, of a constant size in wall units, dominate the flow in that region. Thus, a constant grid spacing in wall units must be preserved. He finally estimated that the number of points required to resolve the inner layer is

$$N_{\text{inner}} \propto C_f Re^2$$

which leads to

$$N_{\text{inner}} \propto Re^{1.8}$$

under the assumption that $C_f \propto Re^{-0.2}$.

The cost of a calculation, however, does not only depend on the size of the grid. We need to consider that the equations of motion need to be

advanced for a sufficient amount of time (related to the integral time scale of the flow), in order to obtain converged statistics. Considering that the CFL condition needs to be satisfied in most cases, the time-step is defined as $\Delta t \propto \Delta x/U$, i.e. the number of time-steps is proportional to the number of grid points in one direction. Finally, the total cost of the calculation scales with $Re^{2.4}$ for the inner layer.

More recently, Choi and Moin [106] revisited these estimates, after pointing out that the assumption for the scaling of the skin friction is only valid for low to intermediate Reynolds number range ($Re \leqslant 10^6$) and has been shown to not hold at higher Reynolds numbers. Instead the skin friction coefficient scales with

$$C_f \propto Re^{-1/7}$$

which leads to the following estimation for the number of points required to resolve the inner layer:

$$N_{\text{inner}} \propto Re^{13/7}.$$

It becomes immediately obvious that the cost of fully resolving the inner layer far outweighs that of the outer layer and dominates the simulation. Therefore, the need to minimize or avoid that cost has been identified and modelling the flow in the inner layer has been proposed as an alternative. The basic principle behind wall modelling is that the transport of the momentum in the inner layer has to be modelled, since the grid is too coarse to resolve the dynamically important eddies and just assuming a no-slip condition results in an incorrect velocity profile, and subsequently, wall stress.

Deardorff [107] and Schumann [108] attempted to solve this problem by using approximate boundary conditions similar to the wall functions used in RANS simulations, under the assumption of a constant wall stress. This suggests that a logarithmic layer exists, which can be used to relate the outer layer velocity to the wall stress. In flows of engineering interest, however, those approximate conditions cannot always be applied as the assumption of an equilibrium flow and, subsequently, a logarithmic law does not hold. Various modifications of the Schumann model have proposed ([109, 110, 111, 112]) that account for various parameters such as the roughness of the wall, the elongation of the near-wall structures etc. Piomelli et al. [110] suggested a so-called ejection model, which takes into account the fact that the fast fluid motions toward or away from the wall significantly affect the wall stress. In the modified version of this model by Marusic et al. [112], the model is based on the streamwise component of the velocity instead of the wall-normal one, which is found to yield more accurate results.

Werner and Wengle [113] proposed a model, where they replaced the logarithmic law with a power (1/7) law. Their model functions under they hypothesis that the instantaneous tangential velocity components are in phase with the respective instantaneous wall shear stresses. This model is more

suitable for inhomogeneous configurations, since it does not make use of averaged statistics for the velocity and/or wall stress values. A modification of this model was suggested by Hassan and Barsamian in [114], where the shift that exists in the correlation between the wall friction and the instantaneous velocity is accounted for, similar to the ejection model presented by Piomelli et al. in [110].

Following these early methods, a lot of different approaches have been considered to deal with the near-wall region. They can be categorized in two groups: a) wall stress models and b) hybrid RANS/LES methods. The first category relies on approximate boundary conditions to model the transport of momentum in the inner layer. In these methods, the LES grid is formally defined as extending all the way to the solid wall. The model calculates the wall stress in terms of the outer velocity, which is then provided to the LES as a boundary condition. On the contrary, in the second category the LES does not extend all the way to the wall and instead the wall model is responsible for simulating near-wall flow, with the model and the LES exchanging information at the matching interface. The present work focuses exclusively on the first category. For more extensive reviews on wall modelling, the reader is referred to [6, 115, 116, 117, 118].

In this chapter two different models are evaluated. In section 4.2, an equilibrium wall model is investigated. Instead of focusing on the model itself, we use a simple law of the wall and focus on the way the wall model is applied. We find that the classical finite element approach fails in both theory and practice. In section 4.3, some preliminary work on a two-layer non-equilibrium wall model, that solves the RANS equations on an auxiliary grid, is presented.

4.2 Equilibrium model

4.2.1 Introduction

In this section we focus on the implementation of wall modelling for large eddy simulation in a finite element framework. The standard approach to wall modelling for LES in finite elements is the same as the one typically used in RANS, as described for example in [119, 120, 121, 122]. As opposed to the approach commonly used in finite differences and finite volumes, the mesh does not extend all the way to the wall (i.e., a part of the domain is omitted). Therefore, there exists a thin region of height d between the wall and the first point of the computational mesh (see Fig. 4.1a). The traction is applied at point A with the velocity evaluated at the same point.

Despite its importance for simulation problems of engineering interest, little work has been conducted in regards to wall-modelled LES (WMLES) in a finite element framework. Bazilevs and Hughes [123] proposed an alterna-

tive method to deal with coarse meshes in the near-wall region, through the weak imposition of the boundary conditions using Nitsche's method [124]. The formulation was further enhanced by Bazilevs et al. in [125, 126], by incorporating the law of the wall of Spalding [127] and also imposing the boundary condition in the wall-normal direction in a weak sense, although the primary goal of the latter was ease of implementation. The weak imposition performed considerably better when uniform (and, thus, coarse) grids were utilized, as is often the case in applications of practical interest. However the results were still not very accurate. The concept was further explored in [128, 129], where an additional stress field was utilized for the imposition of boundary conditions. This approach was shown to offer improved, yet still not accurate, results, while also guaranteeing the impermeability of the wall boundaries. Krank and Wall [130] suggested an alternative approach to wall modelling, via the use of a function space that consists of a standard polynomial function space and an enrichment constructed on the basis of Spalding's law of the wall. This modification allows for the boundary layer to be resolved in a mean sense (somewhat resembling Detached Eddy Simulation on that respect) even with coarse meshes. Following the classification proposed in [117], the method they propose is a RANS-LES method, in contrast to the method proposed herein that classifies as a two-layer approach. The method was tested in various configurations using very coarse meshes with surprisingly accurate results. However, questions can be raised in regards to the dissipative nature of their code, since they obtained improved results on higher Reynolds numbers in the turbulent channel flow case, despite keeping a fixed grid.

Kawai and Larsson approached the problem from a different angle (albeit in a finite difference context) in [131]. In order to explain the mismatch between the modelled and the real skin friction that is observed when the wall stress is modelled using the nearest neighboring LES velocity (commonly referred to as Log-Layer Mismatch or LLM), they looked at the error due to the under-resolved LES in the first few grid points off the wall. They noted that there is no inherent requirement to apply a wall model at the first grid point off the wall (as is it typically done in a finite volume or finite difference context), as long as it is applied within the inner part of the boundary layer. This means that the wall model is fed with more accurate information and thus provides a better prediction of the wall shear stress, resolving the LLM problem. Instead of the typical finite difference approach, where the traction is applied on the wall with the velocity evaluated at the first grid point off the wall (points B and C respectively in Fig. 4.1b), they proposed that the velocity is evaluated at a point further away from the wall (e.g. point D in Fig. 4.1b). They called this point exchange location. We will, therefore, refer to the method as the exchange location method. The typical implementation of the wall law in the finite difference community can be regarded as a particular case of the exchange location method.

Yang et al. [132] suggested that the LLM is not caused by the numerical error in the first point off the wall, as proposed in [131], but rather by the unphysically strong coupling between the wall shear stress and the velocity at the first point off the wall. They proposed an alternative solution in which the wall model receives the time-filtered LES velocity at the first point off the wall, which proved to be successful in eliminating the LLM problem. They also showed that the same effect can be achieved through the application of wall-parallel spatial filtering on the wall model input, but noted the difficulty of constructing such spatial filters in unstructured meshes. In addition, they pointed out that while the method proposed in [131] has been useful, it is impractical in complex geometry flows, imposing a large overhead on mesh generation as well as wall model implementation.

De Wiart and Murman performed WMLES in a Discontinuous Galerkin Spectral Element framework in [133]. Using a simple equilibrium wall model and high-order elements, they were able to accurately predict the turbulent channel flow even at Reynolds numbers up to $Re_\tau = 50k$, however the model was unable to correctly predict non-equilibrium flows such as the two-dimensional periodic hills and the NACA 4412 airfoil. In the airfoil case, they experimented with the input location for the wall model, with minimal impact on the results. Frère et al. [134] employed both the aforementioned strategies (from [131] and [132]) in the turbulent channel flow, using a high-order Discontinuous Galerkin code. They observed that applying an averaging procedure on the input of the wall model had no impact on the results. It is important to note, however, that they only applied a "partial" average (cf. Eq. 11 therein), as opposed to the full average suggested in [132]. The traction they imposed was proportional to the instantaneous velocity while the factor of proportionality depended on the average velocity. Instead, in the method proposed in [132] not only does the factor of proportionality depend on the average velocity but the traction is proportional to the average velocity. Since the method used imposes the unphysically strong coupling between the wall shear stress and the velocity of the first point off the wall, it is not expected to introduce a significant improvement according to the findings in [132]. In terms of the input location for the wall model, they found that placing the interface at the bottom of the second element off the wall, massively improved the results compared to placing it at the top of the first element. However, they did not examine locations further away from the wall. Considering the significant differences between the Discontinuous Galerkin and standard finite element methods, we believe that their conclusions are not necessarily transferable to the framework used in this work. For instance, in a continuous finite element approach the velocity is the same at the bottom of the second element off the wall and at the top of the first element.

We adapt the finite difference approach for wall modelling to the finite element framework and compare it with the approach typically used in the

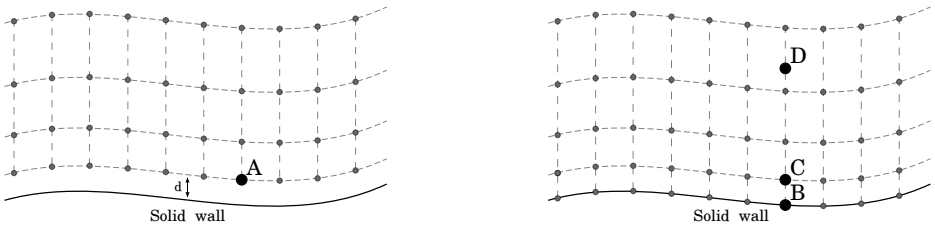

(a) Finite element (b) Proposed approach

Figure 4.1: Wall modelling approach in different spatial discretization methods.

finite element community [119, 120, 121, 122]. We also examine the exchange location method proposed in [131], as well as the application of temporal filtering on the input of the wall model, suggested in [132]. A key contribution of this Chapter is to show that abandoning the classical finite element implementation offers significant improvements in the results.

4.2.2 Explanation of the method

The analytical expression for the shear stress parallel to the wall at a distance $y = d$ from the wall is:

$$\overline{\tau(d)} = \overline{(\mu + \mu_{LES})\frac{\partial u_x}{\partial y}} \Big|_{y=d} - \rho\overline{u_x' u_y'} \Big|_{y=d} \tag{4.1}$$

where x and y correspond to the streamwise and wall-normal directions respectively, while μ_{LES} refers to the turbulent viscosity introduced by the subgrid-scale model (if one is used). The first term of the RHS of Eq. 4.1 refers to the viscous and the modelled stress, while the second term refers to the resolved stress.

In the following, three different approaches to model Eq. 4.1 are presented: i) the typical approach used in finite elements, ii) the typical approach used in finite differences and iii) the exchange location method. It is worth noting at this point that an open integration rule is used in the simulations, i.e., the calculations are performed at the boundary gauss points and the corresponding exchange location points. However, we refer to grid points in the following, as if a closed (nodal) integration rule was used, in order to make an easier comparison between the finite element and finite difference approaches.

Classical finite element approach

The most commonly used approach for wall modelling in finite elements is to consider a mesh that does not extend all the way to the wall, as shown in

Fig. 4.1a (see also [119, 120, 121, 122]). In this approach, the layer between the wall and the first grid point (A) is not directly resolved. Instead it is modelled through a wall function. The velocity at point A and the so-called "wall distance" between that point and the wall (denoted by d in Fig. 4.1a) are typically used to calculate the shear stress ($\tau(d)$), which is then imposed at point A. In addition, a no-penetration condition is imposed at that point.

This method imposes the following conditions on point A ($y = d$):

$$\overline{\tau(d)} = \overline{(\mu + \mu_{LES})\frac{\partial u_x}{\partial y}} \Big|_{y=d} \tag{4.2}$$

$$u_y = 0 \tag{4.3}$$

where the no-penetration condition (Eq. 4.3) means the resolved stress is equal to zero. Comparing Eq. 4.1 and 4.2, we see that the classical approach does not account for the effect of the resolved stress at $y = d$. Since the total shear stress is well calculated due to momentum conservation, this leads to an inaccurate prediction of the velocity gradient, i.e., the method suffers from severe Log-Layer Mismatch.

Following the classification presented in [117] for wall modelling, this method is essentially equivalent to a hybrid LES/RANS model, since the LES is not formally defined as extending all the way to the wall.

Classical finite difference approach

An alternative method proposed here involves following the approach commonly used for wall modelling in finite differences. In this approach, the grid extends all the way to the solid wall (Fig. 4.1b) and we are, in fact, imposing the wall shear stress at $y = 0$, in terms of the velocity evaluated at $y = d$, where d now denotes the distance between the first grid point (B), which now coincides with the wall, and the first grid point off the wall (C). Due to the fact that this velocity has a non-zero vertical component, the problem outlined in the previous paragraph in regards to the resolved stress being zero at a distance $y = d$ from the wall is solved. It is worth noting that, since in this case we are actually resolving the near-wall part of the domain, we are indirectly imposing the following shear stress at point B:

$$\overline{\tau(d)} = \overline{(\mu + \mu_{LES})\frac{\partial u_x}{\partial y}} \Big|_{y=d} - \rho\overline{u'_x u'_y} \Big|_{y=d} \approx \overline{\tau(y=0)} + \overline{\frac{\partial p}{\partial x}} d \tag{4.4}$$

where the last approximation stems from integrating the Navier-Stokes equations in the near-wall elements.

As opposed to the classical finite element approach, this method is equivalent to a wall-stress model (again following the classification of [117]), where a wall model is solved over a layer of thickness d.

Exchange location

The finite difference approach provides an additional opportunity (as explained in [131]). A very typical problem of wall modelling is that, even with a perfect wall model, the results would still be inaccurate, since the LES is under-resolved in the near-wall part of the domain (e.g. at the first grid point off the wall) and thus provides inaccurate information to the wall model. There is, however, no requirement for the velocity to be evaluated at the first grid point off the wall. As mentioned earlier, the only requirement is that the velocity is evaluated at a point located within the inner part of the boundary layer, where the wall functions are typically valid. The use of the exchange location method allows us to place the exchange interface (i.e. the point where the LES feeds information to the wall model) further away from the wall (such as point D in Fig. 4.1b), where the LES is more accurately resolved and, therefore, can provide a more accurate prediction for the wall shear stress.

An issue arising with this method is that, in very complex geometries, it could happen that certain exchange location points are placed outside of the computational domain. To that end, we have developed an adaptive procedure that locates the missing points and gradually reduces the distance from the corresponding wall, until the point is located inside the computational domain. This procedure is used in the realistic car model DrivAer case in Section 5.1. Moreover, no additional meshing effort is required in our experience.

4.2.3 Parallel implementation

Normally, in a parallel simulation, it is not possible to know in advance which parallel processes the exchange interface will be located in. It is also to be expected that partitions requiring information for the wall model will not host the needed exchange location points and thus communications will be necessary. To that end, a pre-process stage to construct a communication scheme is proposed in Algorithm 2. Given that all the partitions perform the same tasks, the description is done in terms of one of them.

A graphical description of this procedure is shown in Fig. 4.2, where the bounding box of the exchange location points of partition 1 is shown together with the bounding box of partitions 2 and 3. In this example, partition 1 will receive information from partitions 2 and 3. It is important to note that this procedure is not necessary for the classical finite difference approach (i.e., when the exchange location is placed at the first grid point off the wall), which is a significant advantage in terms of the simplicity of implementing the method in a finite element code.

Algorithm 2 Definition of the communication scheme for the exchange location method.

- Define the bounding box of my physical domain.
- Exchange bounding boxes with all other partitions.
- Define a bounding box containing my exchange location points and check for intersections with the bounding boxes of other parallel partitions. If there is an intersection, mark the partition as a neighbor.
- Send the coordinates of my needed points to my neighbors and receive coordinates from them.
- For each neighbor, check if their needed points are contained in my elements. Mark the contained points as 'hosted nodes'.
- Exchange the hosted nodes' list with my neighbor partitions.
- Build the communications scheme according to the 'hosted nodes' lists.

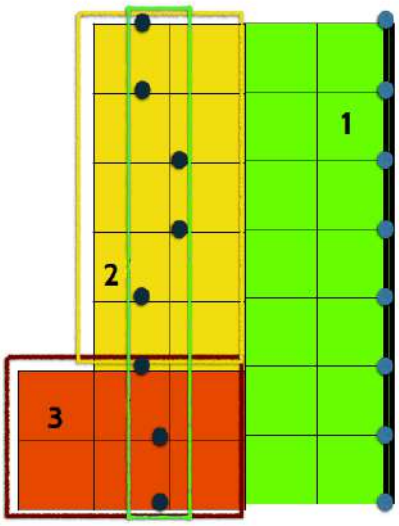

Figure 4.2: Neighbouring subdomains containing the exchange location points.

4.2.4 Wall modelling tools

Two different wall functions are utilized in the tests performed in this work, one for smooth walls and the other one for rough walls. These wall functions are used to calculate the friction velocity u_*, based on the LES velocity that the model receives as an input, which is subsequently used for the calculation of the wall shear stress through the expression $\tau_w = \rho u_*^2$. Reichardt's extended law of the wall [135]:

$$u^+ = \frac{1}{\kappa} ln\left(1 + \kappa y^+\right) + 7.8 \cdot \left(1 - e^{-\frac{y^+}{11}} - \frac{y^+}{11} \cdot e^{-0.33y^+}\right) \tag{4.5}$$

is used in the turbulent channel and wall-mounted hump cases, where $u^+ = \frac{u}{u_*}$ and $y^+ = \frac{yu_*}{\nu}$ denote the dimensionless velocity and wall distance respectively, and $\kappa = 0.41$ is the von-Kárman constant. Ideally, a single wall model would be utilized in all the cases presented, in order to avoid adding an extra degree of freedom in the assessment of the method. However, due to the roughness of the wall in the atmospheric boundary layer case, we use the logarithmic law for rough walls and neutral stability:

$$u_y = \frac{u_*}{\kappa} ln\left(\frac{y + y_0}{y_0}\right) \tag{4.6}$$

commonly used in environmental simulations. Here u_y denotes the mean wind speed at height y and y_0 denotes the surface roughness.

In addition, an exponential running average similar to the one proposed by Meneveau et al [136] is used to account for the time-average nature of the wall functions utilized. For any quantity ϕ, the local time average $\overline{\phi}$ at any time t_n is defined as:

$$\overline{\phi}^n = \epsilon\phi^n + (1 - \epsilon)\overline{\phi}^{n-1}$$

The weighting parameter ϵ is defined as:

$$\epsilon = \frac{\delta t}{T}$$

where δt is the computational time-step and T is the characteristic averaging time-scale, chosen to be comparable to the convective time scale of the problem. In this method, the time-averaging is applied to the velocity that is used as the input for the wall model, in a similar fashion to [132]. We have confirmed in our numerical experiments that the process is insensitive to the precise value of T, as pointed out by Yang et al. in [132], provided that it is large enough (not shown here).

4.2.5 Turbulent Channel Flow at $Re_\tau = 2003$

To assess the performance of our method, we investigate a turbulent channel flow at $Re_\tau = 2003$ with a setup similar to the one used in [126], where Re_τ is the friction Reynolds number based on the friction velocity and channel half width. We compare the two variations of the exchange location with the classical FE approach, using the DNS results of [137] as reference data.

The size of the computational domain considered herein is $6\pi\delta \times 2\delta \times 2\pi\delta$ in the streamwise, wall-normal and spanwise directions respectively, where δ is the channel half-width. The streamwise and spanwise directions are assumed to be homogeneous, and thus periodic boundary conditions are applied, while a no penetration condition is imposed on the wall boundaries.

Meshes of 64^3 (G1), $128 \times 96 \times 96$ (G2) and $256 \times 128 \times 128$ (G3) linear elements that are uniform in all directions are employed. That results in $y^+ \approx 63$, $y^+ \approx 42$ and $y^+ \approx 31$ respectively at the first node. The reference DNS used a $6144 \times 633 \times 4608$ mesh on a domain with size $8\pi \times 2 \times 3\pi$ in the streamwise, wall-normal and spanwise directions respectively. The flow is driven by a constant pressure gradient in the streamwise direction.

The simulation is run for an appropriately long time to guarantee that a statistically stationary regime is reached. Once that quasi-steady state has been achieved, statistics are collected, and the results are averaged in time for approximately 24 flow-through units (we define a flow-through unit as $t = L_x/U$ where U denotes the velocity at the center of the channel and L_x is the size of the domain in the streamwise direction). They are subsequently averaged in space (in the streamwise and spanwise direction) and non-dimensionalized using the computed friction velocity. Reichardt's extended law of the wall (Eq. 4.5) is used for modelling the wall layer. The averaging period T is equal to two flow-through units.

Three alternatives for applying the wall law are compared. In the first one, which will be labeled "classical" approach in the following, we employ the standard FE approach to wall modelling, as described in Section 4.2.2. The wall distance is set equal to the height of the elements ($d = h_{el}$). The remaining two make use of the exchange location method (cf. Section 4.2.2) at two different locations: one on the first grid point off the wall and the other at a distance of $y = 0.125\delta$ (coinciding with the fourth grid point off the wall). The second location is intentionally chosen to be at the limit of the wall law's validity, to evaluate the approach proposed in [131]. We note here that it is not necessary for the exchange location to coincide with the grid points. Additionally, we evaluate the effect of using temporal averaging on the input velocity of the wall law (as described in Section 4.2.4), by performing the two exchange location simulations with and without averaging. The identifier "noav" is used to denote the cases without temporal

averaging.

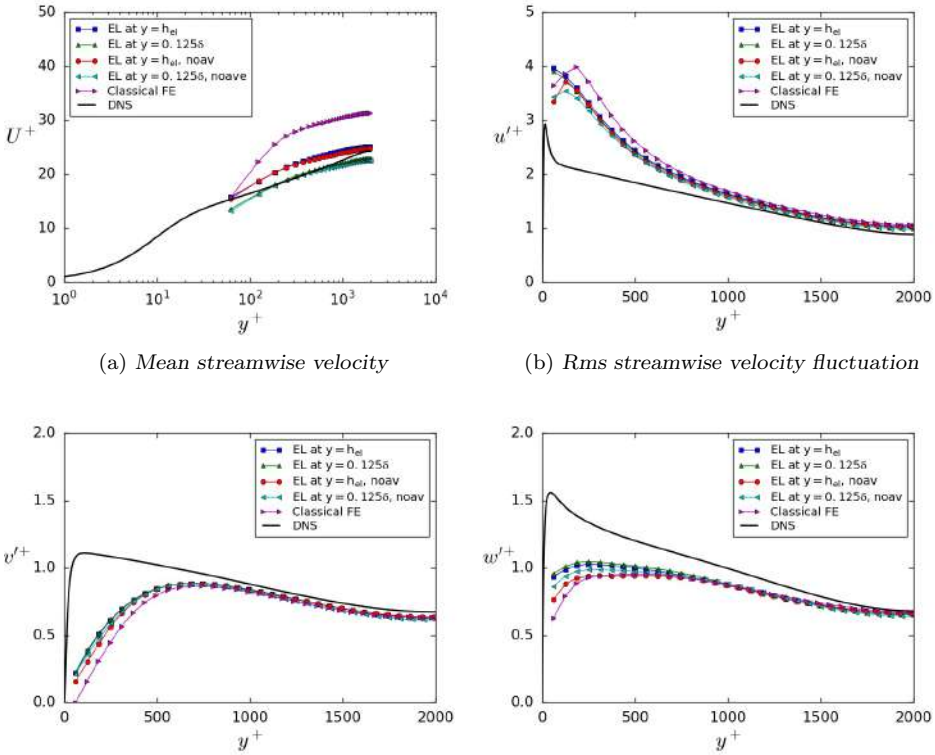

(a) *Mean streamwise velocity*

(b) *Rms streamwise velocity fluctuation*

(c) *Rms wall-normal velocity fluctuation*

(d) *Rms spanwise velocity fluctuation*

Figure 4.3: Mean streamwise velocity and rms velocity fluctuations, for grid G1.

Results for the mean streamwise velocity are presented in Fig. 4.3a, for grid G1. It becomes immediately obvious that the classical FE approach cannot accurately predict the flow, resulting in a vast overprediction of the mean streamwise velocity. Specifically, the velocity at the first grid point is in agreement with the DNS data (as expected, since that is the point where the wall law is applied), however the velocity gradient is inaccurately predicted in the first few near-wall elements resulting in a significant error in the mean streamwise velocity as we approach the core of the channel. This overprediction is a result of omitting the resolved part of the stress as explained in Section 4.2.2, leading to a severe Log-Layer Mismatch. The results from the classical FE approach are similar to the ones in [126]. When the exchange location is used, however, the prediction for the mean flow is significantly more accurate. Placing the exchange location further away from the wall offers a slight improvement in the results. However, both exchange location simulations fail to accurately capture the shape of the DNS results.

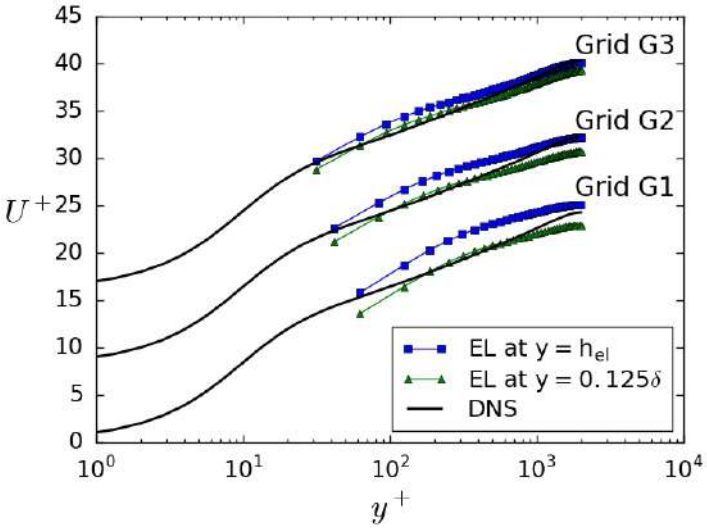

Figure 4.4: Mean streamwise velocity for grids G1, G2 and G3, each shifted upward by 8 units for clarity.

Additionally, it is interesting to note that the use of temporal filtering has minimal impact on the results.

The differences between methods are smaller when looking at the fluctuations, but still noticeable (Fig. 4.3b - 4.3d). All simulations overpredict the fluctuations in the streamwise direction in the near-wall region while underpredicting the wall-normal and spanwise fluctuations. The predictions are much more accurate as we approach the core of the channel. This behavior is expected since the wall law only accounts for the mean velocity profile and the coarse mesh employed does not allow for the near-wall part of the fluctuations to be accurately resolved. Another possible cause is the use of linear elements since they typically falter in accurately predicting the fluctuations near the wall (cf. [27]). That said, the exchange location method still offers an improvement in results, especially near the wall. Small improvements in the results can also be observed when time filtering is used. We also have to note the fact that $v' = 0$ at $y \neq 0$ for the classical implementation of the wall law in the finite element context, which is an inherent problem of the method.

The influence of grid refinement on the velocity and its fluctuations, when the exchange location method with temporal averaging is used, can be seen in Fig. 4.4 and 4.5 respectively. It is clear that refining the grid offers a significant improvement in the prediction for the mean streamwise velocity, with the prediction for grid G3 being very close to the DNS results, especially when the exchange location is placed at $y = 0.125\delta$. The improvement

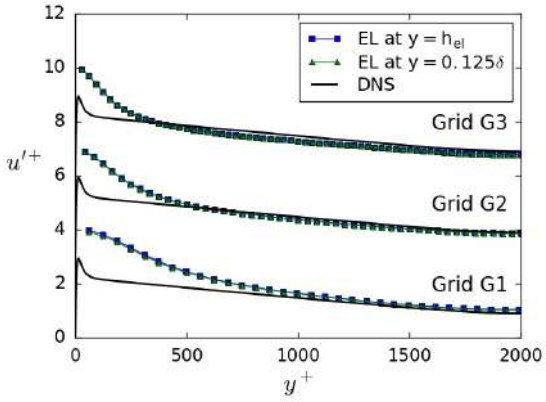

(a) *Rms streamwise velocity fluctuations*

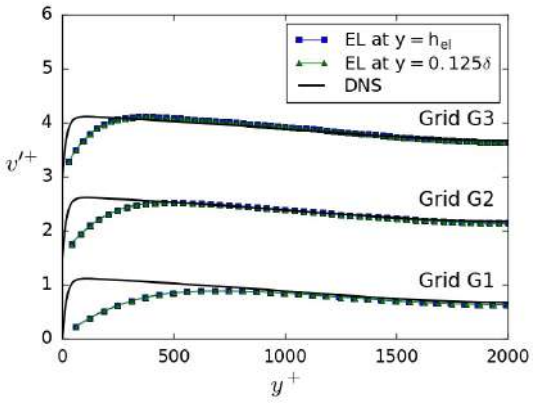

(b) *Rms wall-normal velocity fluctuations*

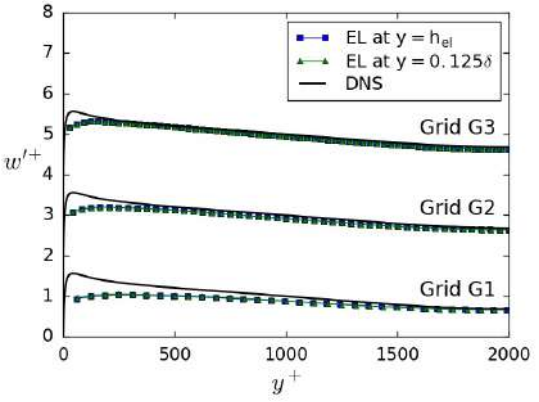

(c) *Rms spanwise velocity fluctuations*

Figure 4.5: Rms velocity fluctuations for grids G1, G2 and G3, each shifted upward for clarity.

is smaller for the fluctuations, but still noticeable. Simulations using the classical FE method were also performed for grids G2 and G3, with similar trends to those of grid G1 (not shown here). The effect of placing the exchange location at the third and fourth grid point off the wall was also examined on all grids, however the results were almost identical to those with the exchange location at $y = 0.125\delta$.

We would like to emphasize the superior performance of the exchange location compared to the classical FE approach. Even when the exchange location is considered at the first grid point off the wall (which is essentially the standard finite difference approach adapted to finite elements), the improvement in results over the classical FE approach is astounding. It is interesting to note that despite the equivalence between finite elements and finite differences when structured grids and a closed integrating rule are used (cf. [138]), the approach when it comes to wall modelling is radically different. Here, we demonstrate that the finite difference approach is significantly more accurate. We believe this to be an important result, especially given the simplicity of the method and its implementation in a finite element code.

Apart from the results presented here, the method was also tested with the VMS formulation in the 64^3 mesh, Fig. 4.6. Similar conclusions can be drawn, with the difference between the classical FE method and the exchange location method being even higher. This is to be expected since there is no eddy viscosity to partially counteract the LLM problem (cf. Section 4.2.2 and Eq. 4.2 therein), and therefore the increase in the velocity gradient is even higher. Additionally, the prediction of the mean streamwise velocity is notably more accurate when the exchange location is moved further away from the wall. The VMS formulation is shown to significantly overpredict the velocity fluctuations, which is in agreement with the lower Reynolds number cases (Section 2.4). It is important to also note the oscillatory behavior in the near-wall region, especially when the classical FE method is paired with the VMS formulation, most evident when looking at the rms velocity fluctuations in the wall-normal direction.

Another important observation is that, in contrast with the low Reynolds number cases (cf. Section 2.4.3-2.4.4), the predictions are improved when the constant is set to $c_2 = 2$, even for the mean streamwise velocity (a closer view can be seen in Fig. 4.7). This further proves the issue that was highlighted in Chapter 2, where an ad hoc tuning of the stabilization constants, based on the case and Reynolds number, is necessary in order to obtain the best results.

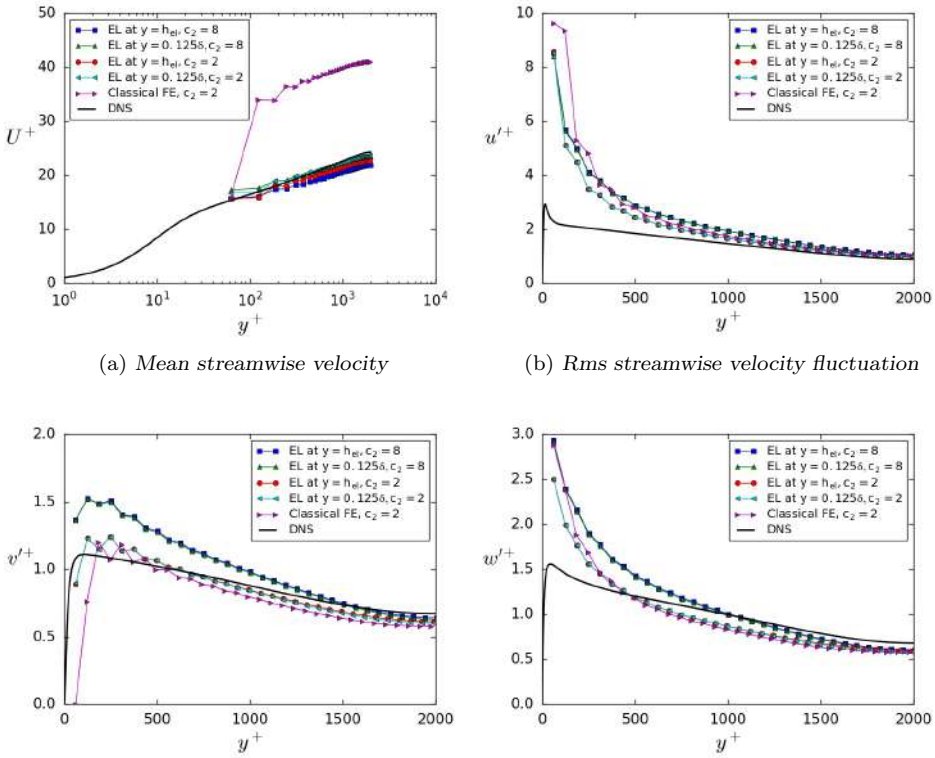

(a) *Mean streamwise velocity*

(b) *Rms streamwise velocity fluctuation*

(c) *Rms wall-normal velocity fluctuation*

(d) *Rms spanwise velocity fluctuation*

Figure 4.6: Mean streamwise velocity and rms velocity fluctuations, for the 64^3 mesh, with the VMS formulation.

4.2.6 Atmospheric Boundary Layer

A large scale environmental flow, namely the neutral atmospheric boundary layer flow over a flat terrain is considered in this section. The very high Reynolds number of environmental flows (here, $Re_\tau = 2.98 \times 10^7$) makes the use of wall modelling imperative and the coarse resolutions used provide an excellent test for the assessment of wall modelling approaches. The size of the computational domain examined herein is $H = L_y = 1000$ m in the vertical direction and $L_x = L_z = 2\pi L_y$ in the tangential directions. The computational grid consists of 53 uniform elements in each direction. Periodic boundary conditions are imposed in the tangential directions. A stress-free condition is imposed at the upper boundary, while a no-penetration condition is imposed at the bottom and top boundaries. The logarithmic law (Eq. 4.6) is used to model the wall layer at the bottom boundary. The values chosen for the friction velocity and roughness length are $u_* = 0.45$ m s^{-1} and $y_0 = 0.1$ m respectively. Statistics are collected once the quasi-steady state

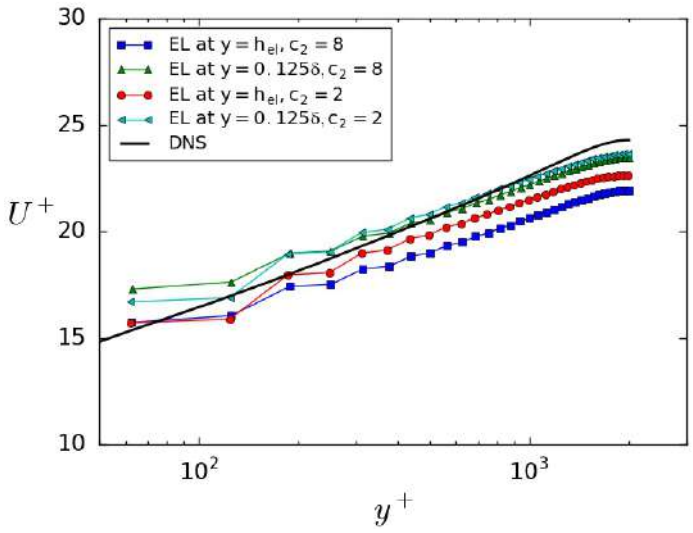

Figure 4.7: Closer view of the mean streamwise velocity, with the VMS formulation.

has been achieved, and the results are averaged in time for approximately 50 flow-through units (here we define a flow-through unit as $t = U_{top}/L_x$, where U_{top} is the velocity at the top of the domain and L_x is the size of the domain in the streamwise direction), and subsequently in space (in the streamwise and spanwise direction). The averaging period T is set equal to one flow-through unit.

Fig. 4.8 presents the results for the mean streamwise velocity compared with the theoretical values from the log-law. As observed, both the exchange location simulations offer more accurate predictions than the one using the classical FE method. Especially the results from the exchange location at the third point are very similar to the theoretical values, albeit with a slight underprediction at the part between the wall and the exchange location.

Another quantity of interest in the study of environmental flows is the non-dimensional vertical gradient of the mean streamwise velocity, defined as $\Phi = (\kappa y/u_*)(dU/dy)$. It can be seen in Fig. 4.9 that all simulations deviate from the theoretical value of 1 in the near-wall region. Nevertheless, the results are noticeably better for the simulations using the exchange location method, with the error being significantly higher in the near-wall region when using the classical FE method.

It is noteworthy that the results when the exchange location is placed at the third grid point off the wall are of similar quality to the ones presented in the literature [139, 140].

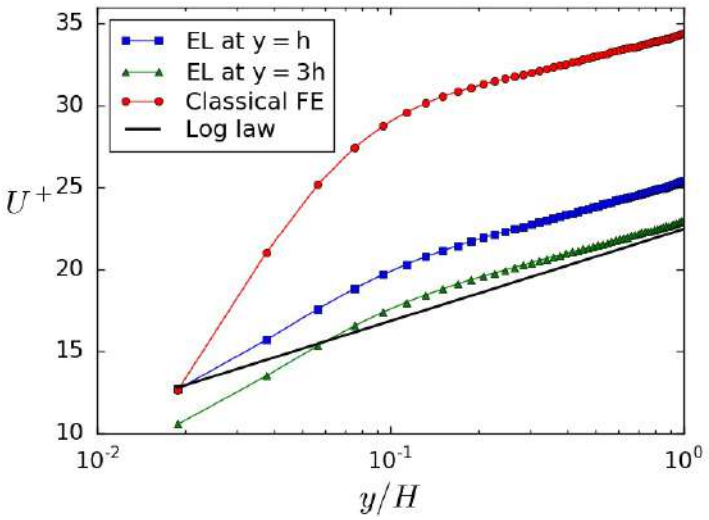

Figure 4.8: Atmospheric boundary layer. Mean streamwise velocity.

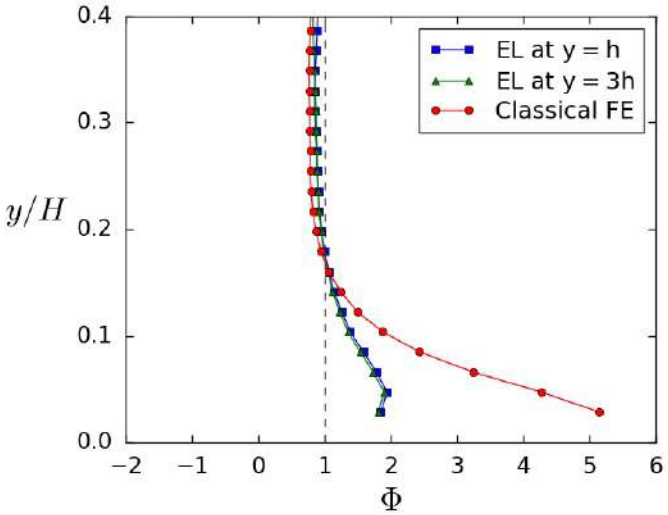

Figure 4.9: Atmospheric boundary layer. Non-dimensional gradient of the mean streamwise velocity, $\Phi = \left(\frac{\kappa y}{u_*}\right)\left(\frac{dU}{dy}\right)$.

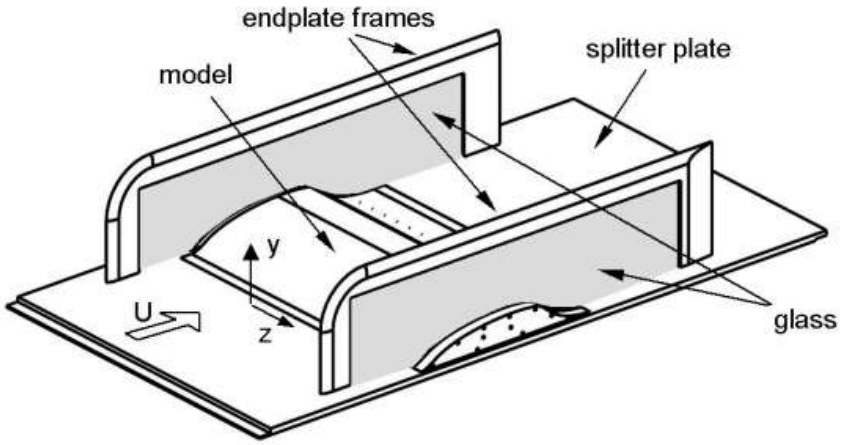

Figure 4.10: Experimental setup for the hump case.

4.2.7 Wall-mounted hump

In this section, we consider the flow over a wall-mounted hump. The features of this flow, where separation, reattachment and recovery of the boundary layer occur, are of special interest, as they appear in several industrial applications. The configuration of the flow is based on the one presented by Park in [141], and the results are compared with the experimental data of Greenblatt et al. [142]. The size of the computational domain is $4.64c$, $0.909c$ and $0.3c$ in the streamwise (x), normal (y) and spanwise (z) directions respectively, where c is the chord length of the hump. The inlet and outlet planes lie at $x/c = -2.14$ and $x/c = 2.5$ respectively with the leading edge of the hump at $x/c = 0$. The top wall is contoured with a small constriction (see Fig. 4.11) between $x = -0.5$ and $x = 1.5$ to account for the presence of the side-plates in the experiments (Fig. 4.10), following the guidelines of the NASA CFDVAL2004 workshop.

The Reynolds number of the flow is $Re = 936000$, based on the hump chord length c and the free stream velocity U_∞ at the inlet. A slip boundary condition is imposed at the top boundary, while periodicity is used in the spanwise direction. A no-penetration condition is imposed at the bottom boundary, with the wall stress being fed into the simulation through the wall model (Reichardt's extended wall law is used, Eq. 4.5). The averaging period is set to $T = 10c/U_\infty$, corresponding to approximately two flow-through units.

Two different grids are utilized in the simulations. The coarse grid (G1) consists of approximately 3.1 million linear elements, with $743 \times 71 \times 61$

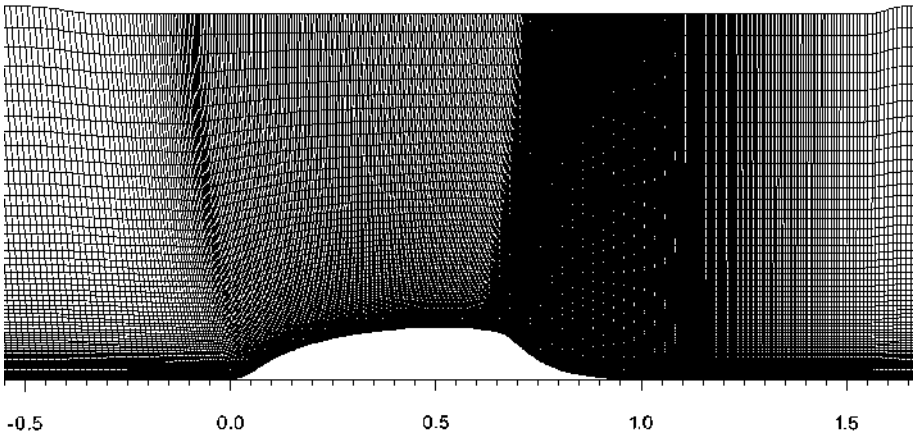

Figure 4.11: Computational mesh from grid G1 in the vicinity of the hump.

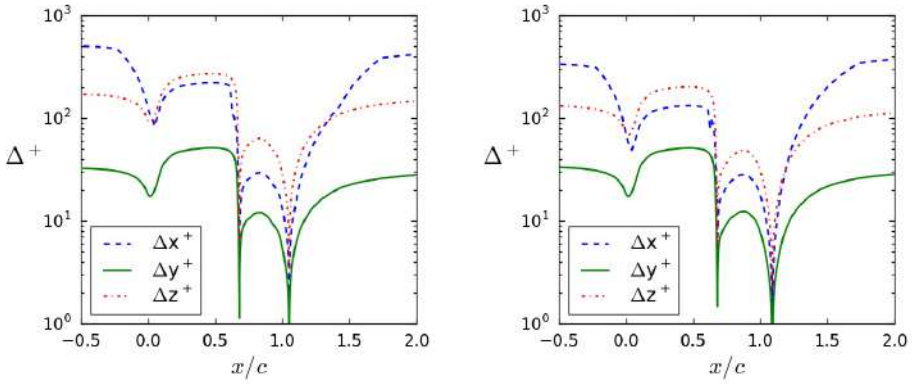

(a) *Coarse grid (G1)* (b) *Fine grid (G2)*

Figure 4.12: Grid spacings in wall units for the two grids.

nodes in the streamwise, normal and spanwise directions respectively. In the fine grid (G2) significant refinement was performed in the tangential directions. In the wall-normal direction, the first grid point was kept at the same distance from the wall (thus y^+ remained the same), so that it remains outside of the buffer layer, however the node density was increased, resulting in a reduction of the growth rate (from 1.06 for the coarse mesh, to 1.03). This resulted in approximately 8 million linear elements, with $901 \times 111 \times 81$ nodes in the streamwise, normal and spanwise directions respectively. Fig. 4.11 presents the mesh in the vicinity of the hump for grid G1, and the dimensionless grid spacings at the wall can be seen for both grids in Fig. 4.12.

Turbulent inflow data are synthesized through the use of the digital filtering technique by Kempf et al. [96] described in Section 3.2, with the target length scale set to $L = 0.25\delta_{in}$, where δ_{in} denotes the thickness of boundary layer at the inflow plane. Due to the limited experimental data at the inflow, the missing Reynolds stresses were specified to match those used by Park in [141] (left panels of Fig. 4.13). To ensure that realistic turbulence evolves before the flow reaches the hump, the mean velocity and Reynolds stresses from the present simulations are compared to those from the WMLES of Avdis et al. [143], at a downstream location ($x/c = -0.81$), shown in the right panels of Fig. 4.13, for grid G2. A slight overprediction can be observed for the streamwise Reynolds stress, which is consistent with the results presented in the turbulent channel flow in Section 4.2.5. However, the general agreement is acceptable.

Statistics are collected over approximately 20 c/U_∞ units of time, after the quasi-static state has been reached. The results are subsequently averaged in the spanwise direction.

Three different exchange locations are examined for this case. Aside from the exchange location at the first and third grid point off the wall, we also examine placing the exchange location at a higher point of the inner layer, without reference to the LES grid, as suggested in [117] and [131]. To that end, we choose $y = 0.125\delta_{in}$.

The predictions for the skin friction and pressure coefficients with grids G1 and G2 are presented in Fig. 4.14 and Fig. 4.15 respectively. The results indicate that the exchange location method predicts the behavior of the flow more accurately than the classical FE method for both grids. The improvement in the prediction of the skin friction coefficient is remarkable, especially in the case of the exchange location at $y = 0.125\delta_{in}$, where the prediction for the skin friction prior to the separation is essentially identical to that of the experiments. A discrepancy is observed within the recirculation region. However, that is to be expected since a simple equilibrium model has been used. The separation and reattachment points are more accurately predicted when the exchange location method is used (cf. Table 4.1) for both grids. A significant improvement in the position of the reat-

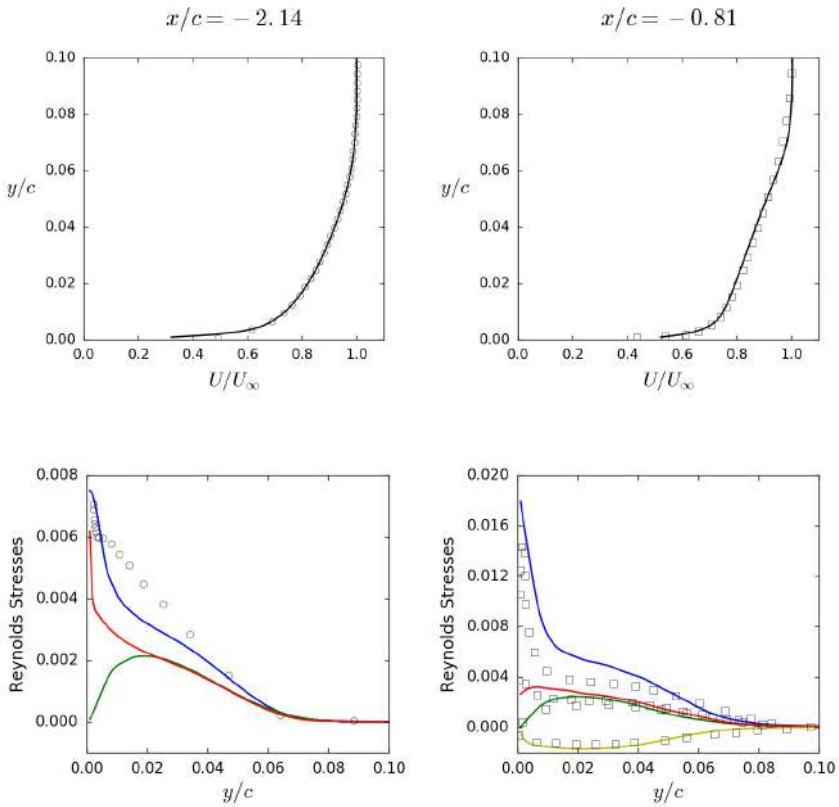

Figure 4.13: Mean streamwise velocity and Reynolds stress at the inflow ($x/c = -2.14$) and a downstream location ($x/c = -0.81$), for grid G2. Blue lines (——): $u'u'$, green lines (——): $v'v'$, red lines (——): $w'w'$, yellow lines (——): $u'v'$, circles (○): experiment (Greenblatt et al. [142]), squares (□): WMLES (Avdis et al. [143]).

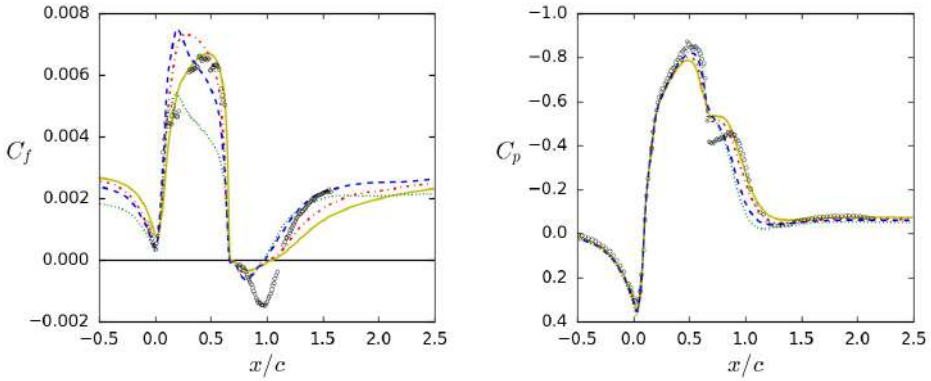

(a) *Skin friction coefficient* (b) *Pressure coefficient*

Figure 4.14: Grid G1: Influence of the point where the velocity is evaluated on the skin friction (a) and pressure (b) coefficients across the streamwise direction. Green dotted lines (·····): classical FE method, blue dashed lines (- - - -): exchange location at first grid point, red dash-dotted lines (-·-·-): exchange location at third grid point, yellow solid lines (——): exchange location at $y = 0.125\delta_{in}$, circles (○): experiment (Greenblatt et al. [142]).

tachment point is obtained when the mesh is refined. Once more, the best results are obtained in the case of the exchange location at $y = 0.125\delta_{in}$. In terms of the pressure coefficient, all the simulations offer similar predictions. A slight underprediction is observed on the attached part of the hump when the exchange location is placed at $y = 0.125\delta_{in}$, however the shape of the "plateau" observed in the experiments around $x/c \approx 0.7 - 0.9$ is more accurately predicted.

The profiles for the velocity and its fluctuations at different streamwise positions are presented in Fig. 4.16 and 4.17 for grids G1 and G2 respectively. All methods capture the mean streamwise velocity profiles acceptably, even though a simple equilibrium wall model has been used. The results from the classical FE method show the highest deviation from the experiment inside the recirculation region. Due to the underprediction of the wall shear stress prior to the separation (Fig. 4.14a and 4.15a), the boundary layer carries too high momentum, resulting in early reattachment (Table 4.1) and, thus, an overprediction of the velocity profiles downstream of the reattachment point.

We observe that all the simulations struggle to accurately predict the Reynolds stresses within the recirculation zone, with the predictions improving downstream of the reattachment point. The discrepancies with respect to the experimental results are similar to those observed in [141]. There exists, however a marked improvement when placing the exchange location

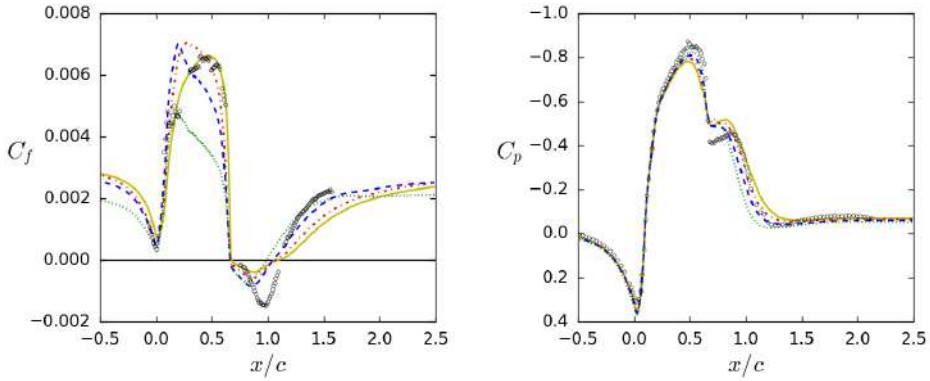

(a) *Skin friction coefficient* (b) *Pressure coefficient*

Figure 4.15: Grid G2: Influence of the point where the velocity is evaluated on the skin friction (a) and pressure (b) coefficients across the streamwise direction. Green dotted lines (·····): classical FE method, blue dashed lines (- - - -): exchange location at first grid point, red dash-dotted lines (-·-·-): exchange location at third grid point, yellow solid lines (——): exchange location at $y = 0.125\delta_{in}$, circles (○): experiment (Greenblatt et al. [142]).

Simulation	Grid	x_{sep}/c	x_{reatt}/c	$(x_{reatt})_{error}$
Classical FE	G1	0.665	0.97	11.8%
EL at 1st point	G1	0.665	0.99	10.0%
EL at 3rd point	G1	0.665	1.03	6.3%
EL at $h = 0.125\delta_{in}$	G1	0.67	1.05	4.5%
Classical FE	G2	0.665	0.985	10.5%
EL at 1st point	G2	0.665	1.05	4.5%
EL at 3rd point	G2	0.665	1.07	2.7%
EL at $h = 0.125\delta_{in}$	G2	0.67	1.09	0.9%
Experiment	-	~ 0.665	~ 1.1	-

Table 4.1: Wall-mounted hump. Separation (x_{sep}) and reattachment (x_{reatt}) locations for the different configurations.

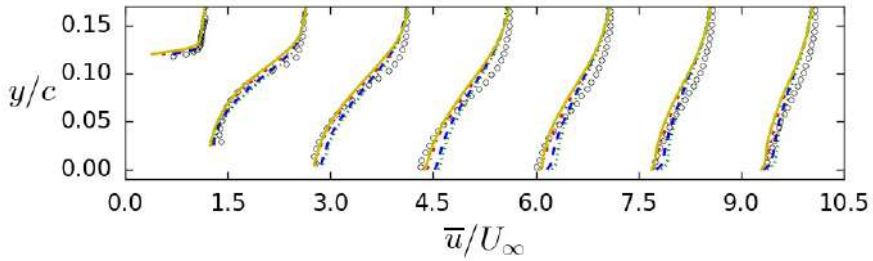

(a) *Mean streamwise velocity profiles shifted by* $\Delta = 1.5$

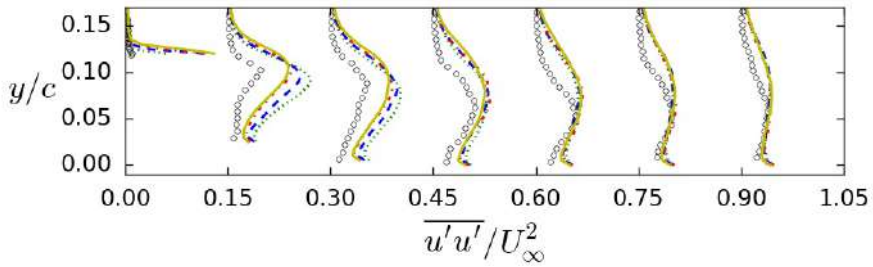

(b) *Streamwise Reynolds stress profiles shifted by* $\Delta = 0.15$

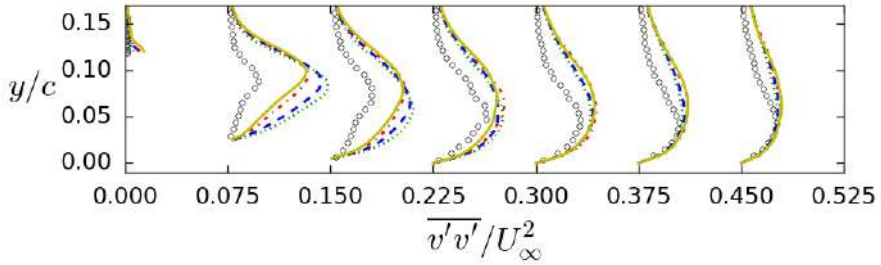

(c) *Wall-normal Reynolds stress profiles shifted by* $\Delta = 0.075$

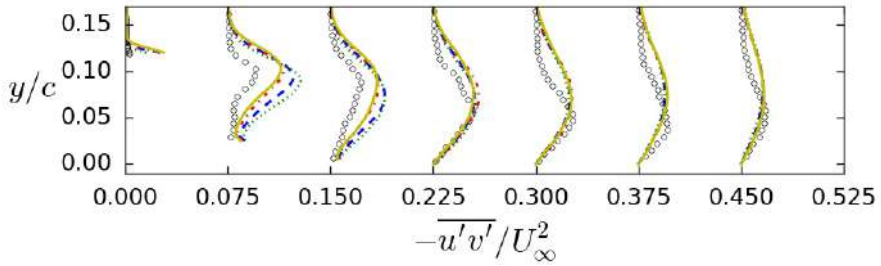

(d) *Shear Reynolds stress profiles shifted by* $\Delta = 0.075$

Figure 4.16: Grid G1: Influence of the point where the velocity is evaluated on the mean streamwise velocity and Reynolds stresses, at different streamwise positions: $x/c = 0.65, 0.8, 0.9, 1.0, 1.1, 1.2, 1.3$. Green dotted lines (·····): classical FE method, blue dashed lines (- - - -): exchange location at first grid point, red dash-dotted lines (-·-·-): exchange location at third grid point, yellow solid lines (——): exchange location at $y = 0.125\delta_{in}$, circles (○): experiment (Greenblatt et al. [142]).

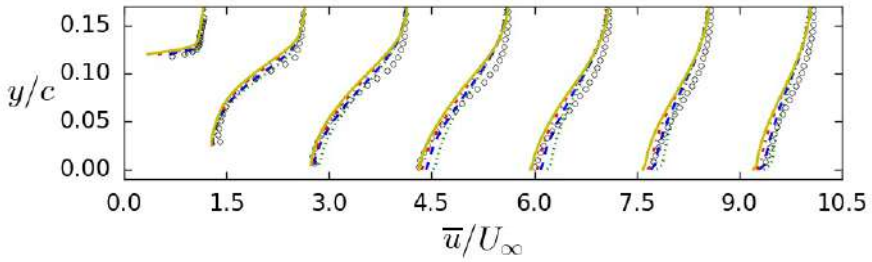

(a) *Mean streamwise velocity profiles shifted by* $\Delta = 1.5$

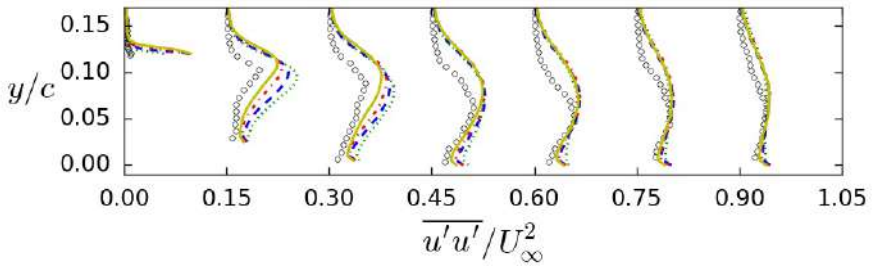

(b) *Streamwise Reynolds stress profiles shifted by* $\Delta = 0.15$

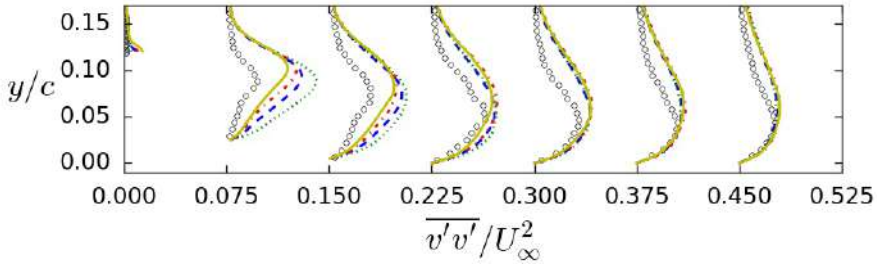

(c) *Wall-normal Reynolds stress profiles shifted by* $\Delta = 0.075$

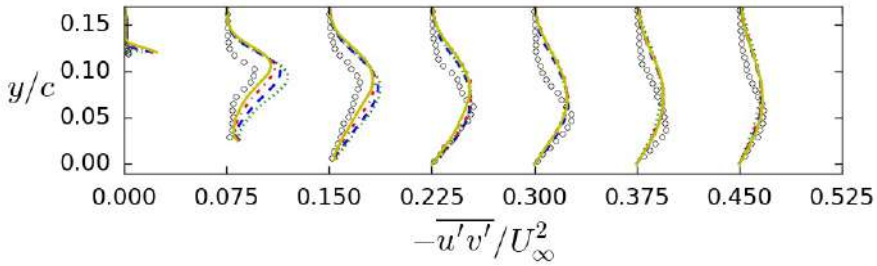

(d) *Shear Reynolds stress profiles shifted by* $\Delta = 0.075$

Figure 4.17: Grid G2: Influence of the point where the velocity is evaluated on the mean streamwise velocity and Reynolds stresses, at different streamwise positions: $x/c = 0.65, 0.8, 0.9, 1.0, 1.1, 1.2, 1.3$. Green dotted lines (·····): classical FE method, blue dashed lines (- - - -): exchange location at first grid point, red dash-dotted lines (-·-·-): exchange location at third grid point, yellow solid lines (——): exchange location at $y = 0.125\delta_{in}$, circles (○): experiment (Greenblatt et al. [142]).

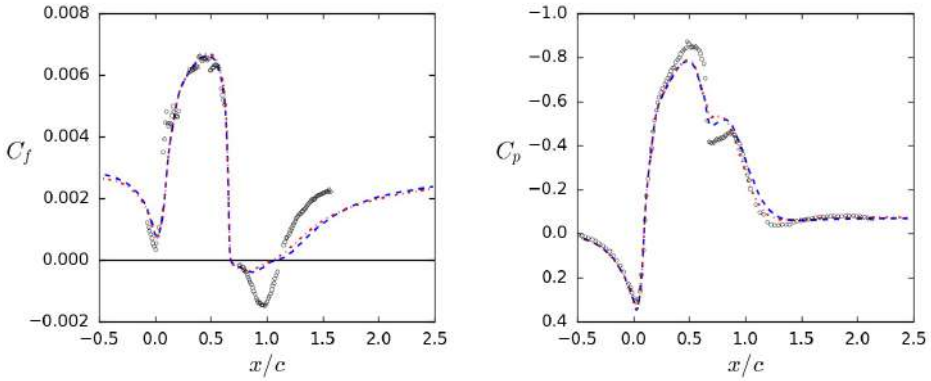

(a) *Skin friction coefficient* (b) *Pressure coefficient*

Figure 4.18: Influence of grid resolution on the skin friction (a) and pressure (b) coefficients across the streamwise direction (velocity evaluated at $y = 0.125\delta_{in}$). Red dash-dotted lines (-·-·-): coarse grid (G1), blue dashed linse (- - - -): fine grid (G2), circles (○): experiment (Greenblatt et al. [142]).

further away from the wall.

The influence of the grid resolution on the results is presented in Fig. 4.18-4.19, for the simulations where the velocity is evaluated at $y = 0.125\delta_{in}$. Although the differences in the skin friction and pressure coefficient are hardly noticeable at first glance (Fig. 4.18), it can be seen that refining the mesh improves the prediction of the reattachment location (Table 4.1). Minimal differences are also observed for the mean streamwise velocity (Fig. 4.19a); however there is a significant improvement in the prediction of the Reynolds stresses close to the center of the recirculation region (Fig. 4.19b-4.19d) as the mesh is refined.

4.2.8 Conclusions

The implementation of wall modelling used by the finite difference and finite volume communities has been adapted to finite elements. The new implementation is as simple and easy to implement as the classical finite element implementation but it provides vastly superior results. Instead of omitting a part of the domain and relying on the wall model to account for it, as is commonly done in finite elements, the whole domain is resolved and the wall stress at the wall is calculated using the velocity at the first grid point off the wall (or gauss point in the finite element context). The fact that this velocity is fully three-dimensional (as opposed to the classical finite element approach where the velocity used is imposed to be zero in the wall-normal direction) leads to significantly improved predictions. Specifically,

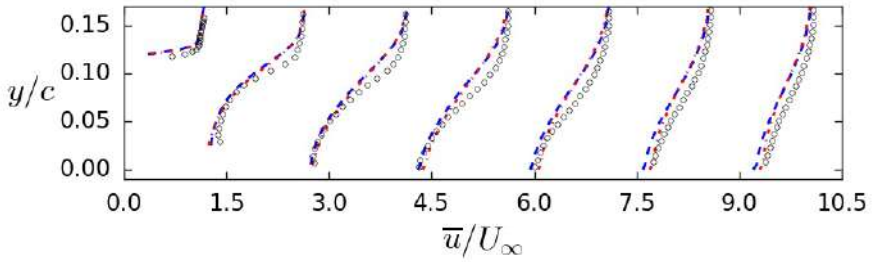

(a) *Mean streamwise velocity profiles shifted by* $\Delta = 1.5$

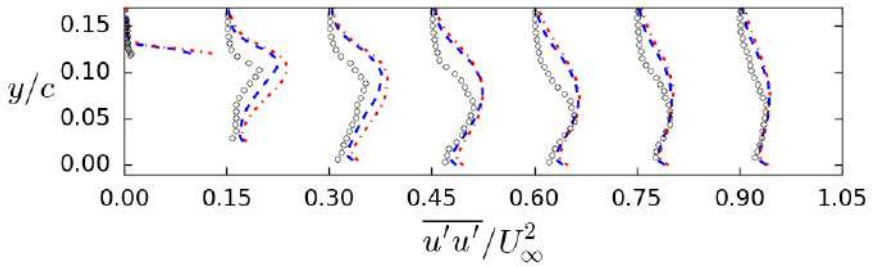

(b) *Streamwise Reynolds stress profiles shifted by* $\Delta = 0.15$

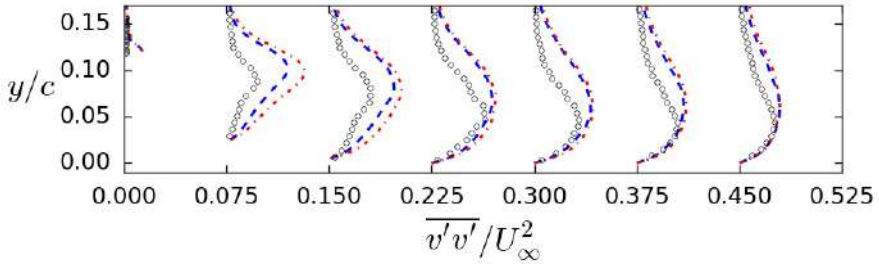

(c) *Wall-normal Reynolds stress profiles shifted by* $\Delta = 0.075$

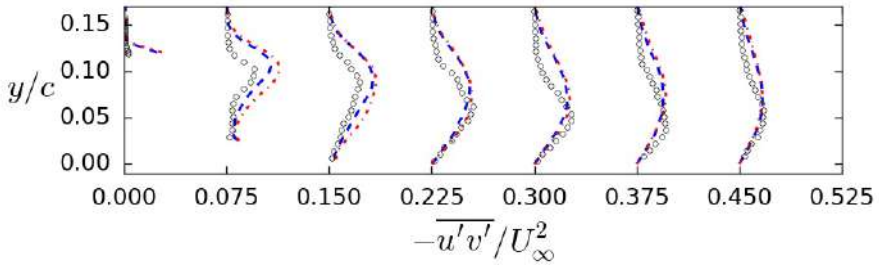

(d) *Shear Reynolds stress profiles shifted by* $\Delta = 0.075$

Figure 4.19: Influence of grid resolution on the mean streamwise velocity and Reynolds stresses (velocity evaluated at $y = 0.125\delta_{in}$), at different streamwise positions: $x/c = 0.65, 0.8, 0.9, 1.0, 1.1, 1.2, 1.3$. Red dash-dotted lines (-·-·-): coarse grid (G1), blue dashed lines (- - - -): fine grid (G2), circles (○): experiment (Greenblatt et al. [142]).

the presence of the resolved part of the stress $-\rho u_x' u_z'$ (cf. Eq. 4.1) leads to a significantly more accurate prediction for the velocity gradient, compared to the classical finite element method. The method is tested against the classical approach, in three different benchmark cases: a) the turbulent channel flow at $Re_\tau = 2003$, b) the atmospheric boundary layer flow, and c) the wall-mounted hump flow. In all cases, the improvement in the results is significant when using the new method, in particular for the mean streamwise velocity as well as the skin friction. It is interesting to note that the proposed method performs remarkably well, despite the fact that the meshes utilized were coarse, and a simple wall law was used as a wall model. This is especially true in the hump case, a non-equilibrium flow with features like separation and reattachment of the boundary layer that are typically difficult to capture.

Additionally, two possible remedies for the LLM have been tested. Taking the input velocity for the wall law further away from the wall and using the time averaged values of the velocity. For the atmospheric boundary layer flow, due to the very high Reynolds number, time averaging is needed not only to reduce the LLM but also to avoid divergence of the simulation due to the strong fluctuations. In the channel case, we have tested the effect of time averaging the input velocity of the wall model, as well as the effect of the point where this velocity in evaluated. In this work, we do not find a significant improvement by using time-averaged velocities as an input to the wall law. The advantage of using the exchange location approach over the classical finite difference approach is also subtle for this case. It is clear that both approaches are significantly better that the classical finite element approach based on the results obtained in this work and those available in the literature. In the atmospheric boundary layer and wall-mounted hump cases, time-averaged values have been used and only the influence of the point where we evaluate the input velocity for the wall model is examined. For these two cases it is clear that the classical finite element approach provides much poorer results than the finite difference approach for wall modelling. The exchange location provides the best results for both cases. In the hump case, we observe that taking the velocity further away from the wall provides noticeable improvements for the friction coefficient and the location of reattachment point.

4.3 Non-equilibrium model

4.3.1 Introduction

The concept of a two-layer non-equilibrium wall model was originally introduced by Balaras et al. in [144, 145], where they solved the thin boundary layer equations (TBLE) in an auxiliary grid, using a simple algebraic mix-

ing length model for turbulence closure. Their method consisted of feeding the LES velocity to the wall model at the first grid point off the wall, which then calculated the wall shear stress and passed it to the LES as a boundary condition at the wall. Using the same strategy on a backward-facing step, Cabot and Moin [146] found that due to the resolved Reynolds stresses carrying over from the LES to the wall model, the skin friction was overpredicted. To rectify that problem, they suggested a dynamic adjustment of the von Kárman constant in order to reduce the modelled Reynolds stress and, thus, counteract the excess resolved stresses. This approach was later used by Wang and Moin [147] on a flow over an airfoil trailing edge, with a notable improvement in the prediction of the skin friction.

Kawai and Larsson [148] noted that the assumption of a constant distribution of the von Kárman constant is not accurate in high Reynolds numbers, since the ratio between resolved and modelled Reynolds stresses varies along the wall-normal direction, due to the highly anisotropic meshes. Instead they suggested that the standard value of the von Kárman constant is to be used from the wall up to a certain height h_{crit}, where the auxiliary mesh is too anisotropic to support resolved stresses. From this height up to the matching interface, the von Kárman constant should follow a linear distribution instead. Additionally, they solved the full RANS equations in the auxiliary grid, in order to account for all the non-equilibrium phenomena. A downside of their approach lies in the fact that the model parameter that is used to specify h_{crit} depends on the numerical scheme as well as the mesh. With that in mind, Park and Moin [149] suggested a method that does not match the total stress in the wall model and the LES, but instead subtracts the resolved part of the stress from the RANS modelled part.

In this section, preliminary work on a two-layer non-equilibrium wall model is presented. The model solves the full unsteady RANS equations on an auxiliary grid. In order to circumvent the excess of Reynolds stresses, we apply a time-averaging technique on the information that the wall model receives from the LES, that filters the incoming stresses. The model is tested on the turbulent channel flow at $Re_\tau = 2003$. Furthermore, we investigate the use of auxiliary grids which are coarser in the tangential directions than the main grid.

4.3.2 Description of the model

Following the concept introduced in [144, 145], an auxiliary grid is utilized to calculate the wall stress based on the velocity coming from the LES mesh, Fig. 4.20. The auxiliary grid is typically, but not necessarily, generated from an extrusion of the wall surface mesh of the main simulation. The nodes are concentrated towards the wall in the wall-normal direction, following a geometric progression, so that the boundary layer is properly

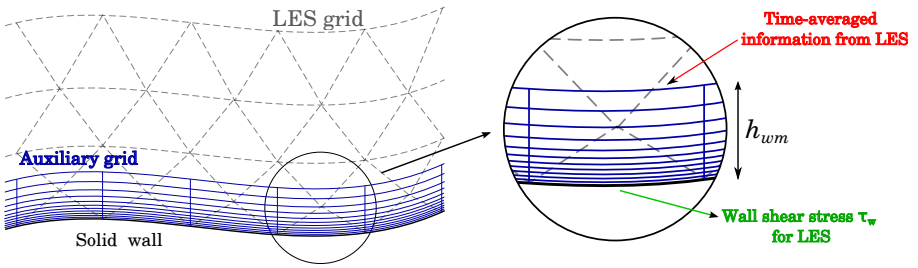

Figure 4.20: Sketch of the two-layer strategy.

resolved and the wall stress is accurately predicted.

The full, unsteady Reynolds-Averaged Navier Stokes (URANS) equations are solved in the auxiliary grid:

$$\partial_t \overline{\mathbf{u}} + \overline{\mathbf{u}} \cdot \nabla \overline{\mathbf{u}} - \nabla \cdot (2(\nu + \nu_t)\boldsymbol{\varepsilon}(\overline{\mathbf{u}})) + \nabla \overline{p} = \overline{\mathbf{f}} \tag{4.7}$$

where $\bar{}$ denotes time-averaged variables and ν_t is the turbulent eddy viscosity. An algebraic model based on Prandtl's mixing length hypothesis is used for turbulence closure:

$$\nu_t = (\kappa y)^2 \left|\boldsymbol{\varepsilon}(\overline{\mathbf{u}})\right| \left[1 - \exp\left(-\frac{y^+}{A^+}\right)\right]^2 \tag{4.8}$$

where the expression in the bracket is the Van-Driest wall-damping function. Here, the wall-damping constant is $A^+ = 26$. In order to avoid steep restrictions on the time-step size due to the CFL condition and the wall-normal refinement of the auxiliary grid, a first order implicit scheme is used for temporal discretization. Instead, both simulations utilize the time-step imposed by the CFL condition of the main (LES) simulation, as described in Section 2.3.

Instead of relying on the aforementioned remedies, a time-averaging procedure is utilized in order to explicitly filter out the incoming resolved Reynolds stresses from the LES mesh. The exponential running average method described in Section 4.2.4 is used here. The method has shown to be insensitive to the exact value of the averaging period T, providing it is large enough to properly filter the incoming stresses. For the turbulent channel flow examined here, T is set equal to 2 flow-through units, as in the case of the equilibrium model.

The auxiliary simulation receives the time-averaged velocity from the LES as a boundary condition at the matching interface. An alternative approach would involve using only the tangential components of the velocity along with the wall-normal traction as a boundary condition, however this is not possible with the current coupling structure available in Alya and was,

therefore, not examined. A no-slip condition is imposed at the wall boundary. In the remaining boundaries, the boundary conditions are set to match those of the main simulation. In the turbulent channel flow examined here for example, periodic conditions are imposed in the tangential directions. The wall stress calculated by the auxiliary simulation is then provided to the main simulation, which, along with a no-penetration condition, serve as wall boundary conditions.

4.3.3 Turbulent Channel Flow at $Re_\tau = 2003$

The turbulent channel flow case at $Re_\tau = 2003$ is used to evaluate the model. The reader is referred to Section 4.2.5 for basic information regarding this case. The effects of time-averaging the LES velocity, as well as the approach suggested by Kawai and Larsson [131], are evaluated on a 64^3 element mesh. The auxiliary grid is created by an extrusion of the LES surface grid at the wall boundaries. In the wall-normal direction, the first grid point is at $y^+ = 0.93$ with a growth rate of 1.1. For the case where the matching location is placed at the first grid point off the wall (in the LES mesh), this results on two auxiliary grids (one for each wall boundary) of $64 \times 21 \times 64$ elements, while when the matching location is moved to the third grid point, the size of the grids is $64 \times 32 \times 64$ elements. It is important to note that, unlike the equilibrium model, moving the matching location away from the wall incurs additional computational cost. Here, moving the matching location to the third grid point results in a 50% increase in the number of elements needed for the auxiliary grids.

The mean streamwise velocity for the cases with and without averaging can be seen in Fig. 4.21. The identifier "noav" is used to denote the cases without temporal averaging. It is immediately obvious that feeding the wall model with the unfiltered, instantaneous LES velocity results in an underprediction of the mean streamwise velocity. The problem becomes even more evident when the matching location is moved to the third grid point off the wall. Time-averaging the input velocity for the wall model massively improves the results. A cross-comparison of Fig. 4.21 and 4.3a shows that the results are comparable with those predicted by the equilibrium model. In fact, a small improvement can be observed for the case with the matching location at the first grid point off the wall, while the results are practically identical when the matching location is moved further away from the wall.

A finer LES grid with $256 \times 128 \times 128$ is also examined. Two types of auxiliary grids are utilized: one with the same resolution as the LES grid in the tangential directions (auxG1) and one with half the number of elements in each tangential direction (auxG2). In the wall-normal directions all grids have $y^+ = 0.93$ with a growth rate of 1.1, as in the coarse LES grid case. For the matching location at the first grid point, this results in

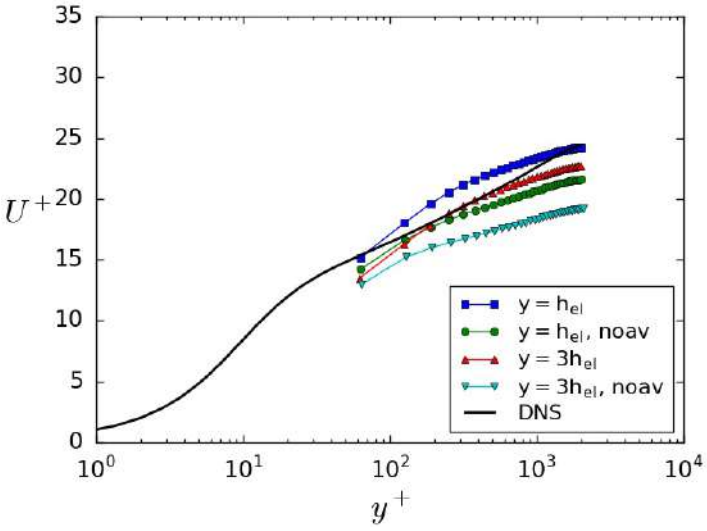

Figure 4.21: Mean streamwise velocity for the 64^3 mesh.

Grid	N_{elem} ($\times 10^6$)	Increase (%)
LES	4.2	-
auxG1a	0.98	23.3
auxG2a	0.25	6.0
auxG1b	1.64	39.0
auxG2b	0.41	9.8

Table 4.2: Non-equilibrium model. Number of elements for each auxiliary grid (for both boundaries), along with the increase in total number of elements.

resolutions of $256 \times 15 \times 128$ elements (grid auxG1a) and $128 \times 15 \times 64$ elements (grid auxG2a), while for the matching location at the third grid point, the resolutions are $256 \times 25 \times 128$ (grid auxG1b) and $128 \times 25 \times 64$ (grid auxG2b).

Fig. 4.22 shows the results for the velocity and its fluctuations for the fine grid. It can be seen that using coarser auxiliary grids has minimal impact on the results. This is an important result, as decreasing the resolution of the auxiliary grids significantly reduces the overhead of the model. This is consistent with the findings in [150, 151], although the author of these works used the thin boundary layer equations instead of a full RANS description. The number of elements for each grid (including both wall boundaries), as well as the increase in the total number of elements of each simulation is

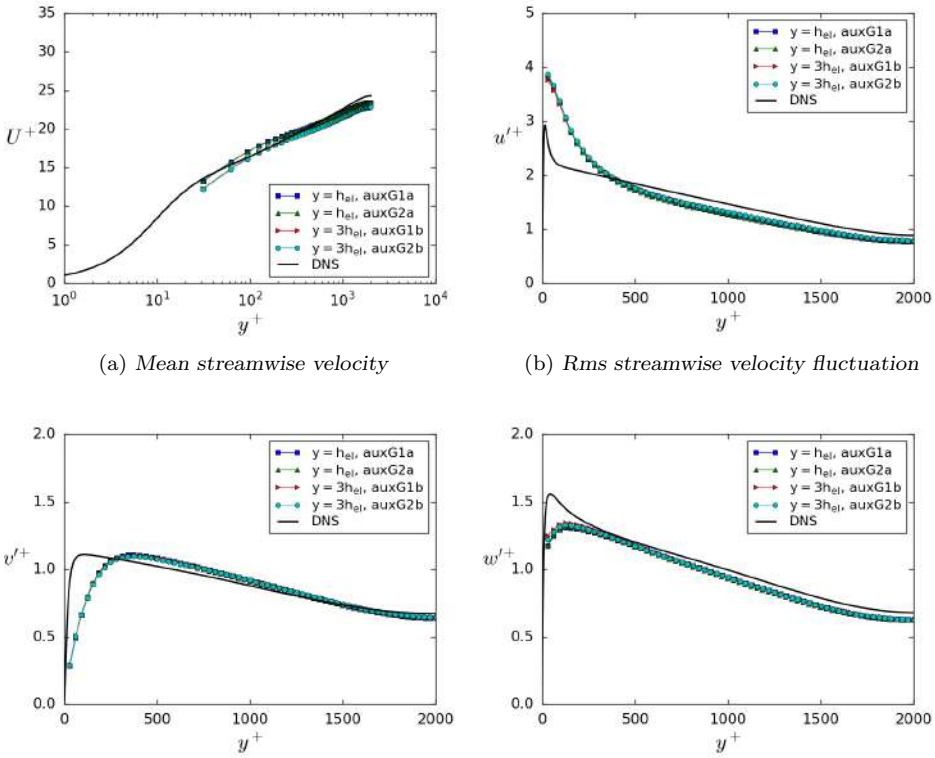

(a) *Mean streamwise velocity* (b) *Rms streamwise velocity fluctuation*

(c) *Rms wall-normal velocity fluctuation* (d) *Rms spanwise velocity fluctuation*

Figure 4.22: Mean streamwise velocity and rms velocity fluctuations for the fine grid.

given in Table 4.2. The coarser auxiliary grids amount to less than a 10% increase in the total number of nodes. Using coarser grids also means that the additional computational cost of placing the matching location at the third grid point becomes fairly negligible. One could potentially use even coarser grids, however not only would the resolution become too coarse, but also the communication costs would become dominant, negating any gains.

4.3.4 Conclusions

Preliminary work on a two-layer non-equilibrium wall model has been presented. The model solves the full unsteady RANS equations on an auxiliary grid, so that all the non-equilibrium phenomena are accounted for. The wall model receives the time-averaged LES velocity as an input. This temporal averaging explicitly filters the resolved Reynolds stresses, effectively solving a common problem encountered in two-layer models, where the excess of Reynolds stresses leads to an inaccurate prediction for the skin

friction. It is also observed that the auxiliary grid does not need to be an extrusion of the LES grid and can instead be coarser in the tangential directions. This results in significant savings in computational cost. The model is only tested on a turbulent channel flow at $Re_\tau = 2003$, however the results are promising.

Chapter 5

Real world applications

5.1 DrivAer

In this section we examine a realistic generic car model called the DrivAer body that has become widely accepted within the aerodynamics community. The model has been developed at the Technical University of Munich (TUM). The geometry is based on two medium saloons, the BMW 3 series and the Audi A4 and was created by merging CAD models in a collaboration between the Institute of Aerodynamics and Fluid Mechanics at TUM, the BMW Group and Audi AG. The model serves as an intermediate step between simplified car models such as the Ahmed body (Section. 2.5.2) and highly complex production vehicles. The model is modular allowing for up to 18 different configurations with the most important variation being the one regarding the geometry of the top. The three different geometries are Fastback, Estate and Notchback, pictured in Fig. 5.1. The A and B pillars are also illustrated for the Fastback model.

The model has been experimentally tested using a 40% scaled model [152, 153, 154, 155] at $Re = 4.87 \times 10^6$ at TUM. Cases with and without moving ground have been simulated taking advantage of the belted wind tunnel. There exist some small discrepancies between the values presented in the different works. To exemplify the differences we shall concentrate in the Fastback model with Smooth underbody, Mirrors and Wheels (F_S_wM_wW) with and without moving ground. The basic dimensions for the Fastback model can be seen in Fig. 5.2. For the case without ground simulation a 25% scaled model at Re from 0.75×10^6 to 2.8×10^6 has been tested at the wind tunnel in Technical University of Berlin (TUB) [156, 157]. Despite the lower Reynolds number in [156], a nearly independent behavior of the drag coefficient for Reynolds numbers above $Re = 2.25 \times 10^6$ is observed.

A lot of uncertainty exists for the exact setup in regards to the wheels in the experiments. For example, in the TUM experiments a generic wheel

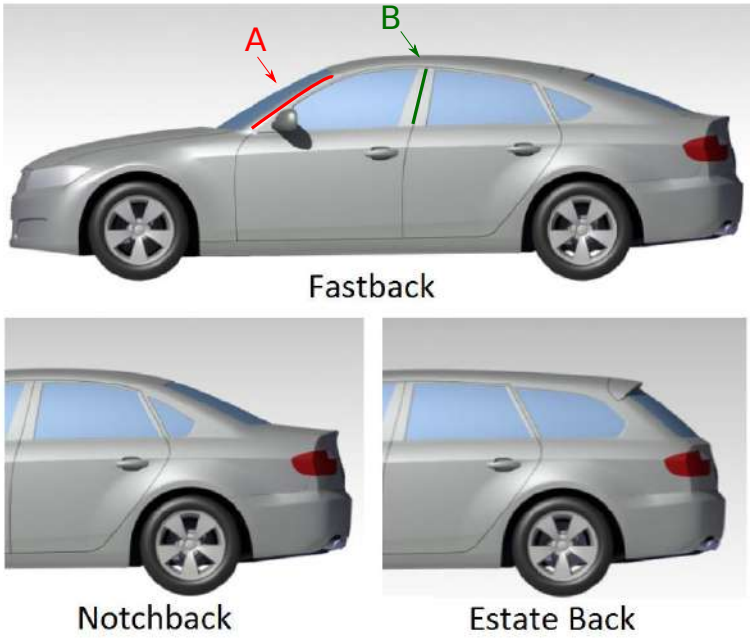

Figure 5.1: DrivAer. Different geometries for the top of the model.

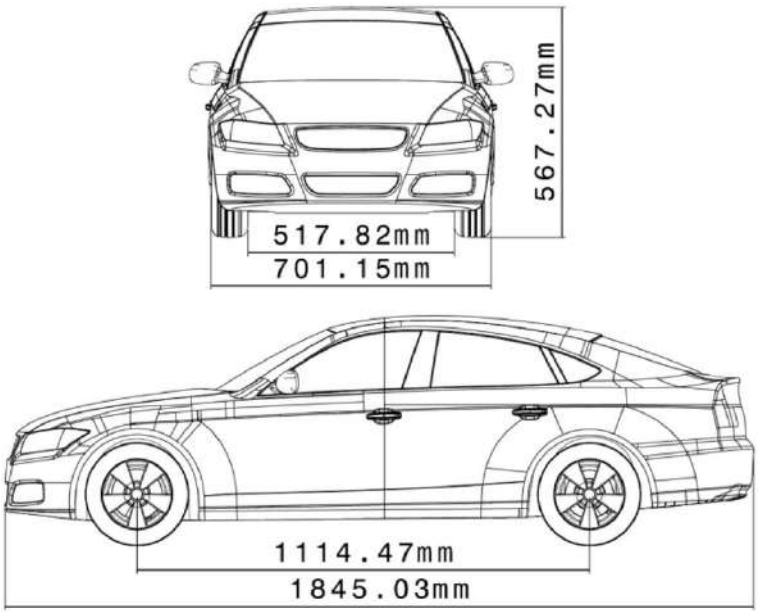

Figure 5.2: DrivAer. Dimensions of the Fastback configuration.

	w/o GS		w GS	
	C_D	C_L	C_D	C_L
Present LES	0.262	-0.111	0.265	-0.022
Heft [152]	0.261	0.01	0.265	-0.06
Heft [153]	0.254	n/a	0.243	n/a
Heft [154]	n/a	n/a	0.241	n/a
Mack [155]	0.249	n/a	0.247	n/a
Strangfeld [156]	0.249	0.057	n/a	n/a
Wieser [157]	0.258	-0.096	n/a	n/a

Table 5.1: DrivAer. Aerodynamic coefficients C_D and C_L for the Fastback configuration.

design has been used [155]. Furthermore it is not specified whether the wheel was in contact with the ground. In [156] it is specified that there exists a gap of 1.5 mm between the ground and the wheel and that the distance between the center of the wheel and ground is 83 mm. Since the radius of the DrivAer wheel model scaled to 25% is 79.625 mm it seems that some generic wheel must have been used. In [157] the gap between the wheel and the ground is also 1.5 mm but there is no information about the wheel diameter.

The reported aerodynamic coefficients for the cases with and without ground simulation are presented in Table 5.1. We notice the spread in values, even for experiments conducted in the same wind tunnel. For the experiments performed at TUM, the spread in the drag coefficient ranges from 0.016 to 0.012 for the cases with and without moving ground respectively. A difference of 0.009 is also observed in the experiments from TUB. Fewer results are available for the lift coefficient, but the spread here is significantly larger, making it impossible to determine the correct value.

Numerical studies using a large variety of turbulence models have also been performed on the DrivAer model. Most studies have performed RANS simulations (see for example [158, 159, 160, 161]), however there have also been studies using DES [159, 160, 161], as well as a study using both wall-resolved and wall-modelled LES [162].

In this work, the fastback geometry with smooth underbody, mirrors and both moving and fixed ground is simulated. The computational domain has a length of $10L$, a height of $8H$ and a width of $11W$, where L, H and W denote the length, height and width of the vehicle respectively. The vehicle is situated at $2L$ from the inlet boundary at the symmetry plane as shown in Fig. 5.3. A detail of the refinement zones is also included. The sizes used in the different zones are presented in Table 5.2. The resulting unstructured computational mesh consists of approximately 23 million degrees of freedom,

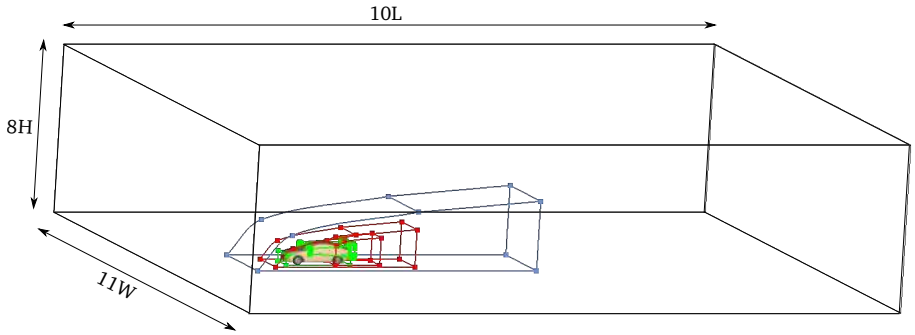

Figure 5.3: DrivAer. Computational domain and different refinement zones.

Refinement Zones	Max Surface Length mm	Max Volume Length mm
Green	10	20
Red	20	40
Blue	40	80

Table 5.2: DrivAer. Maximum element size for each refinement zone.

with a total of 84 million elements.

The Reynolds number, defined in terms of the vehicle length and the reference velocity, is $Re = 4.87 \times 10^6$, which requires the use of wall-modelled LES. The exchange location method presented in Section 4.2 has been used for the car and the ground, using Reichardt's law of the wall (Eq. 4.5). Slip boundary conditions have been used at the side and top boundaries. Finally, a turbulent inflow was originally tested, however it had minimal impact on the results. Therefore, a uniform velocity $(u, v, w) = (U_{\text{ref}}, 0, 0)$ is imposed at the inlet. This is consistent with the DES and LES studies found in the literature [159, 160, 161, 162, 163, 164].

The predicted aerodynamic coefficients are presented in Table 5.1. The predictions are in good agreement with the experimental data, apart from the lift coefficient for the case without moving ground. However, as explained previously, the large spread in experimental data means the correct value is not known. Nevertheless, we observe a reduction of the lift coefficient when the ground is moving, which is consistent with the findings in [152, 160].

The predictions for the pressure coefficient $C_p = ((p - p_{\text{ref}})/0.5\rho U_{\text{ref}}^2)$ along the top and the bottom of the car geometry in the symmetry plane for the case without ground simulation are presented in Fig. 5.4. The pressure increases as the flow travels along the bonnet of the car, before a sudden pressure drop is observed denoting the recirculation region occurring at the

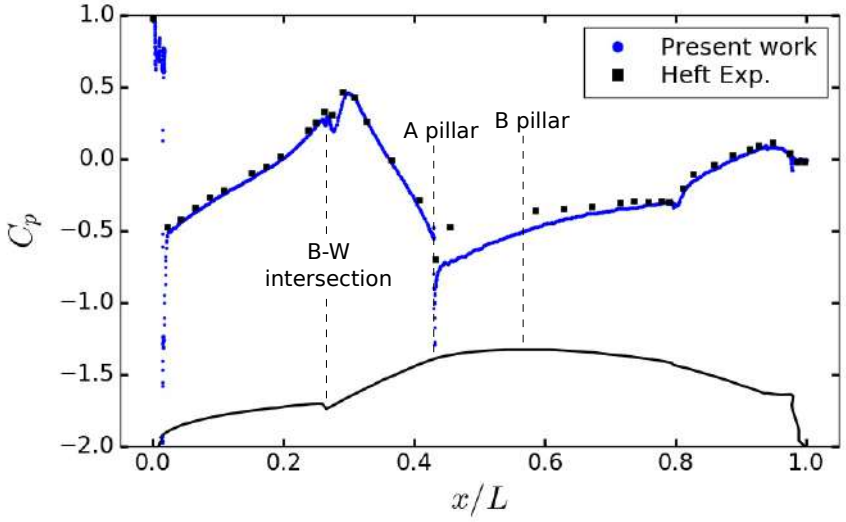

(a)

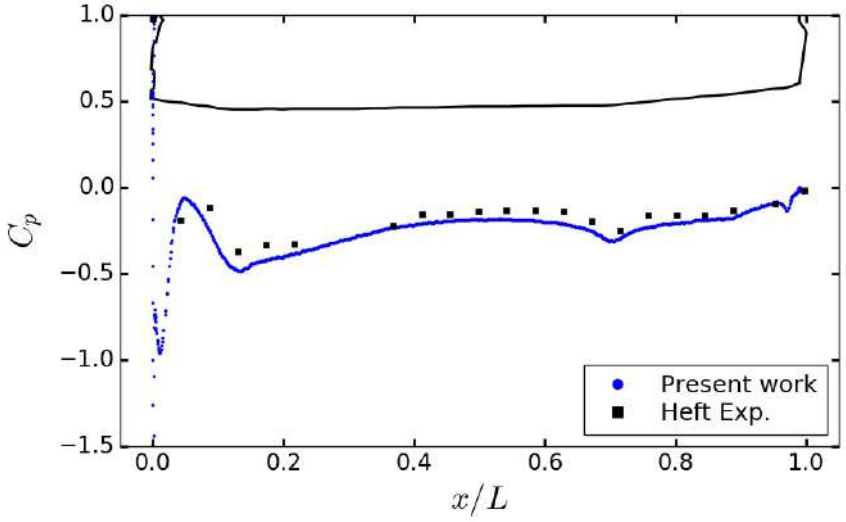

(b)

Figure 5.4: DrivAer. Average pressure coefficient along the (a) top and (b) bottom of the car geometry in the symmetry plane for the case without ground simulation. Comparison with the experimental results of Heft [152].

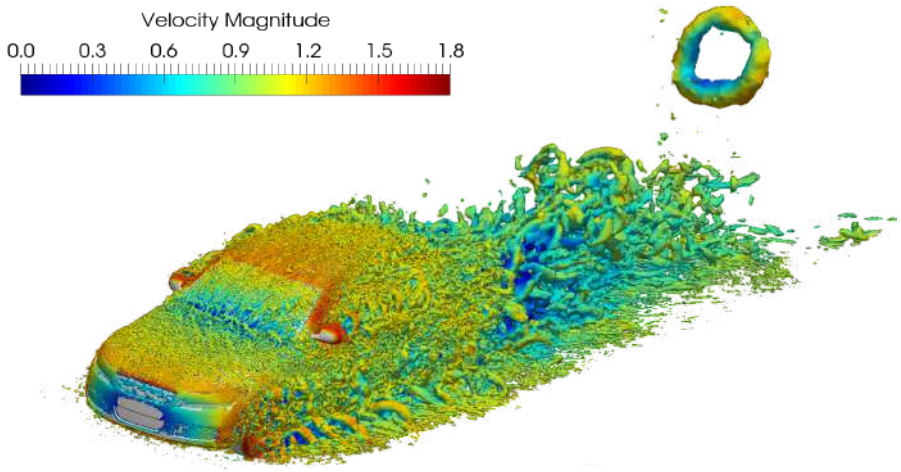

Figure 5.5: DrivAer. Q-criterion for the vorticity coloured by the velocity magnitude for the fastback model with rotating wheels.

intersection between the bonnet and the windshield (Fig. 5.4a). Following reattachment, the flow accelerates over the windshield resulting in a decrease in pressure. The biggest deviation from the experiment is observed at the top of the A pillar. Peters et al. [158] suggested that this could be due to the absence of the roof stinger in the geometry used in the simulations, along with other discrepancies between the geometries used in the numerical simulations and the experiments. The overshoots observed at this point, as well as the front bumper lip of the car, are consistent with the behavior noticed in other LES and DES studies (cf. for example [160, 162]). The predictions are in good agreement with the experiments in the region between the B pillar and the rear of the car. Looking at the underbody of the car (Fig. 5.4b), the biggest deviation from the experiments is observed at $x/L \approx 0.1$, which is where the front wheels are located. We notice that the pressure coefficient is negative across the length of the underbody, which acts as a diffuser, generating a downforce that pushes the vehicle to the ground, increasing traction.

In Figure 5.5, vortices identified by means of Q-isosurfaces and coloured by the velocity magnitude for the fastback case with rotating wheels are presented. As expected a much more complex behavior is observed, compared to the Ahmed body 2.15. Large structures are created when the incoming flow interacts with the wheels and the mirrors. These structures appear to be dominant in the wake of the car. The generation of some smaller vortical structures can also be observed at the intersection between the bonnet and the windshield, as well as when the flow interacts with the A pillar of the car.

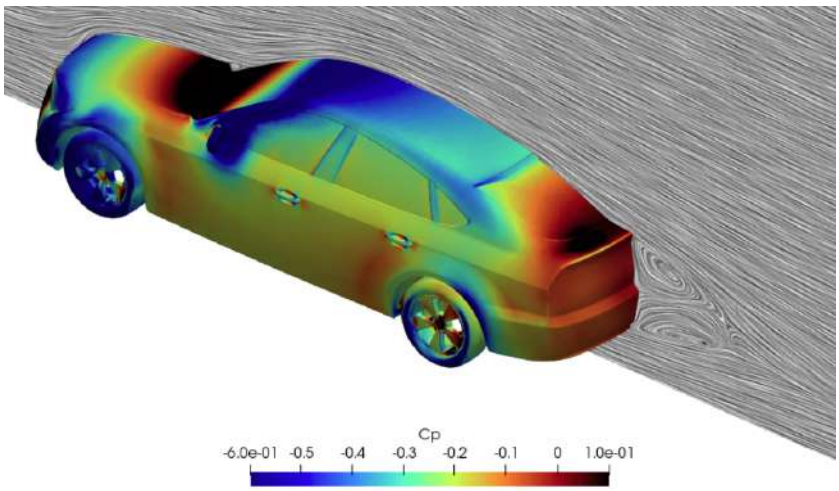

Figure 5.6: DrivAer. Pressure coefficient and line integral convolution on the symmetry plane for the average flow.

Figure 5.7: DrivAer. Streamlines for the average flow.

Figure 5.6 combines the pressure coefficient over the car body with the

Figure 5.8: The Bolund peninsula viewed from a meteorological mast south of the site.

streamlines for the mean flow for the fastback DrivAer model in the case without moving ground. The flow pattern in the symmetry plane compares well with the experimental results from [156], with the lower vortex (the one originating from the underbody) being slightly thinner in the present work. A possible explanation could be the different wheel size and geometry used. Some differences can be observed in the pressure coefficient towards the end of the trunk lid, however there is a good qualitative agreement with the experimental results from [156, 157]. Finally, the streamlines for the mean flow at the car rear are shown in Figure 5.7. A good match with the experimental surface visualization presented in [157] is obtained.

5.2 Flow over the Bolund hill

In this Section we examine the features of the flow over the Bolund hill. The Bolund hill is a 12m high, 130m long and 75m wide hill located on a peninsula close to the city of Roskilde, Denmark. A narrow isthmus connects the hill to the main land at the east side, while the rest of the hill is surrounded by sea, Fig. 5.8. Its highly three-dimensional geometry (Fig. 5.9), featuring properties such as a steep vertical upstream escarpment, similar to those of complex terrains with wind farm installations, as well as a sharp change in surface roughness (from water to grass), make the flow challenging to simulate and, therefore, an excellent case for validating computational models. In addition, the incoming wind can be considered horizontally homogeneous, since there exists a long fetch of sea upstream of the hill, making it easier to establish proper inflow conditions. The hill's low height means it is not exactly representative of actual wind farm sites, however it allows to neglect thermal and Coriolis effects. Nevertheless, the shape of the hill represents a scaled-down model of a typical wind farm site.

The field data were collected during a measurement campaign performed during the winter of 2007-2008 [165]. Velocity and turbulence data were col-

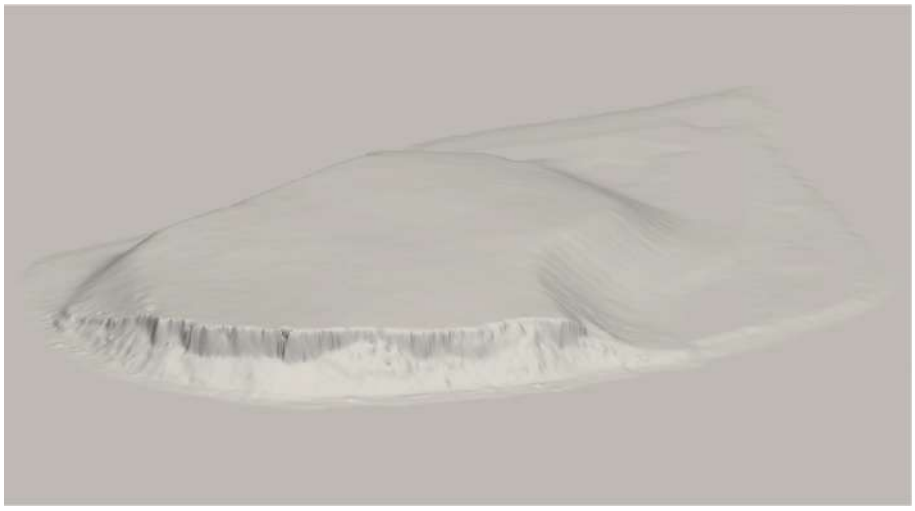

Figure 5.9: Closer look at the Bolund hill model geometry.

lected from anemometers distributed on 10 masts, positioned as presented in Fig. 5.10. Note that masts M0 and M9 were "control" masts for measuring the incoming wind conditions. An extensive comparison between various RANS and LES models was presented in [166], where the LES models were seen to have shown large speed-up errors offering worse results than the RANS ones. More LES studies have been conducted since [104, 167, 168], with significantly improved predictions. Namely, Chaudhari et al. [168] presented results from their LES studies that offered a noticeable reduction of the speed-up errors compared to the best published RANS results (Prospathopoulos et al. [169]), albeit using a quite fine mesh.

The present work focuses on the case where the wind comes from the west (angle 270°), which corresponds to case 1 in [166]. A mesh with local resolution ranging from 0.3m at the vertical escarpment, 0.7m at the hill region and 4m at the rest of the sea and coast surfaces has been used. This corresponds to an unstructured grid of approximately 27 million elements (tetrahedral and prisms) and only 6 million degrees of freedom. A detail of the mesh at the vertical escarpment zone and the transition between that zone and the hill is presented in Fig. 5.11 and Fig. 5.12 respectively. While this mesh resolution is finer in comparison to the LES studies presented in [166], it is notably coarser than more recent works, such as [168], where a mesh of 30 million degrees of freedom was used. The goal is to use a resolution that offers a reasonable compromise between accuracy and computational cost. It is estimated in [165] that for the Bolund case $Re_h = U_{\text{ref}} h/\nu \approx 10^7$, where $U_{\text{ref}} \approx 10$ ms^{-1} is the wind velocity at a height of 10 m. The kinematic viscosity was set to $\nu \approx 1.4 \times 10^{-5}$ kg m^{-1}s^{-1}, following the recommendation of [166].

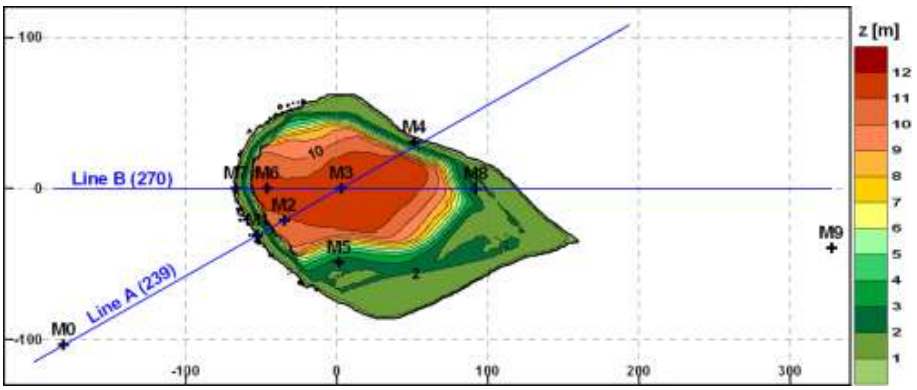

Figure 5.10: The Bolund hill topography coloured with height. Red dots denote the positions of masts M0-M9 installed during the field experiment.

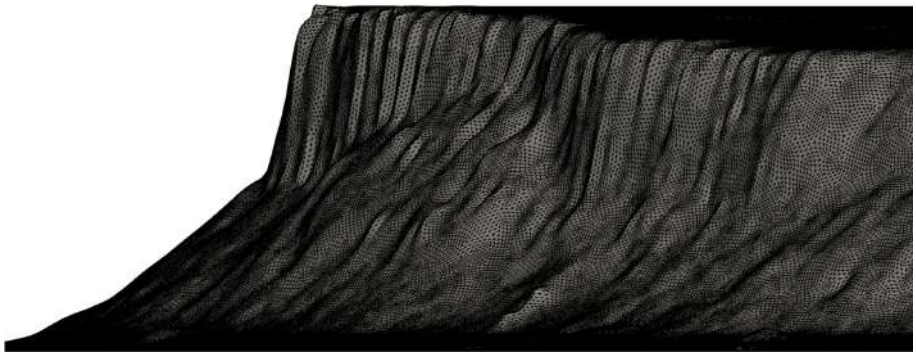

Figure 5.11: Detail of the Bolund hill surface mesh at the steeper vertical escarpment zone.

Since the mesh is quite coarse for such a high Reynolds number, the need for wall modelling arises. To that end, we employ the exchange location method presented in Section 4.2, with a simple logarithmic wall law for rough walls (Eq. 4.6). Additionally, for the generation of appropriate inflow conditions, we use both the precursor and synthetic methods presented in Chapter 3. For the latter, following the recommendations of [166], we impose a logarithmic velocity profile:

$$S = \frac{u_{*0}}{\kappa} log\left(1 + \frac{z}{z_0}\right)$$

where $\kappa = 0.4$ is the von-Kárman constant, $z_0 = 0.0003$ m is the roughness length over the water and $u_{*0} = 0.4$ ms^{-1} is the reference friction velocity. The fluctuations are imposed in such a way so that the turbulent kinetic

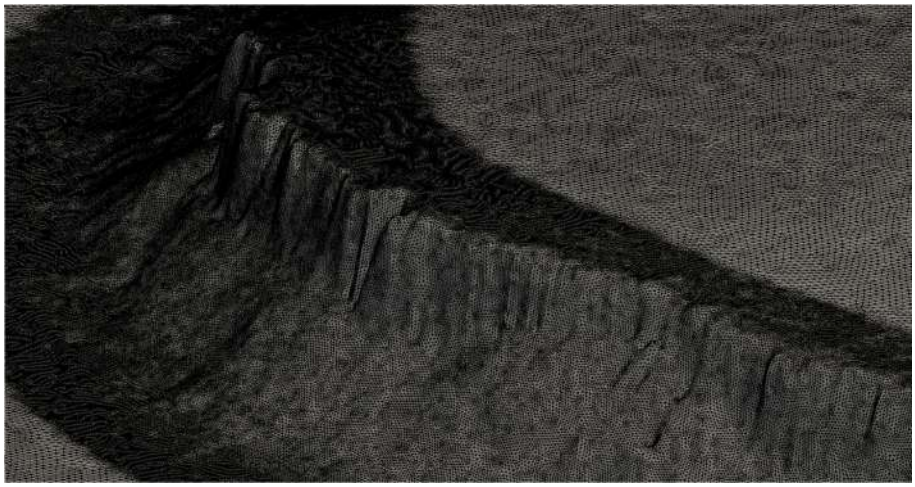

Figure 5.12: Detail of the Bolund hill surface mesh at the transition between the steeper vertical escarpment zone and the hill.

energy remains constant along the height z:

$$\frac{k}{u_{*0}^2} = 5.8.$$

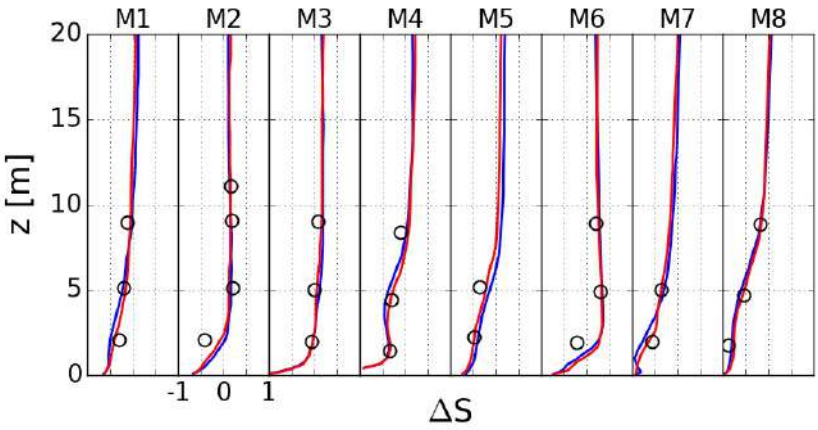

Figure 5.13: Bolund hill. Vertical profiles of the velocity speed-up ΔS at the masts M1-M8. Red line (——): precursor inlet, blue line (——): synthetic inlet, circle (○): field data.

Let us define the velocity speed-up ΔS as:

$$\Delta S = \frac{S - S_0}{S_0}$$

where S is the simulated or measured mean wind speed and S_0 is the mean wind speed at the reference mast M0. Fig. 5.13 presents the vertical profiles of the velocity speed-up at masts M1-M8, using both inflow methods, compared to the field data. It can be seen that both LES configurations offer a quite accurate prediction of the speed-up, with good agreement with the field data. The error is noticeably higher at the lower heights of masts M2 and M6, which is consistent with the observations from [166] and [168]. The explanation given is that there exists an intermittent flow separation close to the surfaces, which most models struggle to predict. It is also important to note that the two inflow methods offer predictions of similar quality, with the results from the precursor method being slightly more accurate. However, it can be argued that the improvement is not significant enough to justify the additional computational cost.

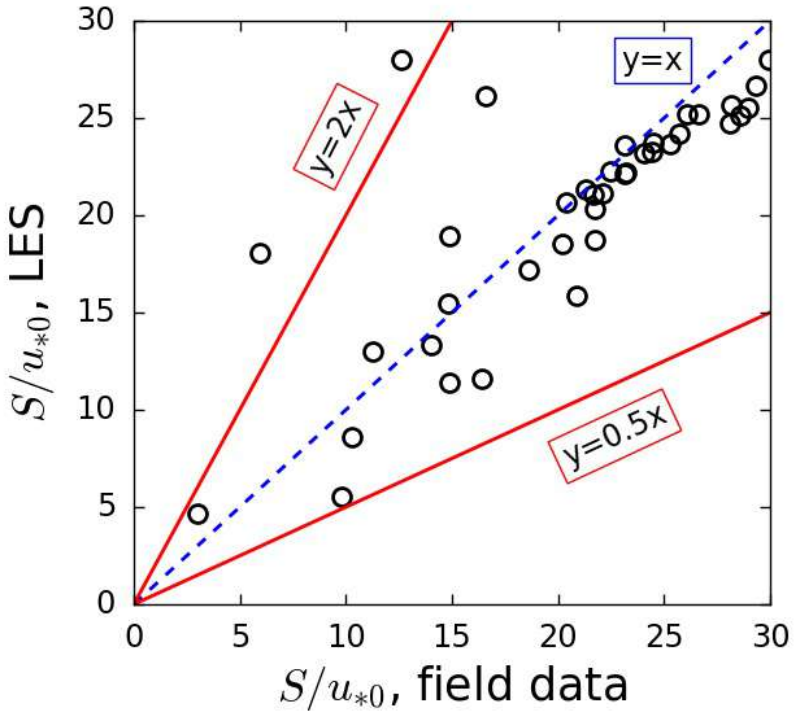

Figure 5.14: Bolund hill. Scatter plot of the velocity magnitude S at all the mast locations using the synthetic inflow conditions, normalized by the friction velocity at mast M0.

Fig. 5.14 presents a comparison of the mean velocity between the LES (using the synthetic inflow method) and the field data at all the mast locations in the form of a scatter plot. The overall agreement is very good, with

most of the points lying on the diagonal $y = x$, especially for the higher velocities. More discrepancies are observed for low velocities, which is to be expected since they are in locations close to the more geometrically complex parts of the hill. Notably, most of the samples lie inside the confidence area $0.5 \leq P/O \leq 2$, where P is the predicted and O the observed value. Using the FAC2 (fraction of two) validation metric, that denotes the amount of data that satisfy the above condition, we obtain FAC2 = 0.94, which is very close to the ideal (FAC2 = 1) and is considered very high for environmental simulations.

The mean absolute speed-up error for all measurement locations, defined in [166] as:

$$R_S = 100\,(\Delta S_s - \Delta S_m)$$

where the subscripts s and m are the simulated and measured speed-up respectively, is presented in Table 5.3, with results from the present study being compared with results from the literature [166, 104, 167, 168, 169, 170, 171]. It can be seen that the results from the current work compare well against all the available data, with only the results of Chaudhari et al. [168] offering a better prediction. As mentioned before, the mesh used here is much coarser than the one in [168], therefore this behavior is to be expected. It is important to note, however, that the improvement compared with the RANS results of Prospathopoulos et al. [169], as well as the RANS results from Alya (not presented here), is not very significant, despite the additional computational cost. In fact, it can be argued that the uncertainty of the hill geometry used in numerical simulations [172] might have a bigger effect on the accuracy of the results than the turbulence model.

Instantaneous vorticity iso-contours are depicted for the synthetic inlet in Fig. 5.15. A horse-shoe vortex structure can be identified around the frontal part of the Bolund hill. This vortex breaks down into hairpin-like small scale vortices which are mixed downstream with the upcoming ABL streaks generating a turbulent region in the wake of the Bolund hill. Additionally, another system of turbulent instability generation is observed at the initial part of the hill, where a separation of the boundary layer is found leading to a further reattachment, thus increasing the turbulent mixing by shedding hairpin-like structures into the wake of the hill.

Model type	R_S	References
RANS - 2eq	15.1 (11.4)	Bechmann et al. [166]
LES	17.3 (14.1)	Bechmann et al. [166]
Wind tunnel	14.7 (13.3)	Bechmann et al. [166]
RANS - 2eq	10.3	Prospathopoulos et al. [169]
Wind tunnel	17 (13.9)	Yeow et al. [170]
LES	10.9	Vuorinen et al. [167]
Wind tunnel	12	Conan et al. [171]
LES	11	Conan et al. [171]
LES	8.8	Chaudhari et al. [168]
LES - precursor	10.17	**Present work**
LES - synthetic	10.17	**Present work**

Table 5.3: Bolund hill. Mean absolute speed-up errors R_S (in %) for all measurement locations for the 270° wind direction, compared with results from the literature. The values in brackets show the best performances of the model.

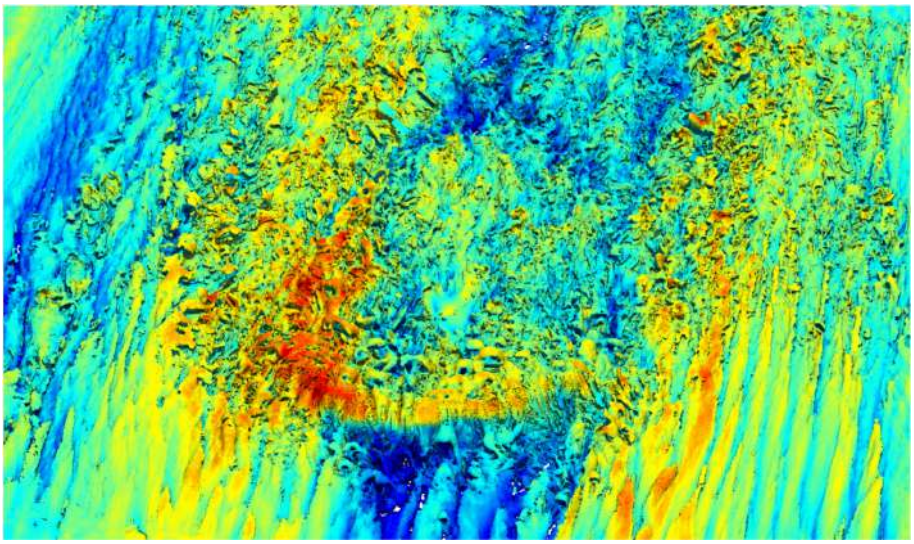

Figure 5.15: Bolund hill. Vortical structures coloured by the wind velocity magnitude.

Chapter 6

Conclusions and future work

6.1 Conclusions

This thesis studies the development of a complete Large Eddy Simulation framework within the Finite Element method. This includes a new low-dissipation formulation, a comparison between synthetic and precursor methods for the generation of turbulent inflows, a new method for applying wall models and a simple method that solves the excess of Reynold stresses, a common problem in two-layer non-equilibrium wall models.

The new formulation uses a non-incremental fractional step method to stabilize the pressure and allow for equal order interpolations for velocity and pressure. Temporal discretization is performed through an explicit energy-conserving Runge-Kutta scheme with an eigenvalue-based time step estimator. The final scheme preserves momentum and angular momentum, with the error in the conservation of kinetic energy being of $\mathcal{O}(\delta t, h^2)$ for linear finite elements (coinciding with the error obtained for finite volumes using collocated schemes). Explicit subgrid scale models are used for turbulence closure. This new formulation is compared with the Variational Multiscale (VMS) method, commonly used for (implicit) large eddy simulations in finite elements, in a range of benchmark tests: a) Decaying Isotropic Turbulence, b) Taylor-Green Vortex and c) Turbulent Channel flow at $Re_\tau = 395,\ 950$ and 2003. It is shown that, while for the VMS method the best configuration of the stabilization parameters is problem dependent, the new formulation performs very well without the need for ad hoc tuning. The formulation is further tested on a flow over a sphere, as well as the Ahmed car body. The results are in great agreement with the reference data, further showcasing the suitability of the formulation for large eddy simulations for complex geometries and high Reynolds numbers.

The importance of prescribing appropriate inflow conditions is also highlighted. Imposing a laminar inlet is shown to falter, significantly underpredicting fluctuations, apart from regions where the turbulence is generated

by the geometry (e.g. the wake of a three-dimensional hill). An extensive review on techniques of synthesizing turbulence is performed, and a method where turbulence is generated through the diffusion process is selected, because of the simplicity of its implementation in a CFD code and the fact that it can easily be applied to arbitrary geometries and unstructured grids. The method is compared with the precursor method on a flow over a three-dimensional hill. The effect of introducing periodicity in the precursor inlet is also examined, but is found to have minimal effect in the results. All methods offer very accurate predictions, in good agreement with the experimental data. The precursor method performs slightly better, however the difference is quite small and it is argued that it does not justify the significant overhead in terms of computational cost. Similar conclusions are drawn from the case of the flow over the Bolund hill. Thus, the synthetic method is instead preferred in the rest of the cases presented in this work.

Furthermore, considering the significant computational cost of resolving the near-wall region, wall modelling techniques are investigated. Mainly, the way that equilibrium models are commonly applied in finite elements is investigated. The implementation typically used in the finite difference and finite volume communities is adapted to finite elements. Instead of using a "lifted wall" approach, where part of the domain is omitted with the wall model accounting for it, as is commonly done in finite elements, the mesh formally extends all the way to the wall and the whole domain is resolved. It is seen that evaluating the input velocity further away from the wall and not at the first grid point yields superior results. The method is tested in three different cases: a) Turbulent channel flow at $Re_\tau = 2003$, b) Neutrally stratified atmospheric boundary layer and c) Wall-mounted hump. The new method performs remarkably better than the classical finite element approach in all cases. Additionally, preliminary work on a two-layer non-equilibrium wall model is presented. Instead of the more complicated procedures presented in the literature, the model relies on temporal averaging of the input velocity in order to filter the excess Reynolds stresses and solve a common problem of non-equilibrium models. The method is tested in the turbulent channel flow case at $Re_\tau = 2003$ with great results. It is also seen that the auxiliary grid does not need to be an extrusion of the LES mesh, but can instead be coarser in the tangential directions.

Finally, the complete framework is used in the large eddy simulation of real world applications with complex geometries, namely the DrivAer model, a realistic car model based on the Audi A4 and BMW 3 geometries, as well as the flow over the Bolund hill, a hill with complex geometry that resembles a scaled-down model of actual wind farm sites. The predictions are in very good agreement with experimental and field data in both cases, highlighting the great potential of the methods presented.

6.2 Future work

Following the work presented in this thesis, there are open lines of research that can be investigated in order to extend the applicability of the framework and potentially improve its accuracy, mostly within the wall-modelled LES context.

- **Non-equilibrium wall model**
  Following the preliminary work presented in Section 4.3, the two-layer non-equilibrium wall model needs to be evaluated in complex cases. The main goal is to ensure that time-filtering the input variables is sufficient to solve the excess of Reynolds stress that lead to inaccuracies in the skin friction predictions, without the need for additional remedies. Furthermore, the effect of coarsening the tangential resolution of the auxiliary grid needs to be examined, in order to evaluate the computational cost imposed by the wall model, compared to a simpler equilibrium one. Finally, the use of more complex RANS models in the auxiliary simulation needs to be investigated. For instance, the potential of creating a wall model that can predict transition to turbulence, via the use of an appropriate model such as the $\gamma - Re_\theta$ transition model, can be examined.

- **Mixed wall modelling method**
  A method which combines the use of equilibrium and non-equilibrium models in different regions of the flow can be devised. Instead of using the non-equilibrium model throughout the computational domain, the auxiliary grid can be restricted in regions with a notable non-equilibrium behavior of the flow, with an equilibrium model used in the rest of the domain. Although such a method would require an a priori knowledge of the flow and could be difficult to implement, it can potentially provide results of great accuracy, without imposing a significant overhead in terms of computational cost.

- **High-order finite elements**
  The application of high-order finite elements has mostly been restricted to simple flows, with more complex geometries examined only recently. However, to the author's knowledge, very little work has been conducted in performing wall-modelled LES with high-order elements. This line of research can potentially offer very accurate methods and should be explored. It must be noted, however, that high order mesh generation is fairly limited in commercial meshing software.

Bibliography

[1] A. Leonard. Energy cascade in large-eddy simulations of turbulent fluid flows. *Advances in Geophysics*, 18A:237–248, 1974.

[2] J. Smagorinsky. General circulation experiments with the primitive equations, Part 1: the basic experiment. *Monthly Weather Review*, 91:99–164, 1963.

[3] M. Germano, U. Piomelli, P. Moin, and W. Cabot. A dynamic subgrid-scale eddy viscosity model. *Physics of Fluids A*, 3(7):1760–1765, 1991.

[4] D. K. Lilly. A proposed modification of the Germano subgrid-scale closure method. *Physics of Fluids A*, 4(3):633–635, 1992.

[5] C. Meneveau, T. Lund, and W. Cabot. A Lagrangian dynamic subgrid-scale model of turbulence. *Journal of Fluid Mehcanics*, 224:353–385, 1996.

[6] P. Sagaut. *Large eddy simulation for incompressible flows - An introduction.* Springer, 3rd edition, 2006.

[7] S. B. Pope. *Turbulent flows.* Cambridge University Press, Cambridge, 2000.

[8] A. W. Vreman. An eddy-viscosity subgrid-scale model for turbulent shear flow: Algebraic theory and applications. *Physics of Fluids*, 16(10):3670–3681, 2004.

[9] J. P. Boris, F. F. Grinstein, E.S. Oran, and R. L. Kolbe. New insights into large-eddy simulation. *Fluid Dynamics Research*, 10:199–228, 1992.

[10] F. Grinstein, L. Margolin, and W. Rider. *Implicit large eddy simulation: computing turbulent fluid dynamics.* Cambridge University Press, Cambridge, 2007.

[11] T. J. R. Hughes. Multiscale phenomena: Green's functions, the Dirichlet-to-Neumann formulation, subgrid scale models, bubbles and

the origins of stabilized methods. *Computer Methods in Applied Mechanics and Engineering*, 127(1–4):387–401, 1995.

[12] T. J. R. Hughes, G. R. Feijóo, L. Mazzei, and J. B. Quincy. The variational multiscale method - a paradigm for computational mechanics. *Computer Methods in Applied Mechanics and Engineering*, 166(1–2):3–24, 1998.

[13] T. J. R. Hughes, L. Mazzei, and K. E. Jansen. Large eddy simulation and the variational multiscale method. *Computing and Visualization in Science*, 33:47–59, 2000.

[14] T. J. R. Hughes, L. Mazzei, A. A. Oberai, and A. A. Wray. The multiscale formulation of large eddy simulation: Decay of homogeneous isotropic turbulence. *Physics of Fluids*, 13(2):505–512, 2001.

[15] T. J. R. Hughes, A. A. Oberai, and L. Mazzei. Large eddy simulation of turbulent channel flows by the variational multiscale method. *Physics of Fluids*, 13(6):1784–1799, 2001.

[16] A. A. Oberai and T. J. R. Hughes. The variational multiscale formulation of LES: Channel flow at $re_\tau = 590$. In *40th AIAA Aerospace Sciences Meeting and Exhibit*, Reno, USA, 2002.

[17] J. Holmen, T. J. R. Hughes, A. A. Oberai, and G. N. Wells. Sensitivity of the scale partition for variational multiscale les of channel flow. *Physics of Fluids*, 16(3):824–827, 2004.

[18] T. J. R. Hughes, G. N. Wells, and A. A. Wray. Energy transfers and spectral eddy viscosity in large-eddy simulations of homogeneous isotropic turbulence: Comparison of dynamic Smagorinsky and multiscale models over a range of discretizations. *Physics of Fluids*, 16:4044–4052, 2004.

[19] S. S. Collis. Monitoring unresolved scales in multiscale turbulence modeling. *Physics of Fluids*, 13:1800–1806, 2001.

[20] V. Gravemeier. *The variational multiscale method for laminar and turbulent incompressible flow*. PhD thesis, University of Stuttgart, 2003.

[21] B. Koobus and C. Farhat. A variational multiscale method for the large eddy simulation of compressible turbulent flows on unstructured meshesapplication to vortex shedding. *Computer Methods in Applied Mechanics and Enginneering*, 193:1367–1383, 2004.

[22] C. Farhat, A. Rajasekharan, and B. Koobus. A dynamic variational multiscale method for large eddy simulations on unstructured meshes.

Computer Methods in Applied Mechanics and Enginneering, 195:1667–1691, 2006.

[23] V. Gravemeier. The variational multiscale method for laminar and turbulent flow. *Archives of Computational Methods in Engineering*, 13(2):249–324, 2006.

[24] R. Codina. Stabilized finite element approximation of transient incompressible flows using orthogonal subscales. *Computer Methods in Applied Mechanics and Engineering*, 191:4295–4321, 2002.

[25] V. M. Calo. *Residual based multiscale turbulence modeling: finite volume simulations of bypass transition.* PhD thesis, Stanford University, 2004.

[26] T. J. R. Hughes, V. M. Calo, and G. Scovazzi. Variational and multiscale methods in turbulence. In W. Gutkowski and T. A. Kowalewski, editors, *Proceedings of the XXI International Congress of Theoretical and Applied Mechanics (IUTAM)*. Kluwer, 2004.

[27] Y. Bazilevs, V. M. Calo, J. A. Cottrell, T. J. R. Hughes, A. Reali, and G. Scovazzi. Variational multiscale residual-based turbulence modeling for large eddy simulation of incompressible flows. *Computer Methods in Applied Mechanics and Engineering*, 197:173–201, 2007.

[28] R. Codina, J. Principe, O. Guasch, and S. Badia. Time dependent subscales in the stabilized finite element approximation of incompressible flow problems. *Computer Methods in Applied Mechanics and Engineering*, 196:2413–2430, 2007.

[29] R. Codina. Stabilization of incompressibility and convection through orthogonal sub-scales in finite element methods. *Computer Methods in Applied Mechanics and Engineering*, 190:1579–1599, 2000.

[30] J. Principe, R. Codina, and F. Henke. The dissipative structure of variational multiscale methods for incompressible flows. *Computer Methods in Applied Mechanics and Engineering*, 199:791–801, 2010.

[31] R. Codina, J. Principe, and S. Badia. Dissipative structure and long term behavior of a finite element approximation of incompressible flows with numerical subgrid scale modeling. In R. Borst and E. Ramm, editors, *Multiscale methods in computational mechanics*, volume 55 of *Lecture notes in applied and computational mechanics*, pages 75–93. Springer, Netherlands, 2011.

[32] O. Guasch and R. Codina. Statistical behavior of the orthogonal subgrid scale stabilization terms in the finite element large eddy simula-

tion of turbulent flows. *Computer Methods in Applied Mechanics and Enginneering*, 261-262:154–166, 2013.

[33] T. J. R. Hughes, G. Scovazzi, and L. P. Franca. Multiscale and stabilized methods. In E. Stein, R. D. Borst, and T. J. R. Hughes, editors, *Encyclopedia of Computational Mechanics*. Wiley, 2004.

[34] R. Codina, S. Badia, J. Baiges, and J. Principe. Variational multiscale methods in computational fluid dynamics. In E. Stein, R. D. Borst, and T. J. R. Hughes, editors, *Encyclopedia of Computational Mechanics*. Wiley, 2017.

[35] U. Rasthofer and V. Gravemeier. Recent developments in variational multiscale methods for large-eddy simulation of turbulent flow. *Archives of Computational Methods in Engineering*, 25(3):647–690, 2018.

[36] A. M. Vázquez, G. Houzeaux, S. Koric, A. Artigues, J. Aguado-Sierra, R. Aris, D. Mira, H. Calmet, F. Cucchietti, H. Owen, E. Casoni, A. Taha, E. D. Burness, J. M. Cela, and M. Valero. Alya: Multiphysics engineering simulation towards exascale. *Journal of Computer Science*, 14:15–27, 2016.

[37] G. Houzeaux, M. Vázquez, R. Aubry, and J. M. Cela. A massively parallel fractional step solver for incompressible flows. *Journal of Computational Physics*, 228(17):6316–6332, 2009.

[38] F. Brezzi and M. Fortin. *Mixed and hybrid finite element methods*. Springer, Berlin, 1991.

[39] P. Gamnitzer, V. Gravemeier, and W. A. Wall. Time-dependent subgrid scales in residual-based large eddy simulation of turbulent channel flow. *Computer Methods in Applied Mechanics and Enginneering*, 199:819–827, 2010.

[40] M. C. Hsu, Y. Bazilevs, V. M. Calo, T. Tezduyar, and T. J. R. Hughes. Improving stability of stabilized and multiscale formulations in flow simulations at small time steps. *Computer Methods in Applied Mechanics and Enginneering*, 199:828–840, 2010.

[41] S. Badia and R. Codina. On a multiscale approach to the transient stokes problem: Dynamic subscales and anisotropic space-time discretization. *Applied Mathematics and Computation*, 207:415–433, 2009.

[42] O. Colomés, S. Badia, R. Codina, and J. Principe. Assessment of variational multiscale models for the large eddy simulation of turbulent

incompressible flows. *Computer Methods in Applied Mechanics and Engineering*, 285:32–63, 2015.

[43] M. Avila. *Nonlinear subgrid finite element models for low Mach number flows coupled with radiative heat transfer*. PhD thesis, Universitat Politècnica de Catalunya, 2012.

[44] M. Avila, R. Codina, and J. Principe. Large eddy simulation of low Mach number flows using dynamic and orthogonal subgrid scales. *Computers and Fluids*, 99:44–66, 2014.

[45] E. Garnier, M. Mossi, P. Sagaut, P. Comte, and M. Deville. On the use of shock-capturing schemes for large-eddy simulations. *Journal of Computational Physics*, 153:273–311, 1999.

[46] J. Domaradzki and S. Radhakrishnan. Effective eddy viscosities in implicit modeling of decaying high Reynolds number turbulence with and without rotation. *Fluid Dynamics Research*, 36:385–406, 2005.

[47] S. Charnyi, T. Heister, M. A. Olshanskii, and L. G. Rebholz. On conservation laws of Navier-Stokes Galerkin discretizations. *Journal of Computational Physics*, 337:289–308, 2017.

[48] F. Capuano, G. Coppola, L. Rández, and L. de Luca. Explicit Runge-Kutta schemes for incompressible flow with improved energy-conservation properties. *Journal of Computational Physics*, 328:86–94, 2017.

[49] F. X. Trias and O. Lehmkuhl. A self-adaptive strategy for the time integration of Navier-Stokes equations. *Numerical Heat Transfer. Part B*, 60(2):116–134, 2011.

[50] B. Sanderse and B. Koren. Accuracy analysis of explicit Runge-Kutta methods applied to the incompressible Navier-Stokes equations. *Journal of Computational Physics*, 231(8):3041–3063, 2012.

[51] B. Sanderse. Energy-conserving Runge-Kutta methods for the incompressible Navier-Stokes equations. *Journal of Computational Physics*, 233:100–131, 2013.

[52] R. Codina. Pressure stability in fractional step finite element methods for incompressible flows. *Journal of Computational Physics*, 170:112–140, 2001.

[53] R. Codina and J. Blasco. A finite element formulation for the Stokes problem allowing equal velocity-pressure interpolation. *Computer Methods in Applied Mechanics and Engineering*, 143:373–391, 1997.

[54] F. Felten and T. Lund. Kinetic energy conservation issues associated with the collocated mesh scheme for incompressible flow. *Journal of Computational Physics*, 215(2):465–484, 2006.

[55] L. Jofre, O. Lehmkuhl, J. Ventosa, F. X. Trias, and A. Oliva. Conservation properties of unstructured finite-volume mesh schemes for the Navier-Stokes equations. *Numerical Heat Transfer. Part B: Fundamentals*, 54(1):53–79, 2014.

[56] G. Comte-Bellot and S. Corrsin. Simple eulerian time correlation of full and narrow-band velocity signals in grid-generated isotropic turbulence. *Journal of Fluid Mechanics*, 48(2):273–337, 1971.

[57] G. I. Taylor and A. E. Green. Mechanism of the production of small eddies from large ones. *Proceedings of the Royal Society A: Mathematical, Physical and Engineering Sciences*, 158(895):499–521, 1937.

[58] W. M. Van Rees, A. Leonard, D. I. Pullin, and P. Koumoutsakos. A comparison of vortex and pseudo-spectral methods for the simulation of periodic vortical flows at high Reynolds numbers. *Journal of Computational Physics*, 230(8):2794–2805, 2011.

[59] J. R. Bull and A. Jameson. Simulation of the Taylor-Green vortex using high-order flux reconstruction schemes. *AIAA Journal*, 53(9):2750–2761, 2015.

[60] C. Moulinec, J. Fang, R. D. Sandberg, W. Wang, and D. R. Emerson. Comparison between several approaches to simulate the Taylor-Green vortex. Presented at the 28th International Conference on Parallel Computational Fluid Dynamics, Kobe, Japan, 2016.

[61] J. Hunt, A. A. Wray, and P. Moin. Eddies, stream and convergence zones in turbulent flows. *Center for Turbulent Research Report CTR-S88*, 1988.

[62] R. D. Moser, J. Kim, and N. N. Mansour. Direct numerical simulation of turbulent channel flow up to $re_\tau = 590$. *Physics of Fluids*, 11(4):943–945, 1999.

[63] A. Rouhi, U. Piomelli, and B. J. Geurts. Dynamic subfilter-scale stress model for large-eddy simulations. *Physical Review Fluids*, 1(4):044401, 2016.

[64] J. C. Del Álamo, J. Jiménez, P. Zandonade, and R. D. Moser. Scaling of the energy spectra of turbulent channels. *Journal of Fluid Mechanics*, 500:135–144, 2004.

[65] O. Colomés. *Large scale finite element solvers for the large eddy simulation of incompressible turbulent flows.* PhD thesis, Universitat Politècnica de Catalunya, 2016.

[66] E. Achenbach. Vortex shedding from spheres. *Journal of Fluid Mechanics*, 62(2):209–221, 1974.

[67] C. Wieselsberger. Further information on the laws of fluid resistance. *Technical note*, 1974.

[68] I. Rodríguez, R. Borrell, O. Lehmkuhl, C. D. Pérez-Segarra, and A. Oliva. Direct numerical simulations of the flow past a sphere at Re = 3700. *Journal of Fluid Mechanics*, 679:263–287, 2011.

[69] I. Rodríguez, O. Lehmkuhl, R. Borrell, and A. Oliva. Flow dynamics in the wake of a sphere at sub-critical Reynolds numbers. *Computers & Fluids*, 80:233–243, 2013.

[70] V. Seidl, S. Muzaferija, and M. Peric. Parallel DNS with local grid refinement. *Applied Scientific Research*, 59:379–394, 1998.

[71] S. R. Ahmed, G. Ramm, and G. Faltin. Some salient features of the time averaged ground vehicle wake. *SAE paper no*, 840300, 1984.

[72] H. Lienhart, C. Stoots, and S. Becker. Flow and turbulence structures in the wake of a simplified car model (Ahmed model). In *DGLR Fach. Symp. der AG STAB*, Stuttgart University, 2000.

[73] C. Hinterberger, M. García-Villalba, and W. Rodi. Large eddy simulation of the flow around the Ahmed body. The aerodynamics of vehicles: trucks, buses, and trains. *Numerical Heat Transfer, Part B*, pages 77–78, 2004.

[74] S. Krajnović and L. Davidson. Flow around a simplified car: Part 1: Large eddy simulation. *ASME: Journal of Fluids Engineering*, 127:907–919, 2005.

[75] S. Krajnović and L. Davidson. Flow around a simplified car: Part 2: Understanding the flow. *ASME: Journal of Fluids Engineering*, 127:919–928, 2005.

[76] M. Minguez, R. Pasquetti, and E. Serre. High-order large-eddy simulation of flow over the Ahmed body car model. *Physics of Fluids*, 20(9):095101, 2008.

[77] E. Serre, M. Minguez, R. Pasquetti, E. Guilmineau, G. Deng, M. Kornhaas, M. Schäfer, J. Frölich, C. Hinterberger, and W. Rodi. On simulating the turbulent flow around the Ahmed body: A French-German

collaborative evaluation of LES and DES. *Computers & Fluids*, 78:10–23, 2013.

[78] D. Aljure, O. Lehmkuhl, I. Rodríguez, and A. Oliva. Flow and turbulent structures around simplified car models. *Computers & Fluids*, 96:122–135, 2014.

[79] P. R. Spalart. Direct numerical simulation of a turbulent boundary layer up to $re_\theta = 1410$. *Journal of Fluid Mechanics*, 187:61–98, 1988.

[80] K. Akselvoll and P. Moin. Application of the dynamic localization model to large eddy simulation of turbulent flow over a backward-facing step. *Engineering Applications of Large Eddy Simulation, ASME*, 1993.

[81] K. Akselvoll and P. Moin. Large-eddy simulation of turbulent confined coannular jets. *Journal of Fluid Mechanics*, 315:387–411, 1996.

[82] R. H. Kraichnan. Diffusion by a random velocity field. *Physics of Fluids*, 13(1):22–31, 1969.

[83] A. Keating, U. Piomelli, E. Balaras, and H. J. Kaltenbach. A priori and a posteriori tests of inflow conditions for large-eddy simulation. *Physics of Fluids*, 16(12):4696–4712, 2004.

[84] P. Sagaut, S. Deck, and M. Terracol. *Multiscale and multiresolution approaches in turbulence*. Imperial College Press, London, 2006.

[85] G. R. Tabor and M. H. Baba-Ahmadi. Inlet conditions for large eddy simulation: A review. *Computers & Fluids*, 39:553–567, 2010.

[86] X. Wu. Inflow turbulence generation methods. *Annual Review of Fluid Mechanics*, 49:23–49, 2017.

[87] N. S. Dhamankar, G. A. Blaisdell, and A. S. Lyrintzis. Overview of turbulent inflow boundary conditions for large-eddy simulations. *AIAA Journal*, 56(4):1317–1334, 2018.

[88] K. Meister, T. Lutz, and E. Krämer. Simulation of a 5MW wind turbine in an atmospheric boundary layer. *Journal of Physics: Conference Series*, 555:012071, 2014.

[89] N. Li, E. Balaras, and U. Piomelli. Inflow conditions for large-eddy simulations of mixing layers. *Physics of Fluids*, 12(4):935–938, 2000.

[90] T. S. Lund, X. Wu, and K. D. Squires. Generation of inflow data for spatially-developing boundary layer simulations. *Journal of Computational Physics*, 140(2):233–258, 1998.

[91] S. Lee, S. K. Lele, and P. Moin. Simulation of spatially evolving turbulence and the application of taylor's hypothesis in compressible flow. *Physics of Fluids*, 4:1521–1530, 1992.

[92] H. Le, P. Moin, and J. Kim. Direct numerical simulation of turbulent flow over backward-facing step. *Journal of Fluid Mechanics*, 330:349–373, 1997.

[93] A. Smirnov, S. Shi, and I. Celik. Random flow generation technique for large eddy simulations and particle-dynamics modeling. *Journal of Fluids Engineering*, 123(2):359–371, 2001.

[94] P. Batten, U. Goldberg, and S. Chakravarthy. Interfacing statistical turbulence closures with large-eddy simulation. *AIAA Journal*, 42(3):485–492, 2004.

[95] M. Klein, A. Sadiki, and J. Janicka. A digital filter based generation of inflow data for spatially developing direct numerical or large eddy simulations. *Journal of Computational Physics*, 186(2):652–665, 2003.

[96] A. Kempf, M. Klein, and J. Janicka. Efficient generation of initial- and inflow-conditions for transient turbulent flows in arbitrary geometries. *Flow Turbulence and Combustion*, 74:67–84, 2005.

[97] L. Davidson. Using isotropic synthetic fluctuations as inlet boundary conditions for unsteady simulations. *Advances and Applications in Fluid Mechanics*, 1(1):1–35, 2007.

[98] N. Jarrin, S. Benhamadouche, D. Laurence, and R. Prosser. A synthetic-eddy method for generating inflow conditions for large-eddy simulations. *International Journal of Heat and Fluid Flow*, 27(4):585–593, 2006.

[99] N. Jarrin, A. Revell, R. Prosser, and D. Laurence. Reconstruction of turbulent fluctuations for hybrid RANS/LES simulations using a synthetic-eddy method. *International Journal of Heat and Fluid Flow*, 30(3):435–442, 2009.

[100] M. Pamiès, P. E. Weiss, E. Garnier, S. Deck, and P. Sagaut. Generation of synthetic turbulent inflow data for large eddy simulation of spatially evolving wall-bounded flows. *Physics of Fluids*, 21:045103, 2009.

[101] R. Poletto, T. Craft, and A. Revell. A new divergence free synthetic eddy method for the reproduction of inlet flow conditions for LES. *Flow, Turbulence and Combustion*, 91(3):519–539, 2013.

[102] T. Ishihara, K. Hibi, and S. Oikawa. A wind tunnel study of turbulent flow over a three-dimensional steep hill. *Journal of Wind Engineering and Industrial Aerodynamics*, 83:95–107, 1999.

[103] J. Fang and F. Porté-Agel. On a multiscale approach to the transient stokes problem: Dynamic subscales and anisotropic space-time discretization. *Journal of Physics: Conference Series*, 753:082008, 2016.

[104] M. Diebold, C. Higgins, J. Fang, A. Bechmann, and M. Parlange. Flow over hills: a large-eddy simulation of the Bolund case. *Boundary-Layer Meteorology*, 148(1):177–194, 2013.

[105] D. R. Chapman. Computational aerodynamics, development and outlook. *AIAA Journal*, 17:1293–1313, 1979.

[106] H. Choi and P. Moin. Grid requirements for large eddy simulation: Chapman's estimates revisited. *Center for Turbulence Research Annual Research Briefs*, 2011.

[107] J. W. Deardorff. A numerical study of three-dimensional turbulent channel flow at large Reynolds numbers. *Journal of Fluid Mechanics*, 41:453–480, 1970.

[108] U. Schumann. Subgrid-scale model for finite difference simulation of turbulent flows in plane channels and annuli. *Journal of Computational Physics*, 18:376–404, 1975.

[109] G. Grötzbach. Direct numerical and large eddy simulation of turbulent channel flows. In *Encyclopaedia of Fluid Mechanics*, volume 6, pages 1337–1391. Gulf Publishing Houston, 1987.

[110] U. Piomelli, J. H. Ferziger, P. Moin, and J. Kim. New approximate boundary conditions for large eddy simulations of wall-bounded flows. *Physics of Fluids*, 1(6):1061–1068, 1989.

[111] P. J. Mason and N. S. Callen. On the magnitude of the subgrid-scale eddy coefficient in largeeddy simulations of turbulent channel flow. *Journal of Fluid Mechanics*, 162:439–462, 1986.

[112] I. Marusic, G. Kunkel, and F. Porté-Agel. Experimental study of wall boundary conditions for large eddy simulation. *Journal of Fluid Mechanics*, 446:309–320, 2001.

[113] H. Werner and H. Wengle. Large-eddy simulation of turbulent flow around a cube in a plane channel. In *8th Symposium on Turbulent Shear Flows*, Munich, Germany, 1991.

[114] Y. Hassan and H. Barsamian. New-wall modelling for complex flows using the large eddy simulation technique in curvilinear technologies. *International Journal of Heat and Mass Transfer*, 44:4009–4026, 2001.

[115] U. Piomelli and E. Balaras. Wall-layer models for large-eddy simulations. *Annual Revision of Fluid Mechanics*, 34:349–374, 2002.

[116] U. Piomelli. Wall-layer models for large-eddy simulations. *Progress in Aerospace Sciences*, 44(6):437–446, 2008.

[117] J. Larsson, S. Kawai, J. Bodart, and I. Bermejo-Moreno. Large eddy simulation with modelled wall stress: recent progress and future directions. *Mechanical Engineering Reviews*, 3(1), 2016.

[118] S. T. Bose and G. I. Park. Wall-modeled large-eddy simulation for complex turbulent flows. *Annual Review of Fluid Mechanics*, 50:535–561, 2018.

[119] D. Lacasse, É. Turgeon, and D. Pelletier. On the judicious use of the k-ε model, wall functions and adaptivity. *International Journal of Thermal Sciences*, 43:925–938, 2004.

[120] T. Chacon Rebollo, M. Gomez Marmol, and S. Rubino. Numerical analysis of a finite element projection-based vms turbulence model with wall laws. *Computer Methods in Applied Mechanics and Engineering*, 285:379–405, 2015.

[121] A.J. Lew, G.C. Buscaglia, and P.M. Carrica. A note on the numerical treatment of the k-epsilon turbulence model. *International Journal of Computational Fluid Dynamics*, 14(3):201–209, 2001.

[122] D. Kuzmin, O. Mierka, and S. Turek. On the implementation of the k-epsilon turbulence model in incompressible flow solvers based on a finite element discretisation. *International Journal of Computing Science and Mathematics*, 1(2-4):193–206, 2007.

[123] Y. Bazilevs and T. J. R. Hughes. Weak imposition of Dirichlet boundary conditions in fluid mechanics. *Computers & Fluids*, 36:12–26, 2007.

[124] J. Nitsche. Über ein variationsprinzip zur lösung von Dirichletproblemen bei verwendung von teilräumen, die keinen randbedingungen unterworfen sind. *Abhandlungen aus dem Mathematischen Seminar der Universität Hamburg*, 199:780–790, 1971.

[125] Y. Bazilevs, C. Michler, V. M. Calo, and T. J. R. Hughes. Weak Dirichlet boundary conditions for wall-bounded turbulent flows. *Computer Methods in Applied Mechanics and Engineering*, 196:4853–4862, 2007.

[126] Y. Bazilevs, C. Michler, V. M. Calo, and T. J. R. Hughes. Isogeometric variational multiscale modeling of wall-bounded turbulent flows with weakly enforced boundary conditions on unstretched meshes. *Computer Methods in Applied Mechanics and Engineering*, 36:9–15, 2010.

[127] D. B. Spalding. A single formula for the "law of the wall". *Journal of Applied Mechanics*, 28:455–458, 1961.

[128] A. Gerstenberger and W. A. Wall. An embedded Dirichlet formulation for 3D continua. *International Journal for Numerical Methods in Engineering*, 82:537–563, 2010.

[129] P. Gamnitzer, V. Gravemeier, and W. A. Wall. A mixed/hybrid Dirichlet formulation for wall-bounded flow problems including turblent flow. *Computer Methods in Applied Mechanics and Enginneering*, 245-246:22–35, 2012.

[130] B. Krank and W. A. Wall. A new approach to wall modeling in LES of incompressible flow via function enrichment. *Journal of Computational Physics*, 316:94–116, 2016.

[131] S. Kawai and J. Larsson. Wall-modeling in large eddy simulation: Length scales, grid resolution, and accuracy. *Physics of Fluids*, 24(015105), 2012.

[132] X. I. A. Yang, G. I. Park, and P. Moin. Log-layer mismatch and modeling of the fluctuating wall stress in wall-modeled large-eddy simulations. *Physical Review Fluids*, 2(104601), 2017.

[133] C. C. de Wiart and S. Murman. Assessment of wall-modeled LES strategies within a Discontinuous-Galerkin spectral-element framework. *AIAA Paper*, 2017-1223.

[134] A. Frère, C. C. de Wiart, K. Hillewaert, P. Chatelain, and G. Winckelmans. Application of wall-models to Discontinuous Galerkin LES. *Physics of Fluids*, 29(085111), 2017.

[135] H. Reichardt. Vollständige darstellung der turbulenten geschwindigkeits- verteilung in glatten leitungen. *ZAMM-Zeitschrift für Angewandte Mathematik und Mechanik*, 31:208–219, 1951.

[136] C. Meneveau, C. Lunds, and W. Cabot. A Lagrangian dynamic subgridscale model of turbulence. *Journal of Fluid Mechanics*, 319:353–385, 1996.

[137] S. Hoyas and J. Jiménez. Scaling of the velocity fluctuations in turbulent channels up to $Re_\tau = 2003$. *Physics of Fluids*, 18, 2006.

[138] T. Arbogast, M. F. Wheeler, and I. Yotov. Mixed finite elements for elliptic problems with tensor coefficients as cell-centered finite differences. *SIAM Journal on Numerical Analysis*, 34:828–852, 1997.

[139] F. Porté-Agel, C. Meneveau, and M. B. Parlange. A scale-dependent dynamic model for large-eddy simulation: application to a neutral atmospheric boundary layer. *Journal of Fluid Mechanics*, 415:261–284, 2000.

[140] A. Andrén, A. R. Brown, J. Graf, P. J. Mason, C.-H. Moeng, F. T. M Nieuwstadt, and U. Schumann. Large-eddy simulation of a neutrally stratified boundary layer: A comparison of four computer codes. *Quarterly Journal of the Royal Meteorological Society*, 120:1457–1484, 1994.

[141] G. I. Park. Wall-modeled large-eddy simulation of a separated flow over the NASA wall-mounted hump. *Center for Turbulence Research Annual Research Briefs*, 2015.

[142] D. Greenblatt, K. B. Paschal, C. S. Yao, J. Harris, N. W. Schaeffler, and A. E. Washburn. Experimental investigation of separation control part 1: Baseline and steady suction. *AIAA Journal*, 44(12):2820–2830, 2006.

[143] A. Avdis, S. Lardeau, and M. Leschziner. Large eddy simulation of separated flow over a two-dimensional hump with and without control by means of a synthetic slot-jet. *Flow Turbulence and Combustion*, 83:343–370, 2009.

[144] E. Balaras and C. Benocci. Subgrid scale models in finite difference simulations of complex wall bounded flows. *AGARD-CP-551*, pages 2.1–2.6, 1994.

[145] E. Balaras, C. Benocci, and U. Piomelli. Two-layer approximate boundary conditions for large-eddy simulations. *AIAA Journal*, 34(6):1111–1119, 1996.

[146] W. Cabot and P. Moin. Approximate wall boundary conditions in the large-eddy simulation of high Reynolds number flow. *Flow, Turbulence and Combustion*, 63:269–291, 1999.

[147] M. Wang and P. Moin. Dynamic wall modeling for large-eddy simulation of complex turbulent flows. *Physics of Fluids*, 14:2043–2051, 2002.

[148] S. Kawai and J. Larsson. Dynamic non-equilibrium wall-modeling for large eddy simulation at high Reynolds numbers. *Physics of Fluids*, 25:015105, 2013.

[149] G. I. Park and P. Moin. An improved dynamic non-equilibrium wall-model for large eddy simulation. *Physics of Fluids*, 26:015108, 2014.

[150] W. Cabot. Large-eddy simulations with wall models. *Center for Turbulence Research Annual Research Briefs*, pages 41–50, 1995.

[151] W. Cabot. Near-wall models in large eddy simulations of flow behind a backward-facing step. *Center for Turbulence Research Annual Research Briefs*, pages 199–210, 1996.

[152] A. I. Heft. *Aerodynamic investigation of the cooling requirements of electric vehicles*. PhD thesis, Technische Universität München, 2014.

[153] A. I. Heft, T. Indiger, and N. A. Adams. Experimental and numerical investigation of the DrivAer model. In *Proceedings of the ASME 2012 Fluids Engineering Summer Meeting*, pages 1–11, Puerto Rico, USA, 2014.

[154] A. I. Heft, T. Indiger, and N. A. Adams. Introduction of a new realistic generic car model for aerodynamic investigations. *SAE Technical Paper*, 2012-01-0168, 2012.

[155] S. Mack, T. Indiger, N. A. Adams, S. Blume, and P. Unterlechner. The interior design of a 40% scaled DrivAer body and first experimental results. In *Proceedings of the ASME 2012 Fluids Engineering Summer Meeting*, volume FEDSM2012-72371, Puerto Rico, USA, 2012.

[156] C. Strangfeld, D. Wieser, H. Schmidt, R. Woszidlo, C. Nayeri, and C. Paschereit. Experimental study of baseline flow characteristics for the realistic car model DrivAer. *SAE Technical Paper*, 2013-01-1251, 2013.

[157] D. Wieser, H. Schmidt, C. Strangfeld, S. Müller, C. Nayeri, and C. Paschereit. Experimental comparison of the aerodynamic behavior of fastback and notchback DrivAer models. *SAE Technical Paper*, 2014-01-0613, 2014.

[158] B. C. Peters, M. Uddin, J. Bain, A. Curley, and M. Henry. Simulating DrivAer with structured finite difference overset grids. *SAE Technical Paper*, 2015-01-1536, 2015.

[159] E. Guilmineau. Numerical simulations of flow around a realistic generic car model. *SAE International Journal of Passenger Cars - Mechanical Systems*, 7(2):646–653, 2014.

[160] E. Guilmineau. Numerical simulations of ground simulation a realistic generic car model. In *Proceedings of the ASME 2014 4th Joint US-European Fluids Engineering Division Summer Meeting*, Chicago, USA, 2014.

[161] N. Ashton, A. West, S. Lardeau, and A. Revell. Assessment of RANS and DES methods for realistic automotive models. *Computers and Fluids*, 128:1–15, 2016.

[162] D. E. Aljure, J. Calafell, A. Baez, and A. Oliva. Flow over a realistic car model: Wall modeled large eddy simulations assessment and unsteady effects. *Journal of Wind Engineering and Industrial Applications*, 174:225–240, 2018.

[163] A. Pasquali, M. Schönherr, M. Geier, and M. Krafczyk. Simulation of external aerodynamics ofthe DrivAer model with the LBM on GPGPUs. In G. R. Joubert, H. Leather, M. Parsons, F. Peters, and M. Sawyer, editors, *Parallel computing: On the road to exascale*, volume 27 of *Advances in parallel computing*, pages 391–400. IOS Press, 2016.

[164] S. Jakirlic, L. Kutej, D. Hanssmann, B. Basara, T. Schütz, and C. Tropea. Rear-end shape influence on the aerodynamic properties of a realistic car model: a RANS and hybrid LES/RANS study. In *New results in numerical and experimental fluid mechanics X: Contributions to the 19th STAB/DGLR Symposium Munich, Germany*, pages 397–407. Springer International Publishing, 2014.

[165] J. Berg, J. Mann, A. Bechmann, M. Courtney, and H. Jørgensen. The Bolund experiment, part I: flow over a steep, three-dimensional hill. *Boundary-Layer Meteorology*, 141(2):219–243, 2011.

[166] A. Bechmann, N. Sørensen, J. Berg, J. Mann, and P. E. Réthoré. The Bolund experiment, part II: blind comparison of microscale flow models. *Boundary-Layer Meteorology*, 141(2):245–271, 2011.

[167] V. Vuorinen, A. Chaudhari, and J. P. Keskinen. Large-eddy simulation in a complex hill terrain enabled by a compact fractional step OpenFOAM solver. *Advances in Engineering Software*, 79:70–80, 2015.

[168] A. Chaudhari, V. Vuorinen, J. Hämäläinen, and A. Hellsten. Large-eddy simulations for hill terrains: validation with wind-tunnel and field measurements. *Computational and Applied Mathematics*, 37:2017–2038, 2018.

[169] J. Prospathopoulos, E. Politis, and P. Chaviaropoulos. Application of a 3D RANS solver on the complex hill of Bolund and assessment of the wind flow predictions. *Journal of Wind Engineering and Industrial Aerodynamics*, 107-108:149–159, 2012.

[170] T. Yeow, A. Cuerva-Tejero, and J. Perez-Alvarez. Reproducing the Bolund experiment in wind tunnel. *Wind Energy*, 18(1):153–169, 2015.

[171] B. Conan, A. Chaudhari, S. Aubrun, J. Beeck, J. Hämäläinen, and A. Hellsten. Experimental and numerical modelling of flow over complex terrain: the Bolund hill. *Boundary-Layer Meteorology*, 158(2):183–208, 2016.

[172] J. Lange, J. Mann, J. Berg, D. Parvu, R. Kilpatrick, A. Costache, J. Chowdhury, K. Siddiqui, and H. Hangan. For wind turbines in complex terrain, the devil is in the detail. *Environmental Research Letters*, 12:094020, 2017.